

ABSTRACT

Title of dissertation: An Experimental Realization
of a Griffiths Phase in ^{87}Rb
in Three Dimensions

Matthew Earl Wallace Reed,
Doctor of Philosophy, 2017

Dissertation directed by: Professor S.L. Rolston
Joint Quantum Institute,
National Institute of Standards and Technology
and
Department of Physics, University of Maryland

We describe a novel High Bandwidth Arbitrary Lattice Generator (HiBAL) we've created to skirt limits imposed on monochromatic standing waves of light. With its current iteration we can phase and amplitude modulate optical lattices over a broad range of wavevectors simultaneously at MHz frequencies. We characterize the HiBAL with a multi-Mach-Zehnder interferometer and a 0.5 NA diffraction limited imaging system, both designed and built in-house. We report lattice phase control to within a few parts in a thousand.

Disorder plays an important role in the phase diagrams of many materials. Crystal defects can cause exotic phases to coexist with the mundane in real world systems, and some phase diagrams are even dominated by the effects of disorder. We report the trapping and characterization of a Bose gas in an optical field isotropic in two dimensions and disordered in a third. We evaluate the phase diagram of our system as a function of temperature and disorder depth, and find favorable comparisons with indications of an intermediate Griffiths phase predicted by previous Monte Carlo and Renormalization

Group studies separating 2D and 3D superfluid regimes.

Finally, I discuss the possibility of realizing the BKT transition in a non-orientable space. The BKT phase transition is an infinite order phase transition in two dimensions from a normal gas to a superfluid mediated by vortices, which are orientable topological phase defects in two dimensions. I discuss the properties of vortices and their interactions on a Mobius strip, and describe how a relay-imaged bichromatic optical potential could be used to form a Mobius strip out of ultracold gases.

An Experimental Realization
of a Griffiths Phase in ^{87}Rb
in Three Dimensions

by

Matthew Earl Wallace Reed

Dissertation submitted to the Faculty of the Graduate School of the
University of Maryland, College Park in partial fulfillment
of the requirements for the degree of
Doctor of Philosophy
2017

Advisory Committee:

Professor Steven L. Rolston, Chair and Advisor

Dr. Gretchen K. Campbell

Professor Mohammed Hafezi, Dean's Representative

Dr. Ian Spielman

Professor Jay Sau

© Copyright by
Matthew Earl Wallace Reed
2017

Foreword

Several of the figures in this thesis will only properly display in, and print from, Adobe Acrobat or Adobe Reader.

Acknowledgments

I dedicate this dissertation to Rufus, who is as old as my graduate work. He's a baaaaad dog.

I'm not a vacuum fluctuation, and neither was the work related in this dissertation. My advisor Steve Rolston has had my back all these years. He made sure the experiment had what it needed, supported my continued education by encouraging me to travel to conferences and relate the work we were doing, put up with me when I panicked, and has been my encyclopedia of atomic physics. None of this would have happened without Zach Smith, the Tweedle Dee to my Tweedle Dum, whose skills, years of work, intellectual rigor, and passion for invention are the life-blood of our experiment. Seriously man, we both know this was at least half you. I'd like to thank in no particular order Gretchen Campbell, Trey Porto, and Ian Spielman for the time I spent bouncing ideas off of them, for the suggestions they made to me in my measurements and analysis, and for finding the time despite my penchant for simply wandering into their offices unscheduled. I'd also like to thank Jay Sau for patiently reintroducing me to the idea that derivations are important when I began to wonder about quanta of angular momentum in nonorientable spaces.

There's been a varying cast of graduate students and undergrads that have had an influence on my work. I thank Matthew Beeler for getting me started as an atomic physicist, and for showing me that when you have no idea what's going on, the only way out is to measure EVERYTHING. Aftaab Dewan showed perseverance when I told him to look into that 'whole quantum monte carlo thing' and pointed him at the internet. I've been told it's damn hard. Paul King, who moved on to grad school at UT Austin, did most of the assembly, testing, and lens tube design work for our prototype high resolution in-situ microscope. Aaron Stahl gave us our levitation coil. I love my 50 ms TOF images; it's probably time for a larger FOV camera. Jonathan Hoffman, Andres Cimmarusti, Varun Vaidya, Kevin Tweidt, David Norris, Jen Johnson, Dan Barker, Dan Campbell,

Andika Putra, Neal Pimenti, Ben Reschovsky, and Creston Herold have all been part of a community here at the JQI that makes it such a cooperative and productive place to work.

Allesandro Restelli has had an enormously positive impact on the JQI as a whole, and in particular I'd like to thank him for teaching me how to modify integrated circuits, on subjects ranging from stabilizing near-DC servos to characterizing and fixing microwave electronics. His advice was instrumental in the construction of our best functioning custom electronics. The sample-and-hold circuit constructed out of a nest of entirely white, unlabelled wires was entirely my fault. Emily Edwards and Steve Rolson have been instrumental in identifying instances of what Jon Hoffman calls "Matt-speak" in my dissertation, and I cannot thank them enough for that.

I am grateful to Sabrina Matthias from Asphericon for working with us, and enabling us to design a fairly high performance microscope without needing to find additional funding.

Most importantly I am grateful to my family, who kept my little diabetic butt alive when I was a toddler, and to my friends, who have made life good.

Table of Contents

Foreword	ii
Acknowledgements	iii
List of Figures	vii
1 Introduction	1
1.1 Phase Transitions [1]	3
1.2 The BKT Transition	5
1.3 The BKT Transition in Finite Systems	6
1.4 Equations of State	9
1.5 The Quasi-2D Approximation, 3D Dynamics and Band Structure	10
1.6 Emerging 3D Superfluidity, Phase Stiffness and the Sliding Phase	13
2 The Chamber	17
2.1 Redesign and Rebuild	18
2.2 Collecting Atoms	21
2.3 RF Evaporation	23
2.4 Transportation	25
3 The Cell	28
3.1 The 1550 nm Cross Dipole Trap	28
3.2 Absorption Imaging	33
3.3 Imaging and Phase Transitions	37
3.4 The High Bandwidth Arbitrary Lattice	42
3.5 Levitation Coil	56
3.6 Microwaves	58
4 The Sliding Phase	60
4.1 Our Sliding Phase	63
4.2 Phase Fluctuations, Induced vs Many-Body	67
4.3 Dispersion in TOF	68
4.4 Phase Fluctuation Power Spectrum	69

4.5	Our Data Set	69
4.6	Momentum-Space Bunching	73
4.7	Our Phase Diagram	81
4.8	Future Directions	82
5	A Mobioid Proposal	83
5.1	An Optical Potential for Mobius Strips of Cold Atoms	84
5.2	Non-Orientable Spaces and a Local \hat{L}	84
5.3	Vorticies in a Non-Orientable Space	86
	Bibliography	94

List of Figures

1.1	Pekker et. al. Pancakes	4
1.2	The Band Gap	11
1.3	Mohan Phase Diagram	13
1.4	Laflorencie Phase Diagram	14
1.5	Pekker et. al.'s Phase Stiffness	15
2.1	Slower Coil Controls	20
2.2	Vacuum Hardware	21
2.3	Chamber Beams	22
2.4	Chamber Controls	23
2.5	RF Coil	24
3.1	Main Platform	30
3.2	Stroboscopic Trap Pair	32
3.3	Cloud Pair Profile	32
3.4	High Resolution Objective Test	39
3.5	BEC In-Situ	41
3.6	In-Situ Imaging System	42
3.7	High Magnification Test, With Filters	43
3.8	One Dimensional Speckle	45
3.9	AOM Diffraction Efficiency	49
3.10	Arbitrary Lattice Generator	52
3.11	Global Phase Shift	54
3.12	Piezo Resonances	55
3.13	Stable Lattice	56
3.14	Unstable Lattice	56
3.15	Phase Lock Suppression	56
3.16	Phase Lock Error	56
3.17	Spin Mixture	58
4.1	The Lattice	60
4.2	Laflorencie Phase Diagram	61
4.3	LaFlorencie's Momentum Distributions	65

4.4	Hot Cloud Profiles	66
4.5	Intermediate Temperature Cloud Profiles	67
4.6	A Cold Cloud	67
4.7	Dispersion in TOF	69
4.8	Fits of $\ln(n(p_{\perp}))$	70
4.9	Coherent Fraction	70
4.10	The Coherence Parameter	71
4.11	Shot Noise in our Quantum Gases	71
4.12	Feng et. al 1D Bose Gas Correlations	74
4.13	2.5V Ensemble Averages	75
4.14	Strange Bose Distributions	75
4.15	Ensemble Average Profiles as a Funcion of Temperature	76
4.16	2.5V Autocorrelation Function	77
4.17	2.5V Autocorrelation Function Cuts	78
4.18	2.5V Convolution Cuts	78
4.19	5V Ensemble Averages	79
4.20	Two Lattices Ensemble Averages at Selected Temperatures	80
4.21	A Sharp Transition in Fluctuation Correlations in a Deep Lattice	80
4.22	Gradual Scaling and an Anomalous Temperature in Fluctuation Convolutions in a Deep Lattice	81
5.1	Mobius Strip Optical Potential	85
5.2	Mobioid Boundary Integrals for Vortices	89
5.3	Mobioid Eigenspace Vortex Green's Function	90
5.4	Method Of Images Solution	91
5.5	The Method of Images Superflow Remainder	92
5.6	A Method of Images	93

Chapter 1: Introduction

Since the first realizations of Bose-Einstein condensation in ^{87}Rb [2] and ^{23}Na [3], the ability of the atomic physics community to precisely engineer Hamiltonians in ultracold systems has enabled an explosion in the experimental study of correlated quantum-degenerate states of matter. Bosons, Fermions [4] [5], and Bose-Fermi mixtures [6] have been cooled to quantum degeneracy. Interatomic scattering has been controlled through Feshbach resonances [7], which have been used to explore a range of phenomena from collapsing BECs [8] to the phase diagrams of strongly interacting states of matter out to the unitary limit. [9] Optical lattices have been used to explore the phase diagrams of toy models of matter such as the Bose-Hubbard [10] [11] and Fermi-Hubbard [12] models. Deep optical lattices allow the exploration of quantum and classical phase transitions in reduced dimension [13] [14]. Spin mixtures have been cooled into spinor condensates [15] and exposed rich phase diagrams [16]. Dynamic, driven, and Raman-coupled atomic clouds have opened up the exploration of quantum states of matter with nontrivial topologies [17], artificial magnetism [18], and dynamic localization [19].

These experiments engineer the systems they study on a microscopic level by controlling the form of the interactions, the geometry and the internal states of their atoms. They reproduce the macroscopic behavior of many novel materials whose microscopic behaviors are not well understood. Particularly interesting are models proposed as the mechanism for measured macroscopic behavior that, in their time, are not computationally tractable. Quantum simulations with engineered systems in cold atomic gases provide a path to computing the macroscopic behavior of those intractable microscopic mod-

els [20] [21]. Most real world materials are not perfectly ordered, and have disordered crystal structures and contaminants, so macroscopic behavior can often include a mixture of several states of matter, or even properties dominated by disorder [22] [23]. The careful engineering and characterizability of Hamiltonians in cold gas quantum simulation experiments allow the measurement of clean systems, and the reintroduction of well characterized controllable disorder has been used to probe its effects . Dimensionality is critical in determining the physics of materials, and cold atom systems have been realized in one, two, and three dimensions [13] [14]. It is also possible to study systems in the crossover between two and three dimensions.

It is in this spirit we have explored the phase diagram of a three dimensional system composed of coupled two dimensional systems in a regime where inter-plane coupling and the bulk properties of the individual planes are subject to disorder. We have realized this system in a time-averaged potential created with a novel multichromatic shallow angle optical lattice, the first realization in cold atoms of a potential isotropic in two directions but disordered in the third. It sits in a regime somewhere between two and three dimensions, where 2D superfluidity develops in individual pancakes, and communication between pancakes allows 3D superfluidity to emerge at lower temperatures. It relates to superconduction in layered type II superconductors, which are planar, and where in-layer disorder may give each layer its own T_c , as well as the emergence of bulk magnetization in stacked planar magnets. We compare our results to theoretical studies that have used Monte Carlo [24], renormalization group [25] and scaling arguments [26] to probe the properties of similar systems. The predicted phase diagrams are not in complete agreement. We observe in-plane condensation and the emergence of order in the third dimension, and discuss the scaling of this behavior in terms of the phases theory predicts should emerge.

1.1 Phase Transitions [1]

By measuring the specific heat of a material and matching the scaling with thermodynamic models the rotational, vibrational, and translation symmetries of materials have been determined. Every degree of freedom gets $\frac{1}{2}k_B T$, where k_B is Boltzmann's constant and T is the temperature of the system. Ehrenfest classified phase transitions according to the first order in which the derivative of the free energy of a system is discontinuous. The free energy of a system can be written in several ways. The Gibbs free energy $G = U + pV - TS$ is the internal energy of a system U , plus the pressure p of the system times the volume V the system occupies, minus the temperature T times the entropy S of the system, where the entropy is the log of the degeneracy of the system. The enthalpy of evaporation is a jump in the first derivative of the energy of a system as a function of temperature, and so Ehrenfest would classify any such transition a first order transition. The technique finds its limits when derivatives of the free energy and the physical quantities they represent diverge, as is the case with Bose-Einstein condensation.

Landau created his own formulation of free energy L . For some ordered phase of matter with order parameter ψ , Landau postulated $L = \sum_{n=0} a_n([K], T)\psi^n$, and that the thermodynamic properties of the transition would be determined by a finite number of derivatives of L in ψ . The order parameter ψ is the average value of a field, and the mean field approximation is the assumption that Landau's postulate applies. The set $[K]$ are coupling constants that parameterize the energy scales in the Hamiltonian, such as the ratio of the kinetic energy to the interaction energy. As a rule, mean field theory breaks down near phase transitions, and is especially poor in describing systems that require the Landau energy to be analytic to all orders, such as the XY phase transition.

Renormalization group theory moved physics to our current understanding of phase transitions. It was inspired by the observation that as a phase transition crosses the critical region, correlations tend to grow on a length scale that is defined by the coupling constants

[K] from Landau theory. The idea follows that an operator will only be definable on that length-scale, and so operators are redefined for each length scale and coupled to each other through a unitary projection operator. The way those operators are defined and connect to each other are referred to as flows, and they reflect the underlying symmetries of the system. A given set of symmetries will thus lead to the construction of a particular renormalization group. The renormalization group that reflects the symmetries of a 2D Bose gas is the XY renormalization group, and it is necessary to describe the transition from a normal gas to a superfluid in 2D, called the Berezinskii-Kosterlitz-Thouless transition, distinct from the 3D BEC transition

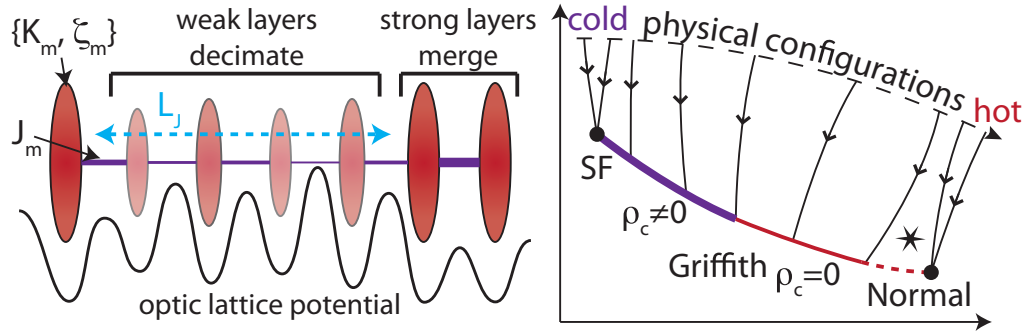


Figure 1.1: Here we see a microscopic model very similar to our system, reprinted with permission from David Pekker [25]. Each pancake has its own superfluid stiffness K_m , coupling J_m , and vortex fugacity ζ_m , a measure of the number of vortices per coherence length. In our system these quantities derive from the temperature, the local effective quasi-2D scattering length \tilde{g} , and the local density.

Our system, a set of 2D systems with randomized interplane hopping rates, is expected to undergo a number of phase transitions as a function of temperature, and the nature of those transitions derive from the 2D symmetry in our system and the broken translation symmetry along the disordered lattice direction. Pekker et al have used the XY renormalization group to describe the transition from a normal gas to sliding phase, where the system has become a bulk 2D superfluid. A sliding phase exhibits superflow in some 2D layers of the bulk 3D system. When initially observed in copper cuprate superconductors this phase was named the sliding phase. At lower temperatures correlations build in the system until 3D superfluidity emerges. It is thus important to understand what the BKT

transition is, what a superfluid is, how it might apply to our system, and its signatures.

1.2 The BKT Transition

In an infinite plane occupied by a Bose gas there exists an infinite order phase transition from a normal gas to a superfluid at finite temperature. Unlike a 3D BEC, a BKT superfluid exhibits no long range order. Bose condensation is impossible in 2D. The superfluid can support persistent frictionless flow and be described by an order parameter ψ . The superfluid is composed of interacting particles of mass m with an interaction energy $n\tilde{g}$, where n is the phase space density, the number of particles per box defined by the deBroglie wavelength $\lambda = \sqrt{2\pi\hbar}/\sqrt{mk_B T}$, and \tilde{g} is the effective in-plane interaction strength. In response to a perturbation, such as a strong delta function potential, a BKT superfluid will smoothly return to the bulk properties of the rest of the gas over a healing length $\chi = \hbar/\sqrt{mgn} = 1/\sqrt{\tilde{g}n}$, where $g = 4\pi\hbar a/m$ is 3D interaction strength of the gas, and a is the atom-atom scattering cross section of the gas. The gas gains a phase stiffness ρ_s , which is defined as the energy cost of applying a phase gradient across the cloud in some given direction $\rho_s^{x_i}(L, T) = \frac{1}{L} \frac{d^2 E(\phi_{x_i})}{d\phi_{x_i}^2}$. In this expression $E(\phi_{x_i})$ is the total energy added to the gas by applying a phase difference ϕ across the gas along the direction x_i . This is true of all quantum-degenerate Bose gases. In a uniform system the gradient will be applied smoothly over the system, and because $E(\phi_{x_i})$ derives from $\frac{d^2}{dx_i^2}$, one can relate phase stiffness to the idea of an effective mass, $E(\vec{k}) = E_0 + \hbar^2 k^2 / 2m_{eff}(\vec{k})$, where $k = \phi_{x_i}/L$. Phase stiffness can also be related to a definition of the superfluid density, $F_{eff} = \rho_{sf}/2 \int dV (\nabla\phi)^2$ [27]. ρ_s varies linearly with ρ_{sf} , but they are not the same number.

The actual particles in the system are the Bosonic atoms, but the transition is best described in terms of quasiparticles called vortices. A vortex is a quantized localization of angular momentum, so that a path integral enclosing its center $\oint_0^{2\pi} \nabla\phi = 2\pi n$. The phase is undefined at its center, making the vortex a phase defect. The order parameter

vanishes at the phase defect, and the depleted region returns to the average n of the gas over the healing length χ . Because of conservation of angular momentum, and because there exist no forces that can exert a torque orthogonal to the vortex's angular momentum, the only way a vortex of charge n may disappear is by annihilating with a vortex of charge $-n$, marking vortices of opposite angular momentum each other's antiparticle. This stands in contrast to 3D BECs and superfluid Helium, where vortices exist as line defects, and can be continuously deformed until the angular momentum is thermalized and expunged into a thermal gas. In this context they are often referred to as vortex anti-vortex pairs. The energy cost of inserting a vortex into the system derives from the kinetic energy of the vortex, both in the extinction at the core and in the angular momentum it spreads throughout the system. In an infinite system the energy of a lone vortex is infinite. A vortex anti-vortex pair, however will have a flow that cancels out at long distance. When the temperature is on the order of the energy required for a vortex anti-vortex pair, unbound pairs will emerge in the fluid. The phase fluctuations due to the density of unbound vortex pairs are so great that, once unbound, the statistics are identical to those of a thermal gas. This is the mechanism by which the BKT transition goes from a BKT superfluid to a thermal gas.

1.3 The BKT Transition in Finite Systems

To create systems with reduced dimensions the atomic physics community relies on deep optical lattices to freeze out transverse motion. An optical lattice is a standing wave of light created by at least two beams with nonzero $\vec{k}_1 - \vec{k}_2$. The intensity of a standing wave induces an AC Stark shift in atoms. This shift in the ground state energy of the atoms acts as a conservative potential. When sufficiently deep the minima of a lattice will confine an atomic wavefunction so tightly the system will act as a set of harmonic traps with excitation energies $E_n = \hbar\omega(n + \frac{1}{2})$. When $\hbar\omega \gg k_B T + \mu$, where the chemical potential μ is the energy cost of introducing an atom into the system, the atoms remain

in the ground state of that potential, confining their motion to two or one dimensions, depending on whether the optical lattice is one dimensional or two. These are called quasi-1D and quasi-2D states because scattering processes are still three-dimensional. Their confinement would need to be significantly smaller than the scattering length of the atoms involved to be truly one or two dimensional.

Some of the first probes of BKT physics in experimental Bose gas systems used scale invariance, a fundamental property of the 2D system. Scale invariant systems can be described by a set of unitless parameters, called scaled parameters, which can be related by simple power-scaling laws across a variety of microscopically distinct systems. Scaled parameters are constructed out of ratios of physical quantities, and so by understanding one such system, one can construct a picture of the behavior of other systems under a wide parameter regime about the BKT phase transition. These composite quantities in aggregate need to hold all the length scale, energy scale, and microstate degeneracy information in the problem in order to be an effective macroscopic map to microscopic behavior.

The phase space density $n(\vec{x}, \vec{p})$ of an ultracold quantum system is the probability density of finding a particle at some particular position and momentum evaluated for all possible positions and momenta. When one attempts to evaluate the various thermodynamic potentials of some arbitrary system, it is necessary to introduce an effective grain size below which distinctions are meaningless. For any generic quantum system this is set by Planck's constant. When the in-situ density of an ultracold cloud is actually measured, the order parameter is projected through a resonant photon scattering process on the position eigenbasis, and the momentum distribution cannot be measured simultaneously. The width in momentum space may be taken as a constant function of temperature, giving the conjugate scale in position space, the de Broglie wavelength $\lambda_{dB} = \sqrt{2\pi\hbar^2/mK_B T}$. Using this one can construct an effective scaled phase space density for a quasi-two dimensional

system,

$$\tilde{n}(x, y) = \iiint n(x, y, z, p_x, p_y, p_z) dz dp_x dp_y dp_z \lambda_{dB}^2 \quad (1.1)$$

This quantity is a measure of the local degeneracy, and so is a good place to start in the construction of our map from one particular BKT superfluid to another. It also makes sense to keep track of the ratio of the thermal energy of the cloud to the chemical potential, μ , two macroscopic energy scales which are in principle measurable and independent. Reformulating this ratio in terms of the de Broglie wavelength reveals the same λ^2 scaling.

$$\tilde{\mu} = \mu / K_B T = \mu m \lambda_{dB}^2 / 2\pi \hbar^2 \quad (1.2)$$

Hidden inside μ is another parameter, the interaction energy. The Gross-Pitaevskii equation for the quasi-two-dimensional regime, eq 1.3, can be derived by integrating the third dimension, assuming that the atoms are all in a single eigenstate in that dimension. Using the harmonic oscillator ground state wavefunction, an interaction term coefficient that scales inversely with the confinement length emerges in the Hamiltonian, where l_z is the HO length, and a_{3D} is the scattering length.

$$\hat{H}\psi = \mu\psi = \left(-\frac{\hbar^2}{2m} \frac{d}{d\vec{x}} + \frac{1}{2} m \omega^2 \vec{x} \cdot \vec{x} + \frac{\hbar^2}{2m} N \tilde{g} \psi^* \psi(\vec{x})\right) \psi \quad (1.3)$$

$$\frac{\hbar^2}{2m} \tilde{g} = g_{2D} = \frac{\hbar^2 \sqrt{8\pi}}{m} \frac{a_{3D}}{l_z} \quad (1.4)$$

The dependence of μ on g_{2D} and thus on l_z provides a way to tune $\tilde{\mu}$ relative to \tilde{n} , which has an explicit mass and density dependence, and realize the same physics across atomic species. Likewise l_z and the atomic density n can be scaled to reproduce the same physics over a large temperature range, limited only by higher order scattering terms like three-body loss. By looking at density fluctuations, and comparing density fluctuations in microscopically distinct systems across the BKT phase transition Zhang et. al. experimentally confirmed this scaling, showing the physics of finite quasi-two-dimensional

disorderless systems to be scale invariant in correspondence with the thermodynamic limit. [28]

1.4 Equations of State

To relate experimental realizations of 2D Bose gas systems to the BKT transition we employ the Local Density Approximation (LDA). To zeroth order the LDA takes the chemical potential of the gas as $\mu = \mu_{hom}(n(r)) + V_{ext}(r)$, where $\mu_{hom}(n(r))$ is the chemical potential of a uniform system with a phase space density $n(r)$. To higher order the LDA is valid when the energy of the system is expressible as an integral of a polynomial function of the local density. This sounds like a restatement of Landau's postulate, but rather than derive the function $\mu = f(n) + V$ from his formalism, we take can $f(n)$ as a map directly to the results of the RNG near the critical region. Far from the critical region one can employ a number of other approximations.

An equation of state is a relationship between several thermodynamic quantities in a generalized system, and is derived from a measurable thermodynamic quantity, such as the Gibbs free energy or the Helmholtz free energy. The Gibbs-Duham equation, $dP = nd\mu + sdT$, is one such equation. With a developed set of meaningful effective local scaled thermodynamic quantities (the local density approximation regime), one can employ the system's equation of state to use a measurable function, such as an atomic cloud's density distribution, to calculate other meaningful quantities. [29] A trapped bose gas is generally in thermal equilibrium with itself, so a measurement of the density distribution of such a gas can be plugged into the Gibbs-Duham equation to construct the pressure of the gas as a function of position. Ho et. al. provide a path through a set of thermodynamic relations for a trapped quasi-2D gas from a set of in situ density measurements to the chemical potential, temperature, pressure, and entropy density of the gas. The high resolution imaging experiment [30] facilitated a study of the behavior of these thermodynamic quantities across the BKT transition and confirmed the mapping.

Yesfah et. al. compared the experimental results to several approximation regimes and determined where, in what direction, and to what degree these schemes break down. On the cold dense end of the phase diagram the Thomas-Fermi approximation is commonly used to find the ground state in smoothly varying systems. In a very cold, smoothly varying system, the kinetic energy term in the Gross-Pitaevskii equation 1.3 can be considered insignificant $\langle p^2 \rangle / 2m \ll \mu$. But it consistently overestimates the phase space density, underestimates the pressure and describes none of the behavior in the transition region. Being a zero temperature approximation the Thomas-Fermi approximation assumes zero entropy. Likewise Hartree-Fock mean field methods, which assume an absence of long range correlations, break down near the transition, and overestimate the entropy per particle by a large factor beyond the transition point.

1.5 The Quasi-2D Approximation, 3D Dynamics and Band Structure

In our derivation of the effective interaction parameter in a quasi-2D system we assumed an isolated system whose out-of-plane wavefunction can be well represented by a harmonic oscillator. In real systems these harmonic traps are generated with optical lattices.

$$\hat{H} = \hat{p}^2 / 2m - V_0 \cos(\vec{k} \cdot \vec{x}) + g \hat{\psi}^\dagger \hat{\psi} \quad (1.5)$$

If we drop the interaction term and evaluate $\langle \psi | \hat{H} | \psi \rangle$ in the position basis we return a differential equation identical to the Mathieu Equation, and so our single particle solutions are Mathieu functions. These constitute the Bloch solutions $\psi_{\vec{k}}(\vec{r})$ to the periodic potential $V(\vec{r}) = V(\vec{r} - \vec{R})$ for the special case of a sinusoidal potential. In contrast to the plane-wave solution there does not exist a solution for every energy E . The solutions with a real-valued eigenenergy are confined to bands, and the regions with imaginary solutions are referred to as band gaps. At low lattice depths $\nu = V_0/E_R$, where E_R is the recoil energy $(\hbar k)^2/2m$, the dispersion relation diverges from a free particle's spectrum, $p^2/2m$.

The solutions are the elliptic sine and cosine functions. They are analytic but have no simple closed form solution, and have to be evaluated numerically. The band width and band gap can be approximated in series expansions about $\nu = 0$ in ν . In the limit where V_0 is less than or on the order of μ , the chemical potential of the cloud, or the temperature, the phase space density is barely modulated by the presence of the lattice, and one cannot relate the system to the quasi-2D regime. At $\nu \gg 1$ the bands flatten out into discrete energy levels. If we compare those gaps to the eigenspectrum we get when we expand the sinusoidal potential about its minima, and solve for one minimum, we get something that looks like a harmonic oscillator with an offset, out to second order.

$$V = -V_0 \cos(x) = m\omega^2 x^2 / 2 - V_0 \quad (1.6)$$

What we find is $\omega = \sqrt{\frac{V_0}{m}} k$, and eventually we will have a gap size that scales with $\sqrt{V_0}$. In the region where $V_0 \gg E_R$, the deviation from the harmonic oscillator can be calculated

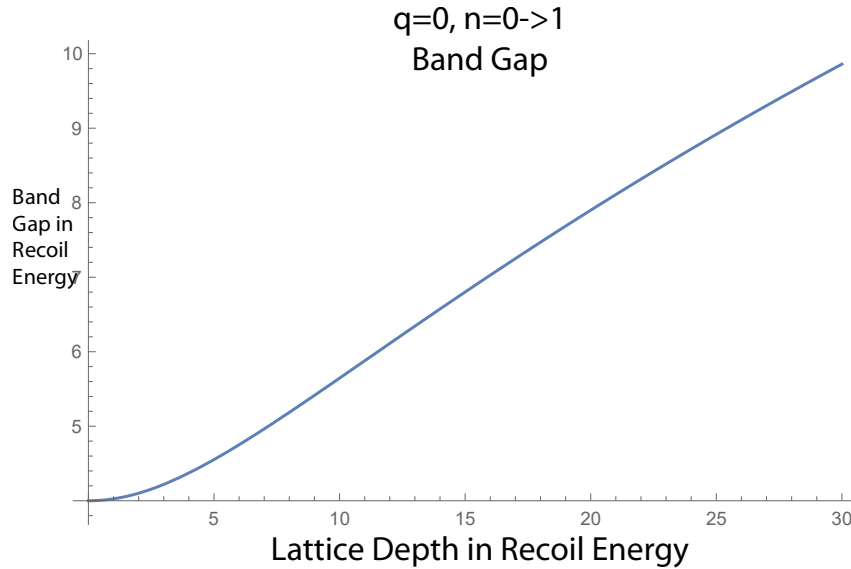


Figure 1.2: Here we consider the energy gap between the ground state and the first excited band at quasimomentum $p = 0$ in the Bloch solution to an atom in a single sinusoidal lattice. The lattice depth and the band gap are both given in terms of recoil energies. This depicts the intermediate region where our data is taken for Rb87 in a $1.3 \mu\text{m}$ lattice. At a vanishing lattice depth, the lowest energy gap is $4E_R$, which in our system corresponds to a temperature of 200 nK. The energy scaling begins to approach $\sqrt{V_0}$ scaling at high V_0 .

in an expansion in $1/\nu$. The energy scale against which we judge if our temperatures and our chemical potentials put us in the quasi-2D regime becomes those discrete gaps.

The crossover region between a 3D and a set of quasi-2D systems is complicated. The first and second excited bands parallel the first and second excited states of the harmonic oscillator. In the lowest band the wavefunction can oscillate at most once per site, much like the ground state of a harmonic oscillator will have one maximum in the center of the potential. The first excited state of a harmonic oscillator has two maxima, just as the first excited Bloch band allows two oscillations per site. But in the regime of strong coupling macroscopic occupations of specific quasimomenta will change the shape and center of mass within a well of the atomic distribution. This stands in contrast to the true quasi-2D regime where the phase relationship between pancakes from one well to the next has no effect on the in-well distribution. It always looks like a harmonic oscillator state. When we consider a quasi-2D system we can make corrections to the two-dimensional LDA by considering localized, fractional occupations of vibrational states perpendicular to our pancakes. In the case of well isolated pancakes those localized vibrations are just from the occupation of harmonic oscillator states above $n=0$. In contrast in the case of strongly coupled pancakes occupation through the entire first band modifies the rescaled interaction parameter \tilde{g} , so out-of-plane physics will strongly couple to in-plane physics. In the strongly coupled regime the only gap available to define how quasi-quasi-2D we are is the band gap.

Because our system is predicted to become a 2D superfluid in an XY renormalization group phase transition, and because we expect many-body dynamics to drive our phase transitions from a localized insulating state to one with a small but finite superfluid fraction in three dimensions, we will want to be able to describe these planes as distinct, local objects. In order to talk about our clouds as distinct local objects in the strong coupling regime we make a unitary transformation from the Bloch solutions to the Wannier solutions $\phi_{\vec{R}}(\vec{r})$, where the sum over quasimomentum \vec{k} is taken over a single Brillouin zone in band

n .

$$\psi_{n,\vec{k}}(\vec{r}) = e^{i\vec{k}\cdot\vec{r}} u_k(\vec{r}) \quad (1.7)$$

$$\phi_{n,\vec{R}}(\vec{r}) = \frac{1}{\sqrt{N}} \sum_k e^{-i\vec{k}\cdot\vec{R}} \psi_{n,\vec{k}}(\vec{r}) \quad (1.8)$$

This is Wannier's original transformation, providing a generalized way to provide localized solutions for any band structure [31]. These provide us with a localized wave function to evaluate \tilde{g} through direct integration, and to calculate hopping rates by evaluating the overlap of the localized atomic density with neighboring wells.

1.6 Emerging 3D Superfluidity, Phase Stiffness and the Sliding Phase

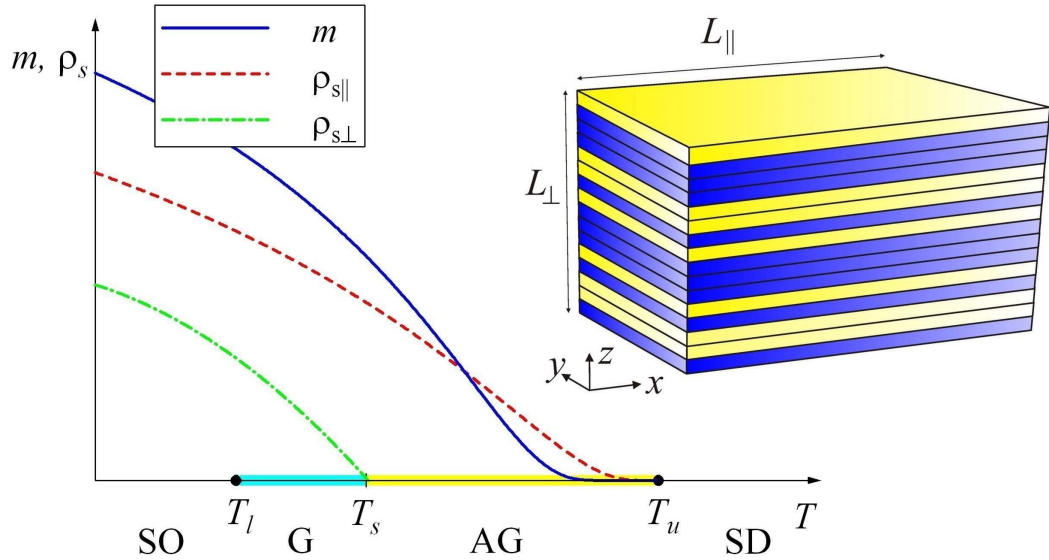


Figure 1.3: Taken from Mohan et al's paper [26], this figure depicts both their model, a random stacking of two different types of planar magnet, and the phase diagram they expect to see as a function of temperature in arbitrary units for their two magnetic stiffnesses and their bulk magnetization m . Using scaling arguments they identify four phases of matter in a disordered stacked system. SO is the strongly ordered phase, G is the non-anomalous Griffiths phase with finite phase stiffness, AG is the anomalous Griffiths phase, so called because it varies with system size, and SD is the strongly disordered phase, a thermal gas.

At sufficiently low temperatures our system is predicted to become a 3D superfluid.

Like a 2D superfluid it supports frictionless flow, and this frictionless flow has a superfluid

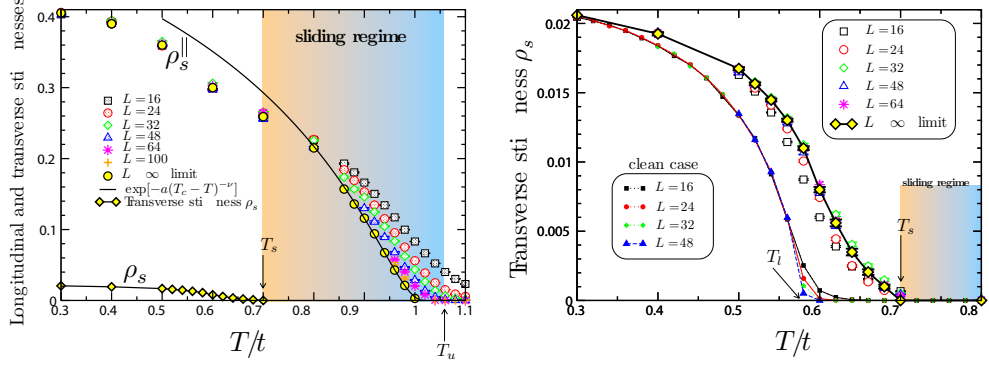


Figure 1.4: Taken from Nicolas Laflorencie’s Monte Carlo paper, this demonstrates the difference between a disordered system and a clean system in a stacked XY two-material system of finite and varying size. Here L corresponds to L_{\perp} . The in plane and perpendicular phase stiffnesses ρ_s scale differently at the transition and have different transition temperatures.

fraction, ρ_{sf} . But in our finite anisotropic system superflow along the length of the lattice is a dubious concept. Instead the phase stiffness ρ_s has been used in [24], [25], and [26] to characterize superfluid transition in disordered stacked superfluids. Mohan et al identify four phases of matter in Figure 1.3. At high and low temperature they identify strongly disordered and strongly ordered phases in their stacked magnets, which through U(1) symmetry map onto our 3D superfluid and thermal gas phases. Between those two extremes are a pair of Griffiths phases, which are phases of matter in disordered systems dominated by the largest deviation from the statistical ensemble in the system. This can be the weakest link in a set of pancakes with disordered hopping potentials, or the longest distance over which each pancake lacks any superfluid fraction. This can be the thickest layer of some particular magnetic material in a disordered stacked planar magnet system. The anomalous Griffiths phase (AG) identified just below T_c for the 2D system is identified as having no phase stiffness, but an anomalous scaling of the free energy F as a function of system length L_{\perp} when a twist is applied across the system, $\Delta F \propto \Phi^2 L_{\perp}^{-z}$, where z is an exponent that varies from ∞ at T_c for 2D order/superfluidity continuously down to 1 at the transition to the non-anomalous Griffiths phase (G), with finite phase stiffness whose properties are dominated once again by rare regions.

In contrast, in a similar system, Nicolas Laflorencie’s Monte Carlo analysis shows

three phases in Figure 4.2: one ordered phase at low temperature, one anomalous Griffiths phase he identifies as the sliding regime, and the thermal phase. This can be explained if his Monte Carlo simulations were unable to identify Griffiths physics in the temperature range where order begins to grow in the disordered direction. The systems he studied were approximately the size of our own system, so the difference could be due to finite size effects.

Pekker et al and Mohan et al agree on the number and variety of phases, but type of disordered system studied by Pekker et al and depicted in Figure 1.1 is closer to our system. It's not a binary system as in the other two works. Each pancake is free to have its own transition temperature, and so every layer is free to be a different material than every other layer. They differ from Nicolas Laflorencie in the size of the phase stiffness seen in the low temperature ordered phase, as can be seen in Figure 1.5. These subtle differences

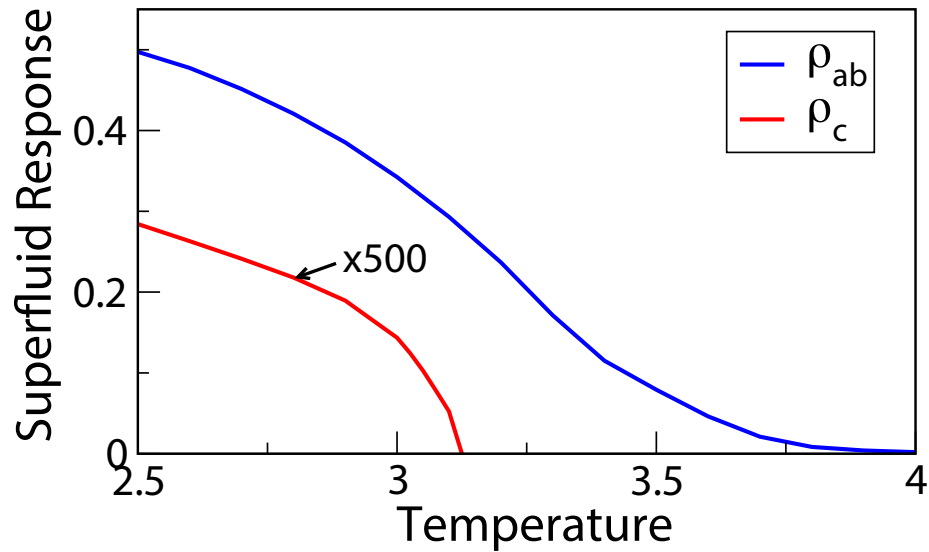


Figure 1.5: The phase stiffness in the ordered phase is predicted to be $\frac{1}{500}$ that of the in-plane phase stiffness, a quantity unlikely to be measurable in our system. Here ρ_{ab} corresponds to ρ_{\parallel} , the in-plane phase stiffness, and ρ_c is the out-of-plane phase stiffness, ρ_{\perp} . The temperature scale is set so that $T = 4$ is the BKT transition temperature.

and the models' relation to a real Bose gas of pancakes with disordered statistics are worth

consideration.

In this thesis, we begin with a description of some of the changes we made in our reconstruction of our BEC production line in chapter 2. In chapter 3 we describe our new optical cross trap, our HiBAL, our new microscope and the microwave and magnetic field control schemes we use to control the atomic state of our ^{87}Rb gas. Chapter 4 compares our experimental realization of disordered stacked quasi-2D Bose gases, from the thermal regime down to the deeply degenerate, to some of the predictions of [24], [25], [26]. Chapter 5 concludes with a description of a novel scheme to realize a BKT superfluid in a Mobius strip, and explores the consequences for vortex physics in a nonorientable space.

Chapter 2: The Chamber

We inherited an apparatus that was designed to conduct a number of different experiments in a number of different physical locations [32] [33] [34]. It was designed to collect ^{87}Rb atoms in a chip trap, and perform some retroreflected lattice experiments in BEC at the trap. It was also designed to move our atoms out to a science cell, where improved optical accessibility enabled both superior microscopy and more flexibility in our optical controls. Finally, it was designed to both perform Rydberg experiments at the chip trap, as well as transport atoms to an arm with a multichannel plate detector for Rydberg physics. Each experiment had their own technological requirements which in turn constrained the performance of the others. The original MOT and magnetic trap were generated on a macroscopic chip trap. It was screwed into a water-cooled block, and a gold mirror was mounted on top of the chip trap. The gold mirror provided for stable retroreflected optical lattices and an effective $\lambda/4$ double pass plus retro for our MOT beams. The chip assembly also had a set of electrodes to provide a DC electric field near the MOT for the use of the Rydberg team.

The optical speckle experiments have all been in our science cell where our optical access gives us opportunities for both quantum control and measurement. Our only purpose for the chip trap was to regularly load sufficient atoms into our 1550 nm tweezer beam for transport to the science cell. The chip trap turned out to have a number of disadvantages. The first was electromechanical. The copper posts which carried current and voltage biases to the chip trap assembly would bend slowly over time, and so much so that they would partially short to the water cooling block. Breaking vacuum in the

main chamber resulted in a significant delay, of at least a month. This also entailed the complete realignment of the optics and recalibration of the electronics. The only dynamic control we had over our magnetic bias fields was a digital switch, and as a rule MOT bias requirements are not the same as molasses bias requirements. Optimization was a mix of timing, bias strength, and MOT beam decollimation to correct for power loss. The chip trap also blocked about half of the field of view of our Zeeman slower, reducing both the load rate and the maximum number in the MOT. Over time there was a degradation of atom number that led to our decision to rebuild the experiment. We replaced the atom chip with a combined magnetic and optical dipole trap that had become more routine in the field since the construction of the chip trap. The final decision to progress to a full rebuild came with the end of the Rydberg experiment and the accidental ablation of Kapton by the 1550 nm dipole beam.

2.1 Redesign and Rebuild

In redesigning the experiment our goal was to develop a more robust experimental apparatus to maximize the time to do physics and minimize the time we spent on daily optimization. Each component had to be robust, stable, and easily servicable. For the most part we followed that philosophy and succeeded in making a much more robust apparatus. On a regular day we now get more than $2 \cdot 10^7$ atoms in our dipole trap before moving out to our science cell, which is over a three-fold increase from the top performance of the old apparatus. We go weeks without needing to touch up the atom collection side of things. With careful optimization the number can be as high as $6 \cdot 10^7$, which is an increase of an order of magnitude over the performance of the old setup when it was working its best.

We reconstructed our MOT and magnetic trap by copying a design used by several BEC experiments at the JQI [35]. We repurposed the vacuum equipment we already had, and bought a pair of custom bucket windows for our 6" Kimball Physics spherical octagon from the Special Techniques division at the Culham Center for Fusion Energy, UKAEA.

These reentrant viewports allow our twenty turn quadrupole coils to sit 0.69" below the 2.75" wide flange, bringing their minimum separation to 1.4", which allows us gradients at the center of our magnetic trap of 230 Gauss/cm. We drive it with an Agilent power supply, and servo it with a NewFocus lock box and a hall sensor.

We kept the same oven and Zeeman slower, a set of 7 coils with independently controllable currents. The cold plate on the oven would cause vacuum problems during power outages, but it is now running on a UPS. The old current controls used darlington pairs, which have to be both heatsunk well and electrically isolated from ground. They had long warm-up times, and so the coil fields would drift over the day. I replaced these with MOSFETS on a watercooled block. The slower coils are attached to the rail of a linear supply, and from there to the individual MOSFET's drains. Each MOSFET's gate is controlled by a current set with its own high impedance trim pot, each of which spans the rail of the same linear supply as the slower coils. The source of each MOSFET is then attached to its own .050 Ω sense resistor, which are attached to the same water cooling block as the MOSFETs. The last sense resistor then attaches to the supply's ground. Varying the current through one MOSFET changes its source voltage, and thus the drain-source voltage that controls it. Significant changes to the coils require a few passes because they are all slightly coupled, through their sense resistors, in series. This is an electronic design flaw we accept to minimize the number of solder joints connecting to the sense resistors. Once set the currents are stable. Each component can be swapped out in minutes; they come to equilibrium within a minute after being turned on.

The chamber used to have a 6" CF cross. One arm went to the chamber, another held the feed-throughs which supplied water to the water cooled block, current to the chip trap, and electric field biases for the Rydberg experiment, the third went to the ion pump+Titanium sublimation pump, and the fourth went to the ion gauge and torque valve. Fig. 2.2 depicts the current vacuum chamber setup. The ion pump, ion gauge, and all-metal valve all connect to the chamber through the same 2.75" flange. The torque valve

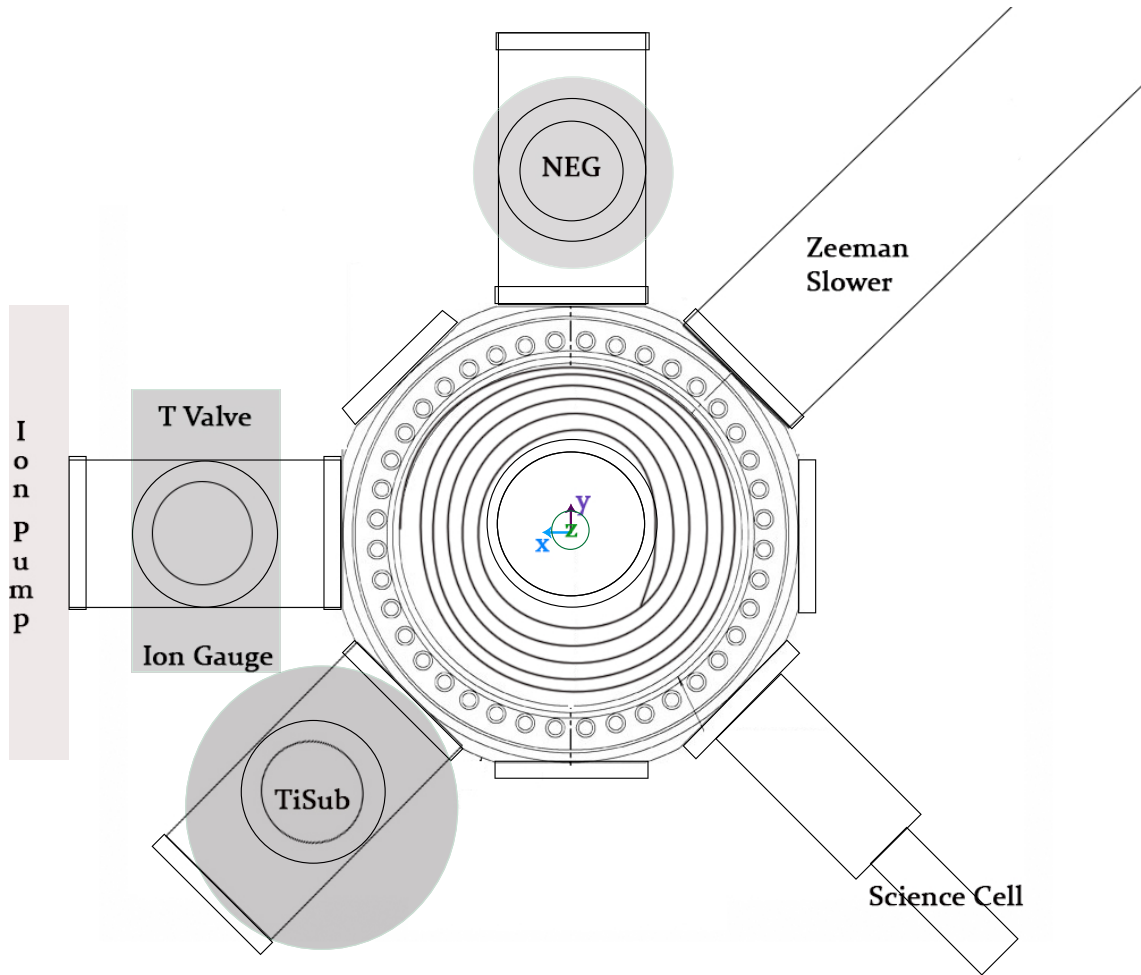


Figure 2.2: The current arrangement of the vacuum hardware, at the elevation of the top quadrupole coil. I've drawn shadows that indicate where the Non-Evaporative Getter, Titanium Sublimation Pump, Ion Gauge and Torque Valve assemblies stand above the rest of the chamber.

2.2 Collecting Atoms

Figure 2.3 depicts the chamber. Our new MOT is a three beam retro-reflected MOT, each beam an inch wide. Each of the MOT beam axes, the \hat{x} , \hat{y} , and \hat{z} axes, has a Hemholtz coil set wrapped around their respective CF flanges to control the bias field in the chamber. These are controlled with bipolar current supplies designed and constructed

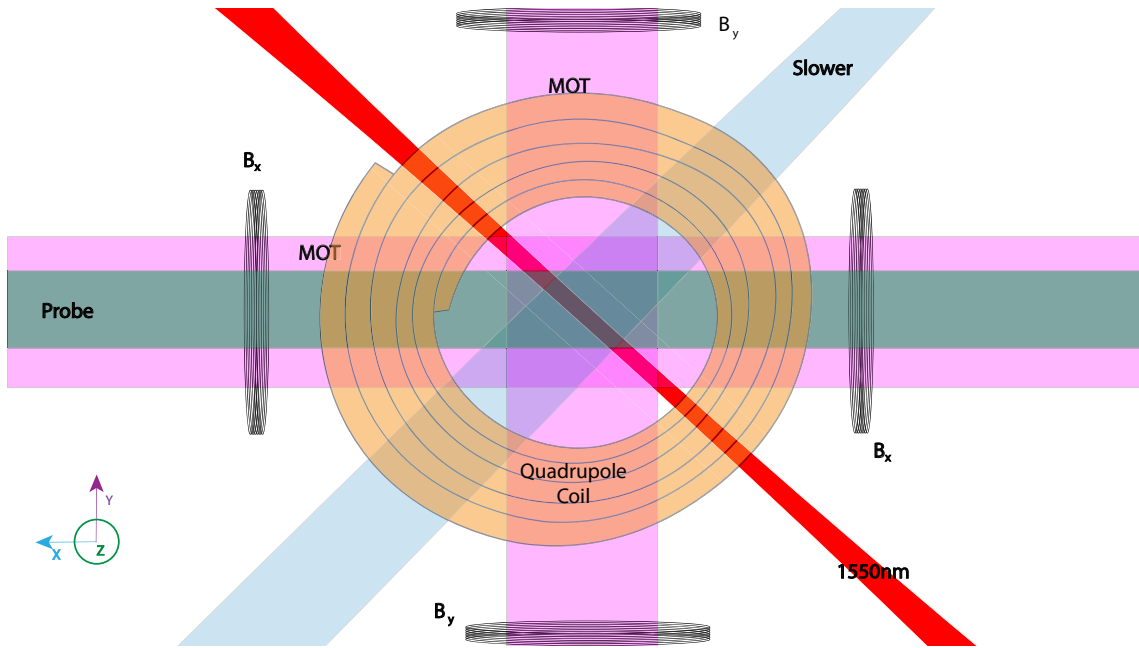


Figure 2.3: Our MOT, imaging, slower and dipole beams in the chamber. Also depicted are our bias coils and our quadrupole coil.

by Zach Smith. Imaging in the chamber is done with a σ^- probe on the x axis, separable from the σ^+ MOT beam. Rotated 45° on the \hat{z} axis are the beam paths for the slower and for the dipole beam.

The cycle starts with all of our laser shutters open and our laser beams on full. The magnetic field biases are set so that the center of the MOT, right before we switch to our optical molasses, sits over the center of the magnetic trap. The biases compensate for both the ambient magnetic field in the chamber and for MOT beam imbalance, which occurs quite naturally in a retroreflected MOT setup. Measured over the first 50 ms, our load rate is 10^9 atoms per second, but saturation effects take over quite quickly, and after an 8 second load we actually have atom clouds $> 10^9$. At this point we use shutters to switch off the slower and slower repumper beams, and allow the MOT two hundred milliseconds to

Object	Shutter/ MOSFET Off	Analog	Control Resolution	Modulation Timescale	Experimental Sensitivity
MOT	✓	✓	μW	μs	$100 \mu W$
MOT Repump	✓	✓	μW	μs	Photons
Slower	✓			100 ms	mW
Slower Repump	✓			100 ms	mW
X&Y Mag Bias	✓	✓	3 mA	ms	100 mA
Mag Quad		✓	60 mA	10 ms	100 mA
Z Bias	✓	✓	3 mA	10 ms	3 mA
Probe	✓	✓	μW	μs	Photons
1550 nm	✓	✓	Contrast, 200:1	100 ns	Watt

Figure 2.4: Our amplitude control capabilities in the chamber. The bipolar bias controls have the capacity to power down the MOSFETS to eliminate any near-field gradients that might affect transport to the cell.

center itself over the magnetic trap. We then drop our repump beam amplitude by a couple orders of magnitude so our atoms spend much more time in $F = 1$ than in $F = 2$. This occurs over 25 ms, and lowers the photon rescattering pressure in the MOT and compresses it. Then we turn off the quadrupole trap entirely, switch our magnetic biases into their molasses configuration, and detune our MOT beams from resonance by 100 MHz to cool the cloud. This molasses step lasts 8 milliseconds. We then use our shutters to turn off the MOT repumper entirely, and allow a millisecond of optical pumping into $F = 1$ from our MOT beams. Then we shutter the MOT beams as well, shift our biases to zero out the magnetic field in the chamber, and snap on our quadrupole field to compression of about twice gravity for atoms in the $F = 1, m_f = -1$ state. This leaves us with about a third of the atoms we had in the MOT. After a 90 ms hold, we ramp the field up to about 12g over 200 ms, and commence RF evaporation.

2.3 RF Evaporation

After the rebuild we had to rework our RF evaporation. The old setup had a two Watt amplifier and a crude antenna. There was a 6" window to project the RF through, so there was little metal to impede the RF. In contrast our bucket window design has no location without a lot of nearby metal. This was initially quite confusing, and before we

installed our fast bipolar bias field controllers our RF evaporation had to be both slow and unreasonably efficient. This slow evaporation meant sources of heating were very important, and one of the larger sources of heating was the RF source itself. The analog RF amplitude control was picking up high frequency signals floating around the room and acting as a mixer, making our tone impure and producing enough signal in the 100s of kHz region to provide a source of loss at the bottom of the trap. One can see how this works when the amplitude A of a frequency sweep $f(t)$ has its own oscillation spectrum, $E = \sum_{\nu} A(\nu, t) d^{-i2\pi\nu t} \cdot e^{-i2\pi f(t)} = \sum_{\nu} A(\nu, t) e^{-i2\pi(\nu+f(t))}$

We attacked the problem from three angles. We added a mF capacitor at the amplitude control for our RF generator as a blocker. I reshaped the antenna to create an RF field orthogonal to the magnetic field at the bottom of the trap. We also bought a 10 Watt amplifier. With these three things we run an RF knife from 17 MHz to 2 MHz over three seconds. To see why an orthogonal RF field maximizes the RF coupling

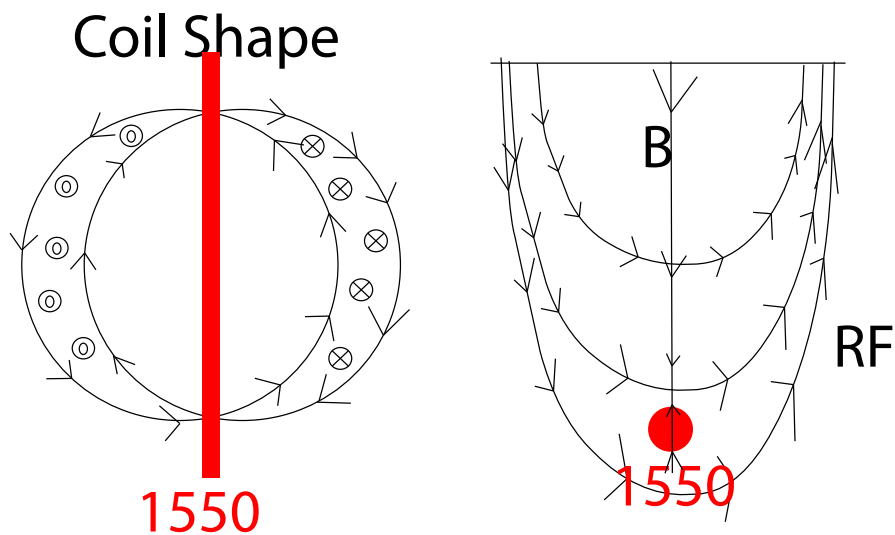


Figure 2.5: We shaped our RF coil so that the magnetic field of the quadrupole coil would be orthogonal to the RF drive field both at the bottom of the trap and all along the 1550, maximizing the efficiency and uniformity of evaporation.

between magnetic sublevels we will take a look at the physics. A stationary neutral

particle in a magnetic field can be described by the Hamiltonian $\hat{H} = -\vec{\mu} \cdot \vec{B}$, where $\vec{\mu}$ is the magnetic moment of our particle and \vec{B} is our magnetic field. If we choose to make our quantization axes local, we can call the direction of the quadrupole field we use to trap our atoms \hat{z} . Decomposing this into the static field B_s and the drive field \vec{B}_d , we can rewrite $\vec{B} = B_s \hat{z} + \vec{B}_d \sin(\omega t)$. Projecting the magnetic moment of the particle onto the x, y, and z axes is then a matter of applying the appropriate Pauli operators to the particle's wavefunction. We can see immediately that $\hat{\sigma}_z$ is diagonal in the quantization axis, so while a small oscillating field $B_{d,z}$ may dress the energies of the individual sublevels, it does not couple them to one another. By minimizing this component along the bottom of the trap in a line that follows the dipole trap we thus maximize our evaporation efficiency and uniformity where the atoms coalesce during evaporation.

2.4 Transportation

Towards the end of our RF evaporation we decompress the trap, and we give it a full second to transition from gravity cancellation to off. When the trap becomes too loose to cancel gravity about half the atoms fall out. The other half are trapped by our 1550 nm dipole beam. The atoms are sufficiently hot and the trap sufficiently loose that the trap cannot be properly written as a harmonic oscillator. If one were to attempt to assign an oscillation frequency along the beam one would say, perhaps, 5 Hz. The time-scale over which the atoms return back to the center of the trap after a sudden movement of the dipole beam is 100 ms, and they do not complete an oscillation in a meaningful way. The optical aperture available to our dipole beam is 12.5 mm wide, and it is 300 mm away from the center of our magnetic trap. To avoid diffraction off the edge of the aperture we have to keep our beam small, and so the smallest waist we can achieve at the focus of the beam is 60 μm . The resulting Rayleigh range for a 1550 nm beam is 8 mm. So to adiabatically decompress along that direction we must move slowly with the magnetic trap decompression at the end of the sequence.

As described in Matthew Beeler's thesis we use an air-bearing Aerotech ABL20040-10 to smoothly and reliably move the single 2" lens which focuses our 1550 nm beam. As before we relay-image that beam with a set of achromats. But we now pass that beam through a 1" polarizing beam-splitter cube. We use the cube to inject our optical cross trap on an orthogonal polarization. The reject port is used for alignment, and this tool has sped up our cross alignment to hours instead of days. Care must be taken that scattered light does not impede transport by putting fringes in the dipole beam.

We also now have the capacity to distinguish between different magnetic states in the cell, to be described in detail in the Science Cell chapter. That measurement has changed the way we transport atoms. Atoms trapped in the $F = 1, m_f = -1$ state are the only magnetically trappable state in the F=1 manifold. There are also two trappable states in the F=2 manifold, but we work hard to ensure we optically pump into the F=1 manifold before we turn on the magnetic trap. We assumed in our slow, seconds long transportation that our atoms adiabatically followed the magnetic field, typical earth fields, putting that splitting at around 100 kHz. What we found was atoms unevenly but consistently distributed throughout the F=1 manifold. This can happen in the presence of light, but atoms scattered into the first excited F=2 manifold will populate into the F=2 ground state manifold as well as F=1. We discovered this problem after we had built up all of our optics and platforms around our science cell, and did not want to disassemble and redesign the closely packed optomechanics to accommodate bias controls running the length of our optical cell and its glass mount. As a partial solution I used a set of fairly large $Ne_2Fe_{14}B$ magnets to lay a track from the center of the chamber out to the cell to increase the magnetic sublevel splitting and to give the area the atoms pass through a large, consistent magnetic field. We find it likely the atoms were passing through a set of weakly coupled avoided crossings as they moved out to the cell. The static field where the atoms sit is now 3.54 Gauss, and we weakly populate the F=0 state when the atoms have arrived in the cell. We clear out the F=0 atoms with a microwave process described at the

end of chapter 3.

Chapter 3: The Cell

Our control and measurement systems in the science cell are the result of three years of work. We have added a new dipole cross trap, a new high resolution microscope, a magnetic dipole for levitation and spin discrimination, a microwave system, and our high bandwidth arbitrary lattice (HiBAL). I will discuss each in order of its development.

3.1 The 1550 nm Cross Dipole Trap

The arrangement we inherited used our 1550 nm transport beam and a second beam which traversed meters of free-space as a cross trap in the cell. The free-space beam was split off from the transport beam with an AOM. Our optics were designed to relay-image the body of that AOM along both the zeroth and first order beams through two different optical paths to the location of the cross trap. There are limits as to what one can do in a real lab environment over several meters of free-space. Over the course of the day the cross would move by about $100\ \mu\text{m}$ down the length of the stage beam. It is almost miraculous that they stayed crossed during this period, but our optical speckle potential and our optical lattice were about 100 μm wide.

I redesigned the cross for stability, and one can view a diagram in Fig. 3.1 The cross trap now launches from a fused silica band gap fiber less than a meter from the location of the final trap. Every optic the cross trap travels through is attached to the same one inch aluminium breadboard by one inch stainless steel posts. Where I could, those posts were also attached to each others through Thorlabs cage cube optic mounts for greater stability. Where this wasn't possible we used Thorlabs Polaris mounts. We purchased the PM fiber

from NKT Photonics. 90% of the mode area is trapped in air, and the comparatively low coefficient of thermal expansion of fused silica minimizes any thermal lensing that occurs on the surface of the fiber. We split off the light for this trap from the stage beam using an AOM (IntraAction) that has a maximum diffraction efficiency of about 80%. It's driven by a very stable IntraAction driver for a -80 MHz shift, and we do not observe deflection due to RF drift reducing the coupling efficiency into the fiber. This AOM is particularly destructive to the mode of the zeroth order beam that passes through when it's driven at high power, but we have not noticed any negative effects on the transfer of our atoms from the stage beam to the cross due to this effect. To ensure a pure polarization the beam passes through a very carefully aligned calcite Glan-Thompson (Glan) polarizer after it exits the fiber, which has an extinction ratio of 100,000:1. It then passes through a fused silica $\lambda/2$ which rotates the polarization to align with the TeO_2 AOM. The zeroth order mode is not observably disturbed when the AOM is driven at spec. At this moment we split the beams using a positive 81.6 MHz shift, but the experimental requirement is only that the frequency must be at least 500 kHz away from 80 MHz, at which point we observe catastrophic heating due to beating between the stage beam and the near-detuned beam.

Both the first and second order beams then pass through a telescope. One lens is a -35mm achromat, and it is the only optic that is not fused silica that the cross trap traverses. Fused silica has a much lower coefficient of expansion with respect to temperature than regular glass, so this optic can produce laser-power dependent lensing and deflection. It's challenging to find appropriate fused silica optics at 1550 nm. We did play with some 1550 coated singlets that were available at the time, but could not produce circularly symmetric beams. The second is a 75 mm lens. This both appropriately sizes the beam waists and separates them physically. They then reflect off a backside polished mirror. At this point the light is carefully set as p-polarized, and is thus maximally transmissive through the dielectric coating of the reflecting mirror. This pass-through signal is used to intensity lock the trap. The transmission of the light as a function of angle, regarding p-polarized

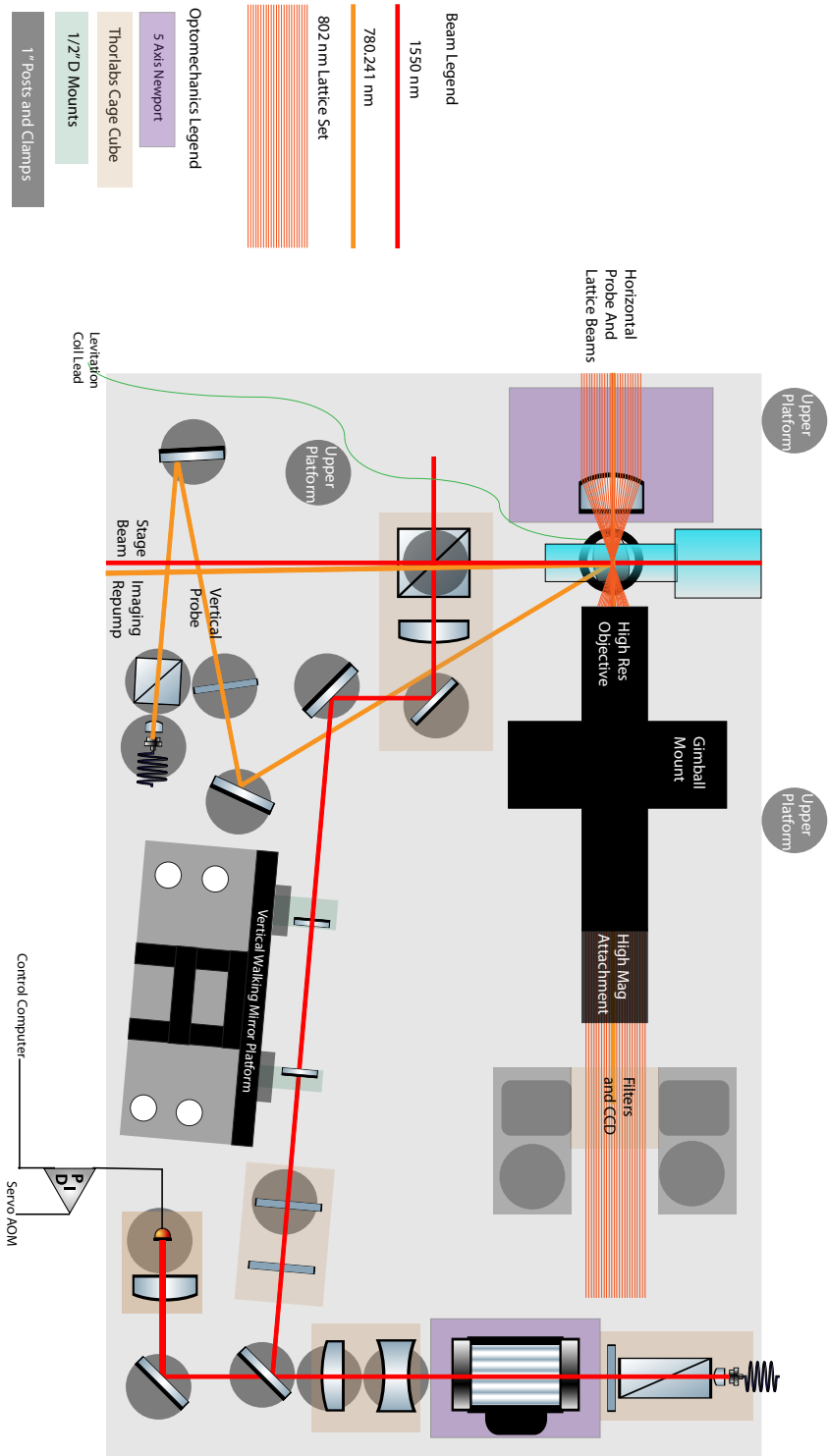


Figure 3.1: This is the main optical breadboard used to mount our high resolution imaging and dipole trap optomechanics. Gravity points into the page. The science cell is shaded a light blue. When viewed in a landscape the optical cross trap starts in the upper right. The translation beam is labelled the stage beam, and comes from off-screen. The HiBAL comes from the upper left and the high res imaging system is to the right of the cell.

light as $\theta = 0$, is $t_p * \cos(\theta) + t_s * \sin(\theta)$. The orthogonal polarization is suppressed to a part in 100,000 by the Glan polarizer, setting a maximum deviation angle as $\arcsin(10^{-5})$, producing deviations in power transmitted from polarization problems of around five parts in 10^{11} . We are thus limited by dust, surface imperfections in our optics, and the amplified photodiode's electronic properties. We find no reason to stabilize high power beams with pick-offs.

The largest source of vibrational instability, which can lead to both heating and the coherent excitation of vibrational and translational modes in a BEC, comes from the next set of optics in the beam path. They are the only optics that act on only one of the two beams. The first-order beam reflects off of a vertical periscope, which is used to set the separation and co-propagation of the two orders. The 1/2" mirrors are set on quarter inch tall, inch wide steel posts, which are in turn attached to a breadboard bolted at a 90° angle to the breadboard that holds all the cross optics. They both then pass through a $\lambda/4$ and a $\lambda/2$ to control the splitting between the reject port and the trap port of the PBS used to combine the cross and stage traps. They then bounce off of their last two walking mirrors, and then a 79 mm focal length fused silica asphere that overlaps the two beams at their foci. Finally they pass through the fused silica PBS and the quartz face of the cell. The science cell separating our vacuum from the rest of our lab is cantilevered off of our atom-collection chamber, and so unlike the rest of our optics it doesn't have micron-level stability, but the angle of the beams mean etaloning is not an issue, and the high quality glass surface doesn't introduce travelling scatterers to our optical trap beams.

This trap is relatively easy to align from scratch. The reject port of the polarizing beam cube can be used for rough alignment. By allowing a small amount of light from both the stage and cross beam to leave through the reject port one can use a florescent card to both confirm the focal points of all three beams and to overlap them. This tool is important in dipole traps whose detuning cannot be brought close to resonance, where the signature in the atom cloud is only present with relatively good overlap and confined to

overlap of all three beams within sixty micrometers of each other in the horizontal.

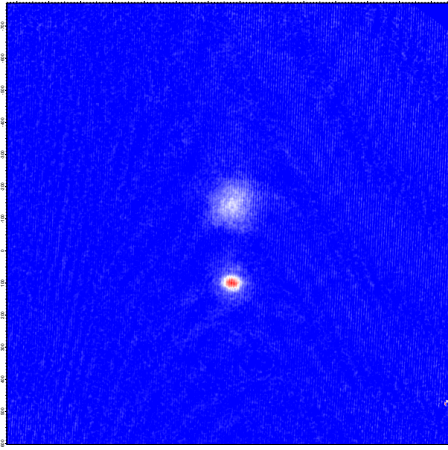


Figure 3.2: Two clouds are captured and cooled using two RF sources and a high speed switch.

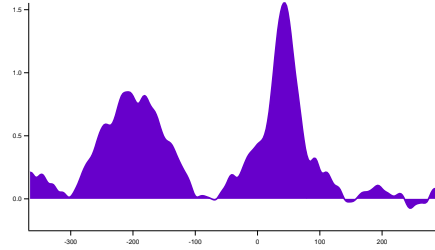


Figure 3.3: The two clouds in profile. In this TOF image one can see that one cloud has condensed while the other has not.

To measure the stability of our trap we applied gaussian fits to images taken with our $1 \mu\text{m}$ diffraction limited imaging system, and we measured sub- μm standard deviations for the position of the cloud. When we measured the velocity distribution of a set of BECs in free-fall TOF we measured net energy contributions to the velocity of the cloud from both in-situ motion and imperfection in our trap turn-off to be sub-Hz. This type of stability is overkill in many experiments, but the study of disorder in particular demands stability. Diverging timescales and vanishing gaps are characteristic of disordered systems, and so extra care must be taken to minimize heating and coherent excitation of low lying states.

Transport does not define, but is a signature of many phases of matter. Our cross was designed with that in mind. Though there have been ballistic measurements of many body localization [36], to my knowledge no one has ever measured atoms in a disordered potential as a circuit element between two imbalanced reservoirs of atoms which can simulate a voltage difference. By varying the RF frequency fed into the AOM that splits the trap we can vary the position of the cross. Fig. 3.2 features a demonstration of two different clouds evaporated in two different traps generated with stroboscopic switching of the cross RF drive frequency. With an AWG or DDS our quasi-imaged AOM cross trap enables dynamic arbitrary tailoring of the longitudinal shape of our trap, and is thus

circuit-element measurement capable.

3.2 Absorption Imaging

In order to understand our images we will have to talk about photon scattering, heating in the imaging process and how that limits our ability to measure our clouds in a fundamental way. If we want to claim we are imaging our clouds at a resolution of a micrometer, we must claim that the atoms in the cloud move less than a micrometer over the whole period of our exposure, which makes high resolution in-situ imaging much different from time of flight imaging.

In a typical time of flight image we are resolving momentum distributions of clouds distributed over millimeters of space. The actual information available about our quantum gases before their release does not exist on diffraction limited lengthscales. Rather it exists on length scales that derive from the time of flight and the equivalent de-Broglie wavelength of the smallest possible momentum in our confined systems. So, for a $50\mu m$ wide cloud of ^{87}Rb , the lowest definable momentum will exist on a lengthscale of $50\mu m$. The velocity of a ^{87}Rb atom with a deBroglie wavelength of $50\mu m$ is $2\pi\hbar/(87\text{amu}\cdot 50\mu m) = .09\mu m/ms$. To separate out this momentum from the zero momentum term we would want 25 microns of separation to resolve the two $50\text{-}\mu m$ -wide clouds. The granularized information available, the information that's meaningful from a quantum information perspective, will thus be either TOF limited or cloud size limited. So during a TOF imaging sequence our only concern is that atoms not, on average, move out of the $50\mu m$ wide spot that is the convolution of our original cloud size with the momentum distribution to produce our actual TOF image. So from a photon absorption and cloud heating perspective, even though our optical resolution is $2\mu m$, the actual information resolution for a 50ms TOF is about $5\mu m$ but our resolvable spot size is $50\mu m$. In such a case we are cloud size limited, and we do not want our atoms to move further than that in the imaging time.

In a misguided effort to get the best SNR possible we shaped our probe pulse to,

on average, be just below total filling for our CCD wells. Our camera is a Point Grey Flea2g running a Sony ICX445. For its price point it sits at a sweet spot in its noise and high quantum efficiency at 780 nm. It has a well depth of 5200 electrons, and a quantum efficiency of about .36, according to the FLIR FL3-GE-03S1M tech specs. So to fill up a ccd pixel, we need about 17300 photons per pixel, each of which, at a magnification of 2, counts for $(3.75/2)^2 = 3.515\mu m^2$. Our TOF images are taken over $150\mu s$, which results in a probe power just over $800\mu W/cm^2$, which is about $.5I_{sat}$ on the cycling transition. Using 3.1 and the D_2 line's linewidth of $2\pi \cdot 6.065$ MHz, we expect to scatter a photon every 150 nanoseconds for a total of 1000 photons per atom per probe exposure.

$$R_{sc} = \frac{\Gamma}{2} \frac{I/I_{sat}}{1 + 4(\Delta/\Gamma)^2 + I/I_{sat}} \quad (3.1)$$

Photons in probe beams have a fairly well defined momentum $\hbar\vec{k}$, and each absorbed photon has two effects. The absorption changes the average velocity of the cloud, and the spontaneous emission takes each atom on a random walk through momentum space that causes heating. When one is anywhere near I_{sat} the doppler effect dominates distortions in imaging, and anyone using absorption imaging should read a paper of which I was only recently made aware. [37] The latter effect occurs in three dimensions and in integer units of the photon's momentum. We can approximate this as a Wiener process in the limit of many scattering events and use the diffusion equation and the resulting variance of its distribution, Eq. 3.2, to calculate heating as a function of time and thus the degradation of our measurement as a function of scattering rate and interrogation time. We can see that the average momentum thus grows as \sqrt{t} and displacement grows as $t^{3/2}$ in eq. 3.3. That comes out to only 3.58 microns of resolution degradation due to heating during a 150-microsecond TOF imaging sequence. This compares well with our $2\mu m$ optical resolution, our approximately $5\mu m$ momentum grain size, and our $50\mu m$ coherent fraction in-situ spot size.

$$\frac{3}{2}KT = \sigma_p^2/2m = dp^2R_{sc}t/4\pi m \quad (3.2)$$

$$\sigma_x = \int \sqrt{dp^2R_{sc}t/2\pi m^2} dt = \frac{2\sqrt{R_{sc}}dp \cdot t^{3/2}}{6\sqrt{\pi}m} \quad (3.3)$$

In-situ pictures place more stringent limits on scattering. If we were to use the same imaging sequence to try to capture our in-situ density distribution in the absence of a lattice we would have convolved the actual distribution with a $3.58 \mu\text{m}$ wide gaussian. In the presence of a lattice perpendicular to the probe, spontaneous emission is reduced in dimensionality by the restricted momentum eigenspace the lattice imposes at low momenta, which enhances the coefficient in the diffusion equation by a factor of $3/2$, bringing our two-dimensional thermal kernel to $5.37 \mu\text{m}$. In addition we have to worry about depth of field effects on our imaging at our high numerical aperture. The momentum added along the imaging axis due to the absorption of photons grows linearly in time as $dpR_{sc}t/m$, and the displacement quadratically. This along-the-beam displacement for our TOF imaging pulse is 415 micrometers. This means our in-situ imaging pulses have to occur quickly. The maximum scattering rate per atoms in a laser beam is given by $\Gamma/2$. At this rate a $4 \mu\text{s}$ imaging sequence will cause π nanometers of displacement, which is already several times our depth of field. A $1 \mu\text{s}$ imaging pulse results in acceptable displacement. Many modern quantum gas microscope experiments get around this by implementing active sideband cooling in deep three dimensional lattice during the imaging process, but photon assisted collisions reduce this to a local number parity measurement.

In order to maximize our SNR we want to scatter as many photons as possible in our in-situ images, and our TOF images are taken at intensities very near to saturation. We must therefore consider how the scattering cross section in an image varies with the probe's field. Direct integration of Eq. 3.4, a differential equation of the intensity using the scattering rate as an absorption coefficient along probe beam direction \hat{z} , gives us Eq.

3.5.

$$\frac{dI(x, y, z)}{dz} = -n(x, y, z)\sigma \frac{1}{1 + I(x, y, z)/I_{sat}} \quad (3.4)$$

$$n_{column}(x, y) = \frac{1}{\sigma} \left(\ln(I_{probe}(x, y)/I_{shadow}(x, y)) + \frac{I_{probe}(x, y) - I_{shadow}(x, y)}{I_{sat}} \right) \quad (3.5)$$

The column density we get from eq. 3.5 is noisier at high I/I_{sat} than at low intensity, when we can use the standard form of Beer's Law. It becomes mostly linear in intensity, which means we must more closely consider our CCDs' response. In the absence of light the CCD has thermal noise which causes a distribution of dark counts with a total span of 40 counts and an average contribution of 20. The edges of the distribution of dark counts are down by 10^{-5} , which sets the gaussian width at 5.89 and a variance of 17.34 counts. In addition we have to deal with the Poissonian statistics of light. For our coherent probe beams the variance is identical to the average number of counts. At first glance this is disastrous. In a very high saturation regime we will have a variance in our atom number identical to the average photon count over the saturation intensity and the scattering cross section, which is identical to our maximum possible signal. The effect is easy to see in Figure 3.5, which has not been subject to any filters. The granularity is not because we are imaging individual atoms. There are eighty thousand atoms in that picture, most of them slightly out of the depth of field. The apparent clumpiness is the result of Poissonian statistics in a short exposure. The solution is straightforward. To accurately gauge what the average of a distribution is we must simply sample it several times. In a practical sense this requires a high enough magnification of the imaging system that each diffraction limited spot size occupies many pixels.

3.3 Imaging and Phase Transitions

In recent years enormous leaps in both thermometry and quantum measurement have been made in the neutral gas community through the use of high resolution in-situ imaging. Citing all the work done along this direction would be redundant, as there are review articles in the literature, so I will briefly discuss the work that was most influential on me personally and some I consider to be the most remarkable.

Cheng Chin's group in Chicago used the fluctuation dissipation theorem to perform in-situ thermometry on in-situ images. [38] The fluctuation dissipation theorem connects the bulk properties of PT reversible materials, which are materials whose Hamiltonians are identical when one mirrors all three spatial dimensions and reverses the flow of time, to microscopic fluctuations that occur in those materials. My favorite mundane example led directly to the theorem's discovery: Johnson-Nyquist noise. Resistors, when unperturbed, will have a time-averaged voltage $\langle V \rangle = 0$ across the resistor, but will have a non-zero time averaged magnitude $\langle V^2 \rangle = 4Rk_B T \Delta\nu$, where $\Delta\nu$ is some bandwidth over which the square of the voltage is measured. This is generally referred to as thermal noise, and different relations for thermal noise exist for different electrical elements. In the case of a resistor with resistivity r and resistance $R = rl$, we know that $\langle V^2 \rangle$ will scale linearly with the length of the object and linearly with the temperature of the room. In regular resistive materials the conduction band is partially filled at room temperature, and the number of carriers is roughly constant. The temperature dependence thus comes from the thermal velocity acquired by the electrons. Carrier concentration in semiconductors, in contrast, has an exponential dependence on temperature, governed roughly by $e^{-E_B/KT}$, so the scaling of $\langle V^2 \rangle$ in a semiconductor is not linear in temperature. One can distinguish between different phases of matter just by studying how fluctuations scale with parameters like temperature and system size.

One expects the timescales in disordered systems to be long because they tend to

have a proliferation of small gaps in their energy eigenspace. Many of these systems can exist in a glassy phase [23]. A glass, which is an archetype of a phase of matter that exists in a range of materials, most famously glass itself, has a few distinguishing characteristics. The statistical properties of a glass, including their response to an outside perturbation, such as a fist put through a glass window, depends strongly on the history of the temperature of the glass, rather than just its current temperature. This history can be mapped to something called quasitemperature, which statistically describes the quasicrystalline order that exists in any given glass. On fast timescales a glass looks like a solid, and shatters rather like a crystal might under enormous pressure. But on long timescales it looks more like a very viscous fluid, so that a gentle force like Earth's gravity will gradually thin the tops of windows and thicken their bottoms as the glass flows downwards over the centuries. This is true in part because these systems all have many possible configurations which, while approximately the same energy, have very small cross-sections, which dramatically slow transitions from one nearby lying state to another. The fluctuation dissipation theorem breaks down for glassy systems, which one expects to see in disordered systems, but extensions that describe the relationship between fluctuations and response functions in terms of quasi-temperature and time do exist [39]. To measure those deviations from the fluctuation dissipation theorem we constructed an imaging system with a resolution comparable to our de-Broglie wavelength and healing length at our lower temperatures. The result is a diffraction limited microscope at 780 nm with a numerical aperture of 0.5. Simulations in Oslo calculated the imaging resolution to be about 900 nm when imaging through our glass cell. Our testing was limited to a 1951 USAF test target, and with our $3.75 \mu\text{m}$ pixel size and 5.7x magnification, the 2 pixel wide full contrast transition regions show our resolution to be at least $1.3 \mu\text{m}$.

The backbone of this microscope is a 25mm wide A25-20HPX-DL-B asphere with EFL 20mm we purchased from Asphericon. The lens is designed to be diffraction limited at 780 nm. The stock items they listed at the time did not represent the full quality

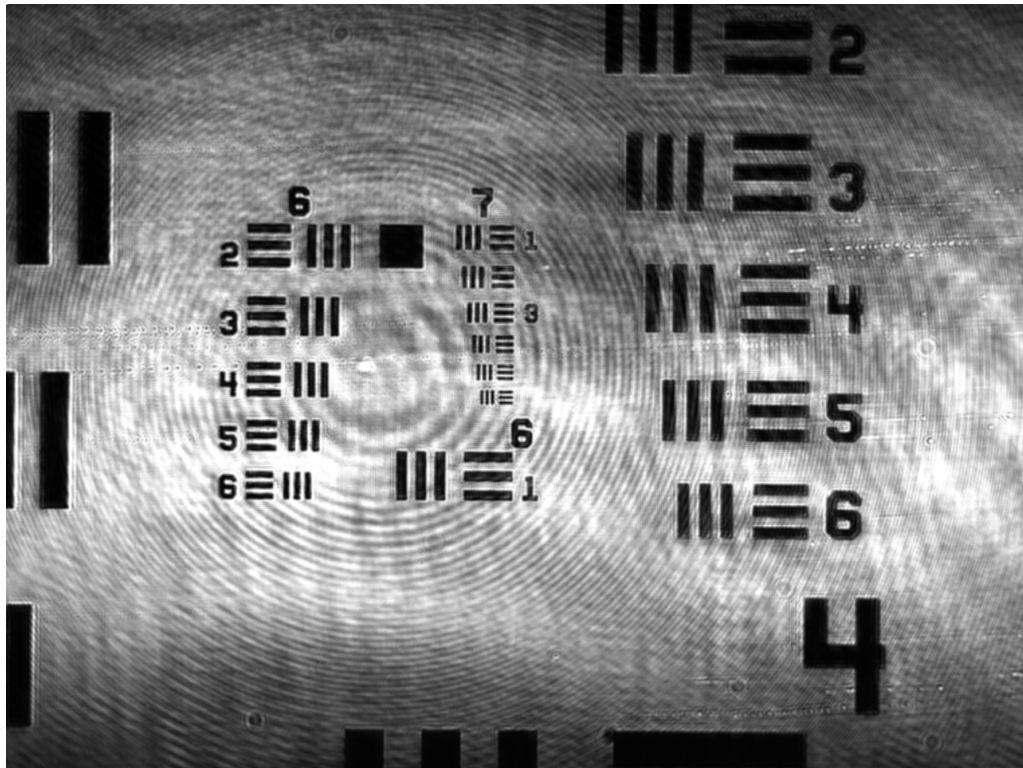


Figure 3.4: A test image captured with our high resolution two lens objective through our science cell wall. Oslo calculates our field of view, before coma starts distorting the image, to be a $140 \mu\text{m}$ wide disk. The field of view here is 847×634 microns, and one can see coma at the large bars on the left side of the image.

range of the products they manufacture, so anyone who wants imaging quality aspheres must inquire directly. We bought one of a small set of very high quality aspheres they manufactured as a product test run. We determined it to be diffraction limited at the full aperture using a short focal length 40x magnification freespace compound microscope objective. They very kindly lent it and an ion polished uncoated reference model as well, for testing purposes. We found the diffraction limited model to be sufficient, and didn't touch their reference model.

The asphere was designed for imaging through air, which is a dramatically different task than imaging through a window at high resolution. The primary source of degradation in our system, without any correction, is spherical aberration. The effect drives from the difference between two trigonometric functions. When a spherical set of rays pass through a window they are deflected according to Snell's law, $n_1 \sin(\theta_1) = n_2 \sin(\theta_2)$. Optical lenses, when designed for beams travelling through air, are designed to deflect into copropagation a ray travelling at angle θ a distance of $f \cdot \tan(\theta)$ from the center of the lens, where f is the focal length. So for two rays traveling at angles θ and ϕ through a piece of glass of thickness d , there will be a differential displacement of $d \cdot (\tan(\arcsin(\frac{\sin(\theta)}{n_{glass}})) - \tan(\arcsin(\frac{\sin(\phi)}{n_{glass}})))$. In air each of those displacements on its own would require a distance d' along the focal axis of $d' = d \cdot \tan(\arcsin(\frac{\sin(\theta)}{n_{glass}})) / \tan(\theta)$ and ϕ respectively. At small angles, where $\tan(\theta) \approx \sin(\theta) \approx \theta$, the n_{glass} term just follows through linearly and the ratio of displacement to focal axis travel remains the same for all rays. But at large angles one gets a differential focal shift between the two rays of $d'_\theta - d'_\phi$. This relative focal shift is spherical aberration. We compensate for the spherical aberration imparted by the glass with a stroke of luck, an achromatic lens that, when used backwards, adds spherical aberration that cancels out the aberration imparted by the glass cell. The lens, at the time, was a CVI Melles-Griot product that was sold by Edmund Optics under part number 49-360. A 25mm lens, it was designed for a 100 mm focal length. Turned around, as it is in our system, its effective focal length is 114 mm. The

total cost of the high resolution imaging objective is less than 700 dollars.

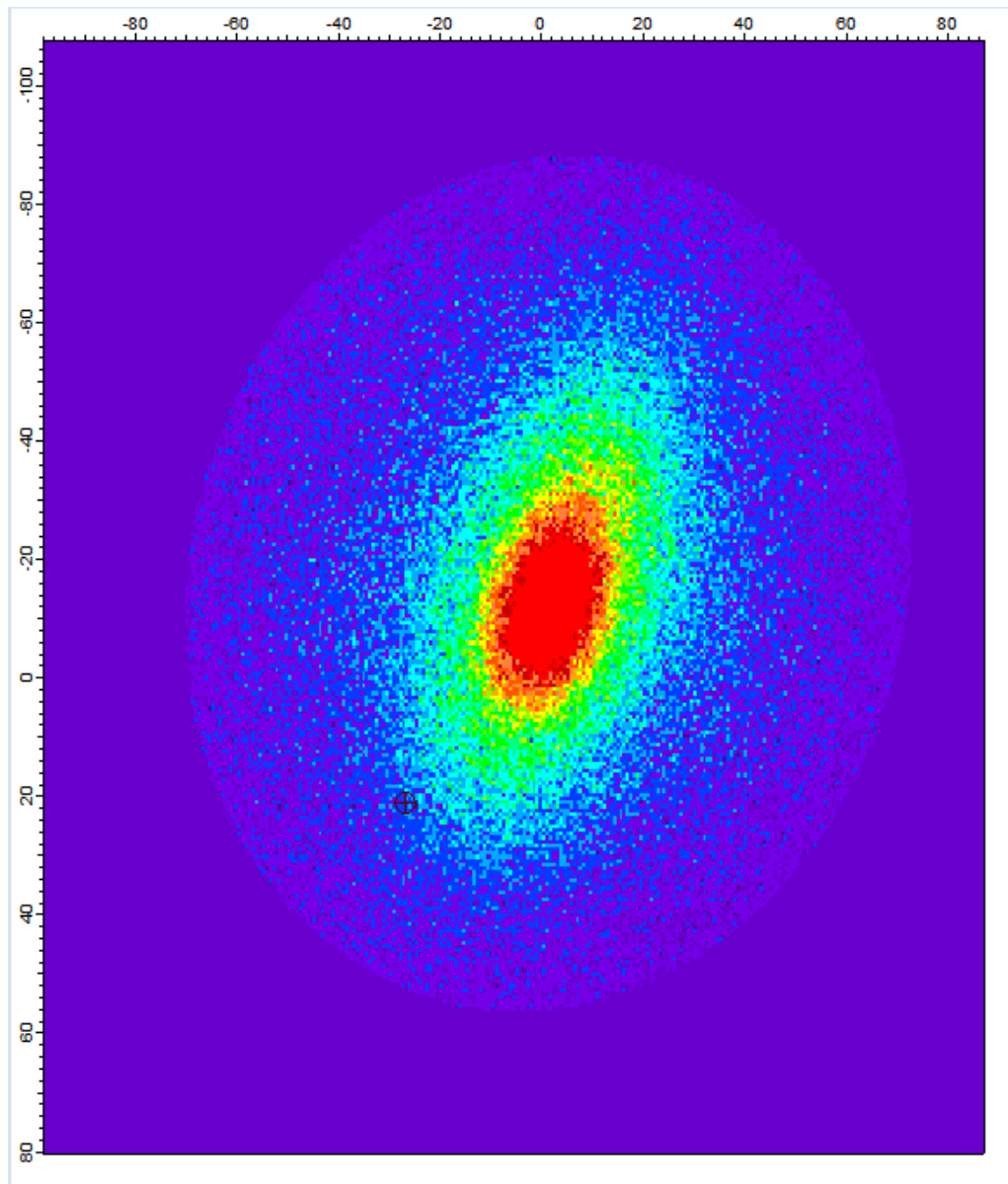


Figure 3.5: An in-situ image of our BEC taken with our high resolution objective with a magnification of 5.7, a Point Grey Flea2g, and a probe sized to be within the diffraction limited field of view.

We constructed a high magnification attachment for our high resolution microscope with a magnification of four. It did not have to be high performing. The object plane of this second microscope requires 5.7 micron resolution while the image plane requires 22.8 micrometer resolution. For the objective portion we chose to use half the aperture of a 25 EFL asphere from thorlabs, and for the imaging lens we used a high performance

plano-convex lens from CVI Melles-Griot. The result is a diffraction limited spot size with a diameter of 6 pixels. When we tested it on its own it had a resolution of $4\mu\text{m}$. To this we later added a number of filters so we could image our atoms in the presence of our lattice light.

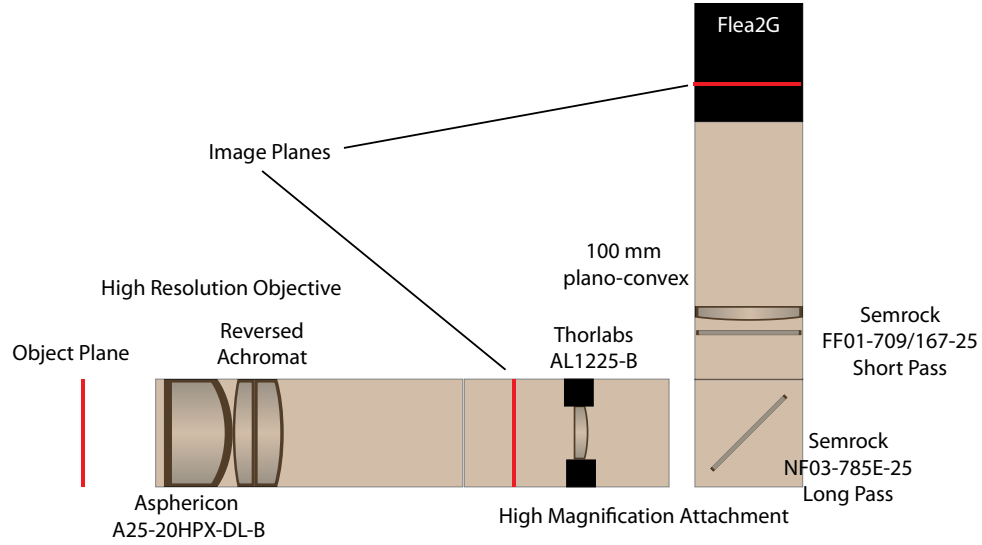


Figure 3.6: This is a diagram of our full in-situ imaging system. The asphere in the high magnification attachment can be swapped out with the CCD to provide a wider field of view and to align the high resolution objective and optical lattice. The Semrock filters remove our 800 nm+ lattices from the imaging line.

3.4 The High Bandwidth Arbitrary Lattice

To study the sliding phase we set out to produce a potential disordered on only one axis. We did not realize exactly how challenging the job would be. We had previously used optical speckle, which requires a phase diffuser, a high NA lens, and intensity control. A beam of intensity $I(x, y)$ passes through a diffuser, obtaining a spatially varying phase $\Phi(x, y)$. $\vec{\nabla}\sqrt{I(x, y)}\Phi(x, y)$ will add perpendicularly to \vec{k}_0 to produce a local wavevector just after the surface of our diffuser, which we can then pass through a lens. The statistical properties of that local $\vec{k}(x, y)$ will determine the spread of the resulting pattern, and

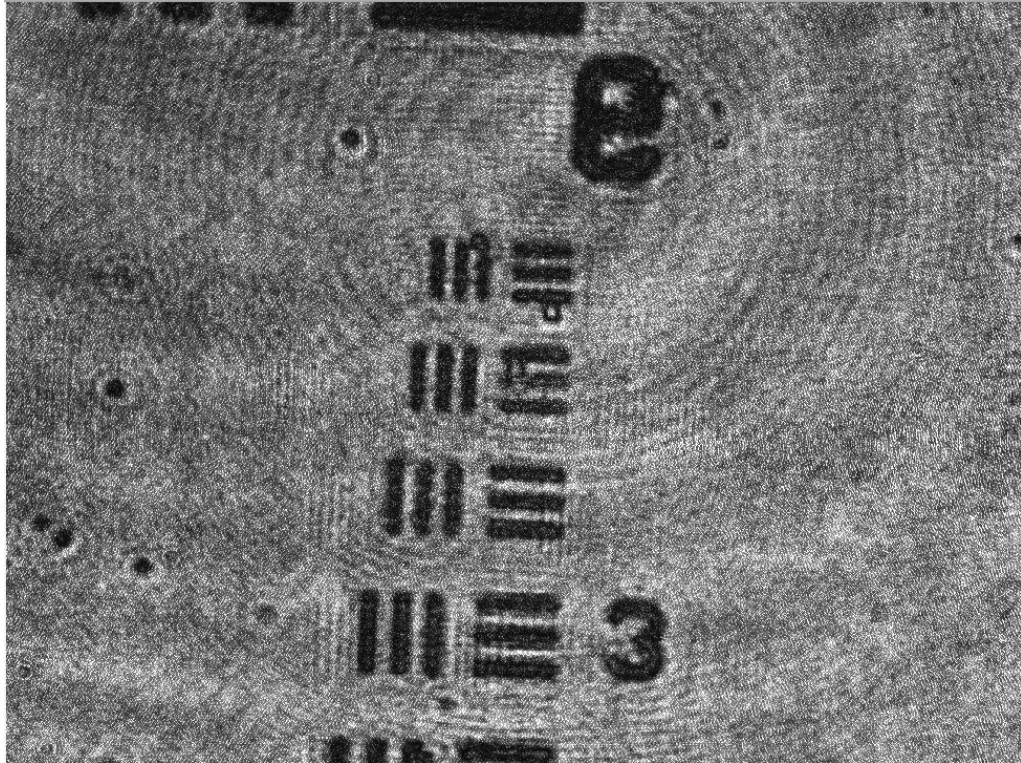


Figure 3.7: An image captured with our high resolution microscope and its long-pass filter high magnification attachment, through the wall of a glass cell of the same manufacture as the science cell in our setup. We have been unable to detect any distortion of the glass cell due to vacuum pressure, and simulations in Oslo suggested slight distortions wouldn't be problematic at our NA. The thinnest bars in this image of a Thorlabs 1951 USAF test target are from Group 7, Element 6, at $2.19 \mu\text{m}$ wide. The test target has quite a few dings. The sharp response indicates a resolution near a μm , with some local distortions. The out-of-focus bars in the image are an etaloned out of focus image from our CCD cover glass. Our long pass 795nm edge filter is not specified as imaging quality.

the numerical aperture will determine the gaussian width of the autocorrelation function of that pattern, which should match the diffraction limit of the aperture the lens is used to focus. One can make highly anisotropic patterns by illuminating a speckle pattern with an elliptical aperture instead of a circular one. And a speckle pattern in which $I(x, y) \approx I(x, y + a)$ can be produced with a cylindrical lens and a similarly anisotropically diffuser. But this technique has a drawback. The intensity of an optical field whose fourier decomposition has more than one component will also vary along the imaging axis.

We can restrict ourselves to uniform polarization and say that, for a monochromatic field,

$$I(x, y, z) = \left(\sum_{\vec{k}} A_{\vec{k}} e^{i(\vec{k} \cdot \vec{x} - \omega t)} \right) * \left(\sum_{\vec{k}} A_{\vec{k}}^* e^{-i(\vec{k} \cdot \vec{x} - \omega t)} \right) \quad (3.6)$$

A one dimensional lattice will be generated if we choose two k vectors. It will have a gradient along $\vec{k}_1 - \vec{k}_2$, and if we allow ourselves the unrealistic case of uniform illumination, it will have no intensity gradient in the plane perpendicular to this vector. If we choose to overlap a pair of Gaussian beams, we can approximate the gradient in that plane as an anisotropic parabola, which gives rise to the harmonic oscillator approximation so common to those using optical traps. We can make the trap minimally more interesting by adding a third beam.

$$(\vec{k}_1, \vec{k}_2, \vec{k}_3) = (\sqrt{k^2 - k_y \hat{z}} - k_y \hat{y}, \sqrt{k^2 - k_y \hat{z}} + k_y \hat{y}, \sqrt{k^2 - 2k_y \hat{z}} - 2k_y \hat{y}) \quad (3.7)$$

Plugging this into equation 3.6 will yield periodic trig terms with gradients along $\vec{k}_1 - \vec{k}_2$, $\vec{k}_1 - \vec{k}_3$ and $\vec{k}_2 - \vec{k}_3$, where we can now only identify a vector of uniformity, where the planes orthogonal to these sets of vectors intersect. One dimensional optical speckle can be constructed by randomizing the amplitude, number, and phase of a set of \vec{k} spanning one axis, with a cutoff in angle determined by the aperture of the lens used to create the

pattern. That set of wave vectors will produce gradient vectors pairwise, most of which will project to some degree along the imaging axis, creating a disordered potential along that direction. The rule of thumb is to follow the behavior of a gaussian beam properly focused at the diffraction limit. So with $780nm$ light with a Gaussian width of $1\mu m$ being analogous to optical speckle with a $1\mu m$ correlation length, so too is the Rayleigh range $z_R = \pi\omega_0^2/\lambda = 4\mu m$ analogous to the correlation length of the disorder along the optical propagation axis. The minimum dimension of any monochromatic disordered potential is 2.

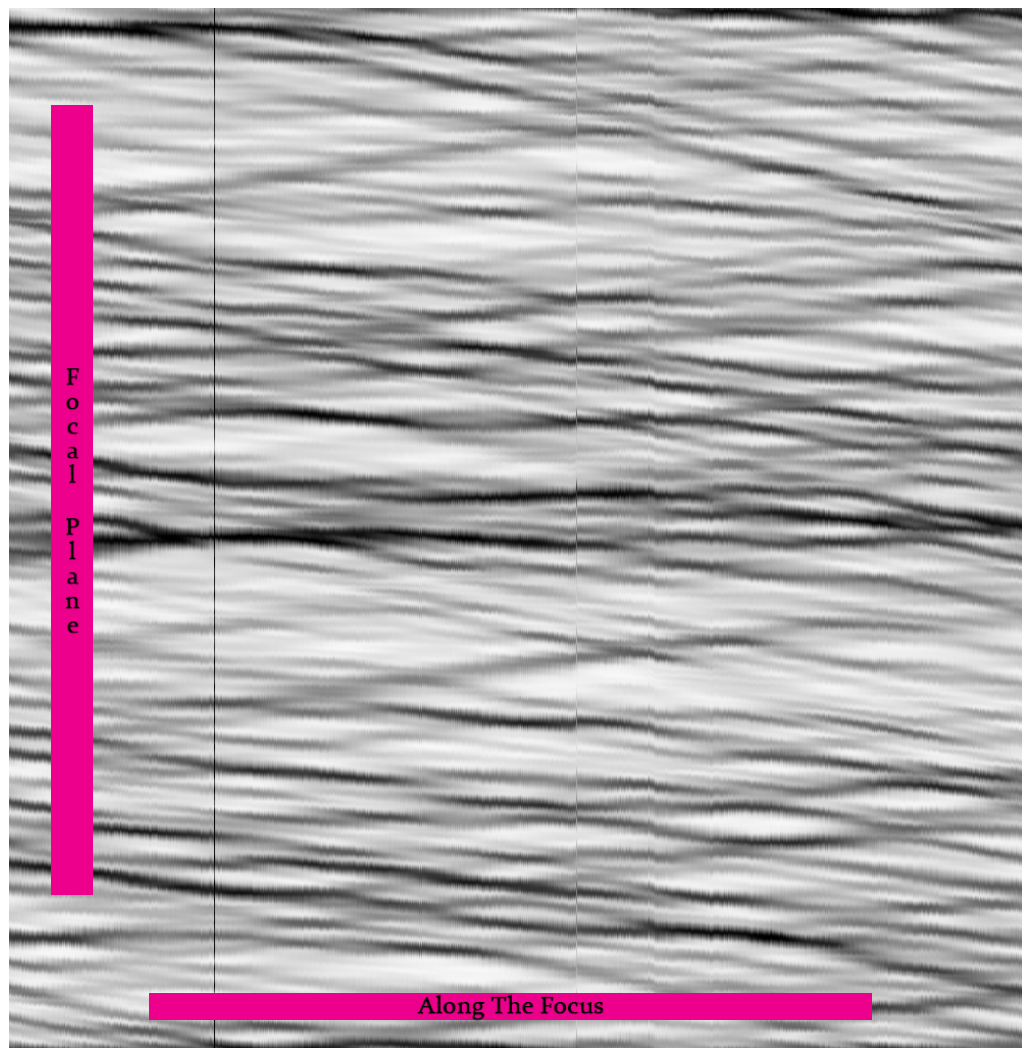


Figure 3.8: A series of pictures through the focus of a one dimensional speckle field created with a phase diffuser and a cylindrical lens.

Our goal was to study BKT physics with disordered coupling between planes, and with sufficient coupling that we could achieve a measure of coherence across the entire cloud. To produce one dimensional optical speckle with a sufficiently long correlation length along the pancake to produce slightly staggered, but single pancakes, would have required a UV field.

The goal was as follows, where every k^\top is transposed from k across the same plane, defining the two dimensional isotropy of the potential.

$$I(\vec{x}, t) = \left(\sum_{\omega} A_{\omega} (e^{i(\vec{k}_{\omega} \cdot \vec{x} - \omega t + \phi_{\omega})} + e^{i(\vec{k}_{\omega}^{\top} \cdot \vec{x} - \omega t)}) \right) \left(\sum_{\omega} A_{\omega} (e^{i(\vec{k}_{\omega} \cdot \vec{x} - \omega t + \phi_{\omega})} + e^{i(\vec{k}_{\omega}^{\top} \cdot \vec{x} - \omega t)}) \right)^* \quad (3.8)$$

This represents a multichromatic set of shallow angle lattices which all follow the same direction, $\hat{k}_{lattice}$, which is perpendicular to the plane of transposition. A full expansion shows that running lattices do exist between cross terms. Let us consider the case with two different shallow angle lattices. The intensity is as follows.

$$I_d(\vec{x}, t) = 2 \left(A_1^2 + A_2^2 + A_1^2 \cos((\vec{k}_1 - \vec{k}_1^{\top}) \cdot \vec{x}) + A_2^2 \cos((\vec{k}_2 - \vec{k}_2^{\top}) \cdot \vec{x}) \right. \\ \left. + 4A_1A_2 \cos((\vec{k}_1 - \vec{k}_1^{\top}) \cdot \vec{x}/2) \cos((\vec{k}_2 - \vec{k}_2^{\top}) \cdot \vec{x}/2) \cos(t(\omega_1 - \omega_2) + \frac{1}{2}(\vec{k}_1^{\top} + \vec{k}_1 - \vec{k}_2^{\top} - \vec{k}_2) \cdot \vec{x}) \right) \quad (3.9)$$

The two regular shallow angle lattice terms are straightforward, but the cross term, which occupies the second line, is a bit strange. This cross term varies in two dimensions at any given slice in time. The first two cosine terms create a gradient in $\hat{k}_{lattice}$, and are a pair of terms modulated at half the period of each of the two regular shallow angle lattices. These are modulated by a third cosine, which is a running modulation of the field along the imaging axis, perpendicular to the direction we choose to engineer. The third, two dimensional term is time-averaged out to zero at the beat frequency of the bichromatic

lattice.

$$\int_0^{\frac{2\pi}{\omega_1 - \omega_2}} I_d(\vec{x}, t) dt = \frac{\pi}{2} (A_1^2 + A_2^2 + A_1^2 \cos((\vec{k}_1 - \vec{k}_1^\top) \cdot \vec{x}) + A_2^2 \cos((\vec{k}_2 - \vec{k}_2^\top) \cdot \vec{x})) \quad (3.10)$$

At a small enough difference frequency the time dependent term will matter. In order to evaluate the effects in a specific multichromatic lattice one would solve for the eigenspectrum of the time averaged potential and then use time dependent perturbation theory to evaluate the contribution to the Hamiltonian. It is straightforward to see one can get strong resonant effects if one modulates the entire potential in narrow bursts at the rate of the difference frequency, selecting out some precise value of $(\omega_1 - \omega_2)t$. At sufficiently low Δf the drive can dress trapped states of the system. And at very low frequencies the atoms would just follow the moving lattice and be shoved out of the system along $\vec{k}^\top + \vec{k}$. In order to avoid all these regimes any pulses must average over tens of periods of the difference frequency, $1/\Delta f$, and $2\pi\hbar\Delta f \gg U_{max}$, where U_{max} is the depth of the total trap. The latter condition ensures the only states coupled by the time dependent term are free particle states, which oscillate quickly in space. The first order term in the time series will be vanishingly small.

We produce this type of potential with arbitrary control over a whole range of reciprocal lattice vectors and a sufficiently wide chromatic range with a pair of high bandwidth AOMs. The central idea is to relay image the diffracting volume of each AOM onto the same spot. One can drive the pair of AOMs with a range of frequencies, which create acoustic sound waves with wavevector $=\omega/c$, where c is the speed of sound in the material. These sound waves are longitudinal compression waves, and in acousto-optic materials the strain tensor is coupled directly to the optical impermeability tensor, so compression waves are also index of refraction waves [40]. When the Bragg condition is met at an angle $\theta_B = \arcsin(\frac{k_{acoustic}}{2nk_{opt}})$, the photons in the laser field can pick up phonons in the AOM's compression wave to shift their phase, energy and momentum. The phase

shift is determined by the phase of the acoustic wave. One can see this by considering the derivation of Bragg diffraction. Diffraction occurs when partial reflections off of a crystal lattice add up in concert. Consider a set of layers at spacing d of thickness $20d$. Light of wavelength λ will diffract when $2d/\sin(\theta) = n\lambda$, where n is an integer. Upon entering and leaving the material the phase of the light accumulated will always be a multiple of 2π . But compared to some point in freespace a distance h from the surface of the volume, that $n\pi$ phase shift will begin at relative phase $\pi h/\sin(\theta)\lambda$, so the total relative phase accumulated before the beam returns to that height is dependent on the position of the grating. In our system the grating is the phonon, and it can be considered to begin and end at peaks in the compression over the overlap volume of the compression wave and the beam. So if we modify the phase of the acoustic wave we modify the effective position of the grating, and modify the phase of the output beam. The phase of the optical lattice, ϕ_ω , can therefore be controlled by controlling the relative phases of two acoustic waves that travel through the pair of AOMs.

Our AOMs were manufactured by IntraAction, model ATD2003AK2.780. They are specified to work with a relatively flat response between 150 and 250 MHz with a 2 Watt drive. There was some miscommunication during the ordering process and so we received a lower bandwidth than we were after. After discussing them with John Lekavich and extensive, incremental testing, we settled on driving them between 135 and 270 MHz at a maximum of 3W. The high frequency range benefits from the added power, the low frequency range not so much. The apertures are 2mmx6mm, so we can diffract nice broad beams.

In general AOMs as broad bandwidth deflectors use a crystal axis with a slow speed of sound. This allows large acoustic wavevectors, which in turn allows large deflections, at relatively low drive frequencies. Other groups report injecting these with a large set of frequencies to produce large sets of beams, whether they are shaping custom potentials or creating arrays of microtraps, and part of the trick is that the relative phases of all their

drive frequencies are sufficiently disordered that $P \sim E^2 \neq (\sqrt{P_1} + \sqrt{P_2} \dots)^2$, so they are less vulnerable to any peak power problems. We are interested in controlling the phases of our optical field, which are determined by the phases of our acoustic fields, so this option is not available to us. And because we want to be able to have as many simultaneous lattices as possible, we need to consider the power diffracted into a first order beam as a function of RF power.

$$P_{opt} = \sin\left(\frac{\pi}{2} \sqrt{\frac{P_a}{P_{sat}}}\right) \quad (3.11)$$

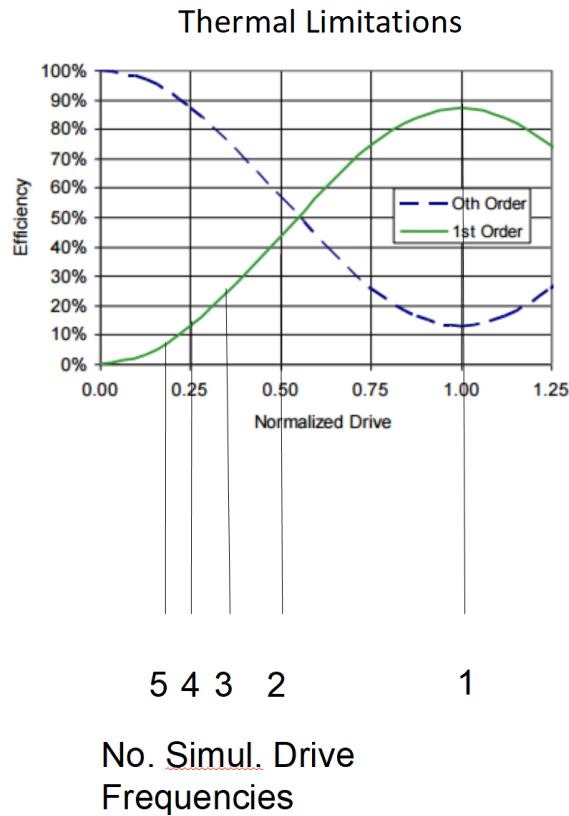


Figure 3.9: As we increase the number of frequencies and stay under the RF power limit we drop out of the linear regime into a region of sluggish response.

This function has a linear response when the acoustic power P_a is between $.25$ and $.75 P_{sat}$. The response is small below $.1 P_{sat}$, so if we want to drive ten frequencies at the same time and avoid overdriving our AOMs our total diffraction efficiency will be untenable. Instead, in order to maximize our diffraction efficiency, we use a train of

pulses. Each is at P_{sat} , so we can use our laser power as efficiently as possible. We vary how deep each lattice is in the time averaged pulse train by varying how often we pulse any given beam before the pattern repeats itself. This requires AOMs that work on the fast axis to avoid unintentional periodic driving effects. In our current setup we use 300 ns pulses, which puts the time-dependent perturbation from the pulse itself up at the 3 MHz energy scale, and our rep rate is never below 100 kHz, which keeps us well above both the depth of our optical potential and the lower band manifold by a factor of 50. The repetition rates of our higher recoil energy lattices are higher than the repetition rates of our smaller wavevector lattices to avoid deviations from a time averaged potential in our disorder.

For our disordered many-lattice experiment we produce our RF fields with a pair of Tektronix AWG2040s. They are old fashioned arbitrary waveform generators (AWG) that can output 8 bit numbers at 1.024 gigasample per second (GS/sec). We bought our first on ebay for a few hundred dollars. The modern and far more capable equivalents cost tens of thousands of dollars. We pass their outputs through a 300 MHz filter to suppress digitization noise and then amplify them through a pair of MiniCircuits ZHL-03-5WF+. We chose a five watt amplifier so we can stay in the linear region of its response function and still have overhead for the RF power. We run two AWGs in a master-slave configuration, so they run off the same clock and the start times of their waveforms are coordinated. This allows us to produce a large set of optical lattices with arbitrary relative phases. We can even offset the entire waveform on one AWG from the other to account for the differing distances our phonon fields must traverse through the AOM before they reach our optical beams.

This is sufficient for producing a set of beams for our disordered lattice, which really does not require specific tones, but it has its limits. While the AWG would be within the Nyquist limit for observing signals over our entire bandwidth, the Nyquist limit is insufficient for producing good oscillators. Let us consider Bragg spectroscopy. To

produce a lattice moving at some speed $v = \phi_d t/k$ we would need two tones for our AOMs with a detuning of $\frac{d}{dt}\phi/2\pi$. This speed could be as slow as tens of Hz. We could pulse on this moving lattice for a microsecond, and despite the divergent timescales that velocity would not change. If we consider what our AWG can represent over the period of a microsecond we can decompose this into a linear algebra problem. If we want to produce a lattice that moves at 10 Hz using \vec{k}_{270MHz} , we will need to produce both 270 and 270.000010 MHz signals. If we calculate $\sin(270x) - \sin(270.000010x)$ and look for the first point in time the norm of that difference is $1/2^8$, it's way out at 300us. Similarly a 100 Hz detuning would have a one bit difference in the entire waveform after 30 us. It is thus useless for Bragg spectroscopy. It's simply not a good oscillator for the majority of the spectrum. We have employed PLLs to make some running lattices, with resolutions down in the Hz range, and I will discuss them in the future directions section.

Our disordered lattices currently have wavevectors that range from 5.5 μm to 1.3 μm , with a recoil energy that ranges from 1.35 kHz to 7.58 Hz. Those energy bands are closely spaced, and the pairwise gaps opened up by absorbing from one lattice and emitting into another are at the Hz level. This means even the slowest changes in our potential, rather than being adiabatic and reversible, will be a source of heating. Consequently we've worked very hard to make this lattice very stable. As with other optical arrangements near the cell every optic in the lattice setup is on one aluminium breadboard. Cage cubes are used in tandem with minimally spaced 1" posts where possible. The number of optics was minimized. The aluminium breadboard is clamped to the optical table by four short posts. The results were insufficient; there was too much phase jitter between the two arms of the lattice. However, as we discuss below, we solved the problem with active stabilization.

We use a thorlabs fiber coupler to launch light out of a PM fiber designed for 780. A pair of walking mirrors follow to allow simultaneous alignment with the apertures and primary axes of two AOMs and the optical arrangement: the height of the laser beams is kept a constant distance from the optical breadboard to within the uniformity

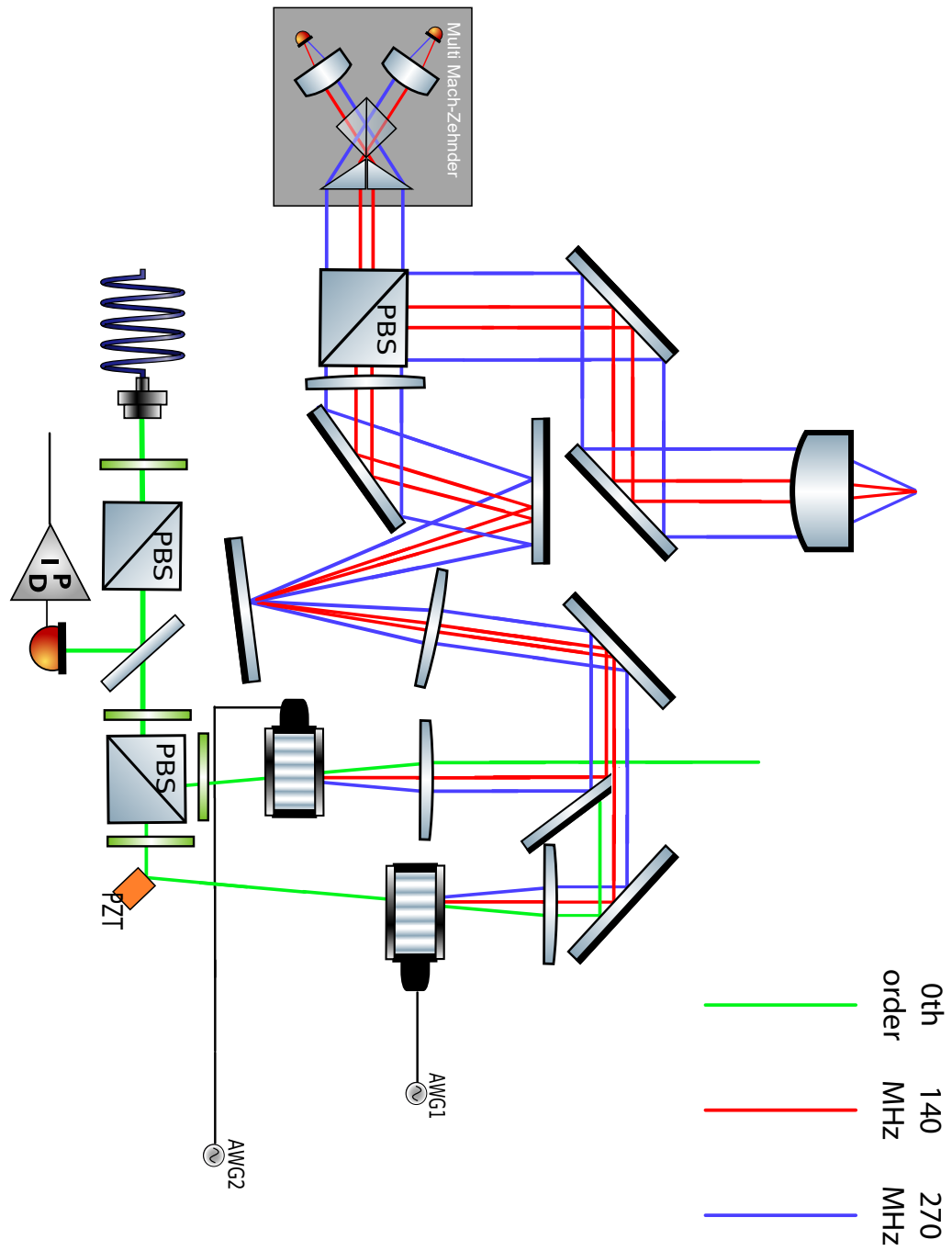


Figure 3.10: This shows, mostly to scale, how we construct our HiBAL. The two arms of our lattice generator, which pass through our two AOMs, are length-stabilized with a piezo-mounted mirror. The actual lattice is realized with an asphere.

of the breadboard. Vertical deflections of the beam paths are not compatible with our optical potential. After the walking mirrors we polarization stabilize with a PBS, intensity stabilize with a pickoff, intensity balance with a half waveplate and a PBS, and align the polarizations with a pair of half waveplates. After the second PBS there are two paths for the two AOMs. One of the two paths passes through an AOM and a lens, then gets recombined with the second arm. The second arm, however, uses two mirrors for alignment. After recombination every beam in the lattice passes through the same optics as every other beam. Contributions along this part of the optical path to dynamic dephasing are so small as to be unmeasurable. Phase noise is not introduced past this point. But because the lattice is split briefly into two paths the lattice's phase, uncorrected, is completely unstable.

We measure the phase stability of our lattice with an unusual Mach-Zehnder interferometer. We were concerned about adding phase noise to our lattice by trying to correct deviations imposed by acoustics within the interferometer itself, so we chose to put all the optics on a single piece of metal to make it as monolithic as possible. We use a pair of prisms to deflect the two arms of the lattice towards a beamcube, and each sublattice has its own little spot on that beamcube where the phase measurement is made. The signal is then deflected up by a pair of prism mirrors, where it is then directed by disconnected mirrors onto a pair of photodiodes, Thorlabs PDA100s. As manufactured the photodiode coverglass distorted our interferometer signal through etaloning. Zach and I removed that glass, each in our own way. He disassembled and resoldered his. I went at mine with a hacksaw. Both are still in the experiment. When our interferometer is aligned it measures the relative phases, pairwise, of each set of lattice beams.

In a normal lattice the recoil energy is usually quite large, so some phase noise produces a different quasimomentum. In ours phase noise changes the shape of the potential, not just its position. A deviation in the length of the beam path in one arm will add a uniform relative phase ϕ_a to each of the two sets of beams. This will then be

written into the shallow angle lattices, which will individually experience displacements of ϕ_a/k_ω . The differential displacement doesn't just displace the potential, it reshapes it, which would render the study of systems at thermodynamic equilibrium impossible. We can choose to take an inner product of the lattice with itself. We restrict our inner products ranges to the periods of the individual sublattices because $\int \cos(\omega x)\cos(\sigma x) = \delta(\omega, \sigma)$. For more than one k_n a Δx cannot be chosen to restore the inner product of the whole set to 1 in the presence of some phase offset ϕ .

$$\sum_n \int_0^{2\pi/k} \cos(k_n x)\cos(k_n(x + \Delta x) + \phi) = \tag{3.12}$$

$$\sum_n \pi \cos(\Delta x \cdot k_n + \phi) + \frac{\sin(2\pi k_n) \cos(\Delta x \cdot k_n + 2\pi k_n + \phi)}{2k} \tag{3.13}$$

This needed to be fixed, and we needed to ensure that it would be fixed for all lattices simultaneously.

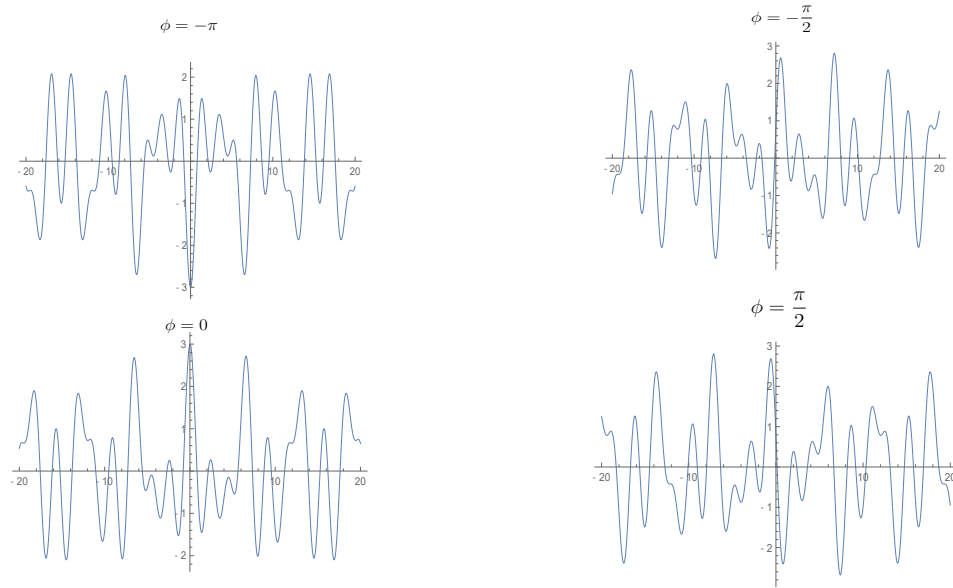


Figure 3.11: Above I have $\cos(x + \phi) + \cos(2x + \phi) + \cos(2.8x + \phi)$ at several choices of ϕ , demonstrating that phase shifts between the two arms of our lattice would change the shape of the potential rather than just translate it.

It is common for lattice phase stabilization and modulation to be performed by phase

modulating the RF used to feed AOMs that drive diffraction [41]. We cannot do so with our discounted AWGs. Phase modulators don't work identically over a large bandwidth. Inserting a time delay into the AWGs clocks would not work either for reasons similar to those described above. A translation in time of the RF drives would shift each drive frequency at $\Delta t/\omega_k$, causing another differential shift in phase instead of a uniform shift.

We went with a direct approach by piezo-actuating one of the two beam paths. We attempted to emulate [42] to get high bandwidth control but mostly failed to do so. For reasons that are unclear to us we were nowhere near as successful in suppressing resonances in the piezo mount. We measured the effects of our stabilization scheme using

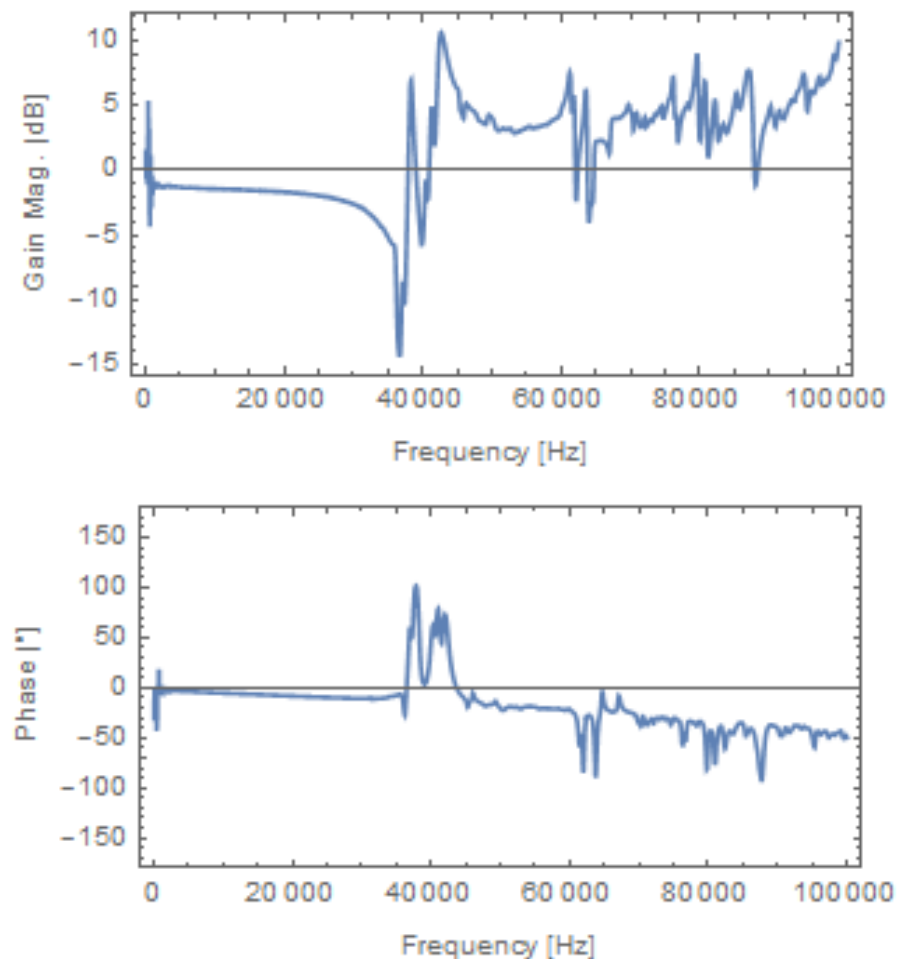


Figure 3.12: The amplitude and phase response of our piezo mirror as measured with a Michelson interferometer.

our Mach-Zehnder and our in-situ imaging system. We eliminate phase noise in our lattice to be smaller than .04 radians, which on our longest wavelength lattice is a displacement of 30 nm.

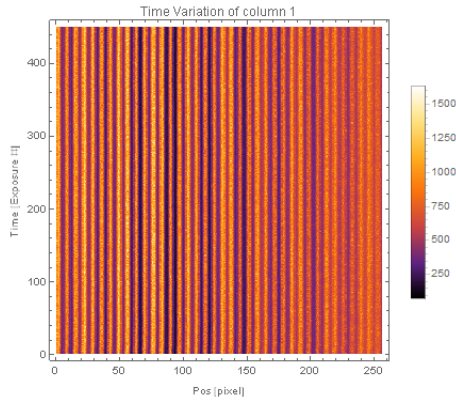


Figure 3.13: This is a multifrequency phase locked lattice imaged with our in-situ microscope onto our Flea2g and shuttered at 200Hz, each horizontal line is a different time step.

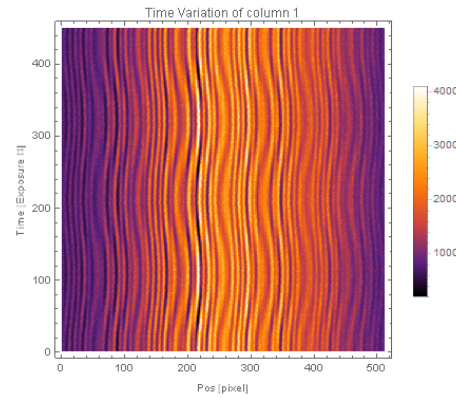


Figure 3.14: A dataset taken in the same manner as 3.13, but without the phase lock the optical potential wanders about, as in 3.11. Equilibrium physics isn't possible here.

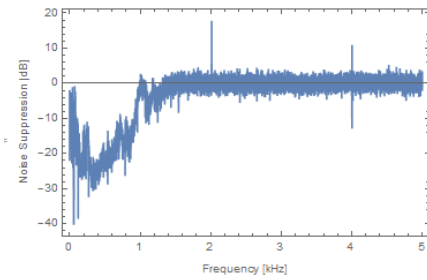


Figure 3.15: We suppress noise out to 2 kHz, where we have our first resonance in the piezo mount.

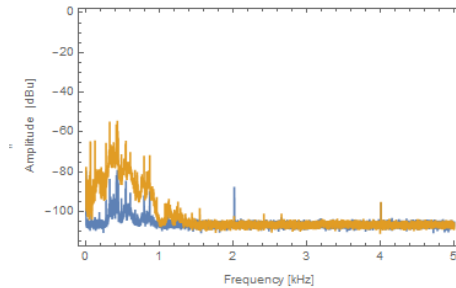


Figure 3.16: This shows the power spectrum of noise measured by our novel Mach-Zehnder interferometer, both locked and unlocked.

3.5 Levitation Coil

Time of flight measurements are often restricted by the space available in a vacuum chamber. Some groups have gone to great lengths to study atoms free of the influence of gravity [43], while others can compensate for it using the linear magnetic field gradient in their quadrupole coils [18] or water cooled levitation coils [13]. A levitation coil is a turn

of wire that utilizes the Zeeman shift and its gradient to create a potential to counteract gravity, and its form is as follows.

$$m_{FgF}B_z = \frac{\mu_0}{2} \frac{R^2 I}{(z^2 + R^2)^{3/2}} \quad (3.14)$$

$$-\nabla_z m_{FgF}B_z = m_{FgF} \frac{3\mu_0}{2} \frac{R^2 I z}{(z^2 + R^2)^{5/2}} \quad (3.15)$$

Our atoms are magnetically trapped in the low field seeking state in the chamber, and we provide a quantization axis with permanent magnets to maintain our spin polarization. In order to better resolve the momentum distributions of our clouds we utilize the Zeeman shift in the F=1 manifold using a levitation coil with a novel system that requires very low power.

Our all optical trap and microscope arrangement is tightly packed and leaves little room for any water-cooled coils. Instead we use a small coil of 16 gauge wire. It's held just under the cell centered on the vertical imaging axis by a piece of fiberglass. We use a bank of supercapacitors gated with MOSFETS to put hundreds of amps through the coil. The circuit itself was designed and built by Aaron Stahl (undergraduate), and the details will be in a future paper. Its current implementation has a capacitance of 930 Farads. It's designed to levitate the atoms for up to 200 ms with a relatively constant current, but we've found the best SNR in the current experiment is achieved at 50 ms TOF. Its ability to provide bursts of hundreds of amps at relatively constant current while powered by a 10 W power supply is a novel and effective design that can turn an easily obtainable phone charger into a kilowatt linear supply for a number of applications. Uncooled coils are limited by the fusion current of the wire in question on the time scale of the pulse. Shorter pulses allow higher currents. For actively cooled coils the limit will be set by the choice of supercapacitor.

3.6 Microwaves

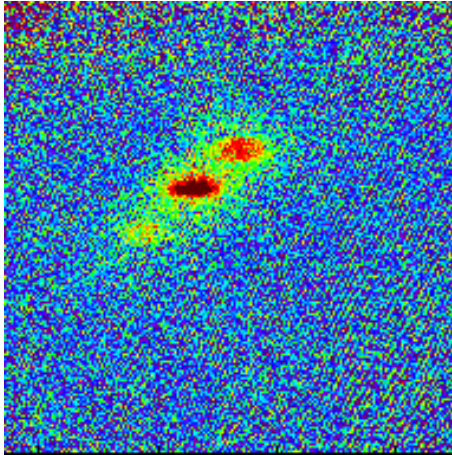


Figure 3.17: A mostly $m=0$ cloud

As discussed at the end of chapter 2, the transfer to the cell passes the atoms through a variety of magnetic field profiles in the presence of stray RF fields. The combination tends to depolarize atoms during the 300 mm transfer to the cell. The depolarization is obvious in TOF when we use our levitation coil. Our interest has been in $U(1)$, and spin mixtures would put us into entirely new phase diagrams. Using some rare earth magnets to adjust the magnetic field along the atomic transfer path we minimize the spin depolarization. We further implemented a microwave system to purify the sample before evaporating down to degeneracy. We used the microwaves to characterize the magnetic field by using it as a repump from $F=1$ to $F=2$, and found the magnetic field from the permanent magnet to be 3.54 Gauss at the cross trap. This separates our transitions by 2.47 MHz, which we measured with our microwave system.

We generate our microwaves with a PLL evaluation board, the ADF4350EB1Z. We've also used these to produce Raman beams on our HBAL. They are fractional PLLs and range from 140 MHz up to the 3 GHz region. We clock it with an Agilent 33220A function generator, and sweep the clock with its analog sweep control. This we pass to a ZX90-2-50-S+ to double the frequency to the 6.8 GHz $F=1, m_f=0$ to $F=2, m_f=0$ transition,

and filter it with a VHF-5500+. We then run the signal through a preamp, a ZX60-8008E=S+, an attenuator. Our power comes from an HP 493A Microwave Amplifier, a travelling wave tube amplifier (TWT). We then use a directional coupler, the ZADC 13-73-S+ and a CS-6000 circulator to monitor back reflections and protect our electronics. We then use an ebay-bought NARDA 903n s/n323 double stub tuner to impedance match our circuit to our 206476 SMA+ waveguide, kindly donated by Rb1.

To purify our clouds we sweep our microwaves across the F=1 to F=2 transition for states we want to eject. We then blast them away with F=2 to F=3 probe light. The relative scattering rate of our 6MHz wide probe beam and our 6.8 GHz detuned F=1 atoms is nominal and does not depolarize our F=1 atoms to a degree we can image.

Chapter 4: The Sliding Phase

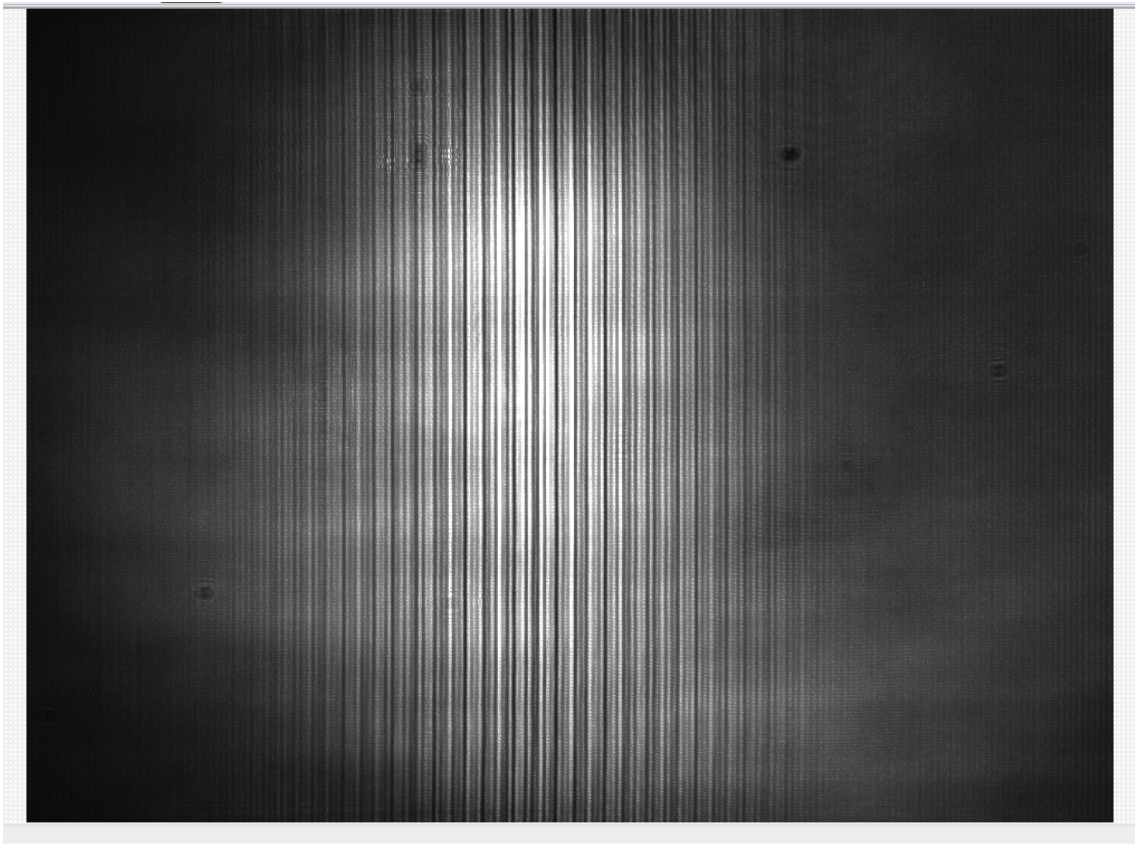


Figure 4.1: A picture of one of our disordered lattices, taken with our high magnification imaging system. Much of the vertical banding is etaloning in our CCD cover glass. We've confirmed this by measuring the same lattice with different flea2gs.

A trio of papers earlier this decade inspired our current experiment [24] [25] [26]. They used computational tools to explore the phase diagram in three dimensions in a $U(1)$ system of coupled, randomly sorted stacks of different two dimensional materials. Absent disorder these systems would undergo the BKT transition in-plane at T_{BKT} and then establish superfluidity, superconduction, or net magnetization in the third dimension

at a lower temperature. Mohan et. al. considered randomly stacked layers of a pair

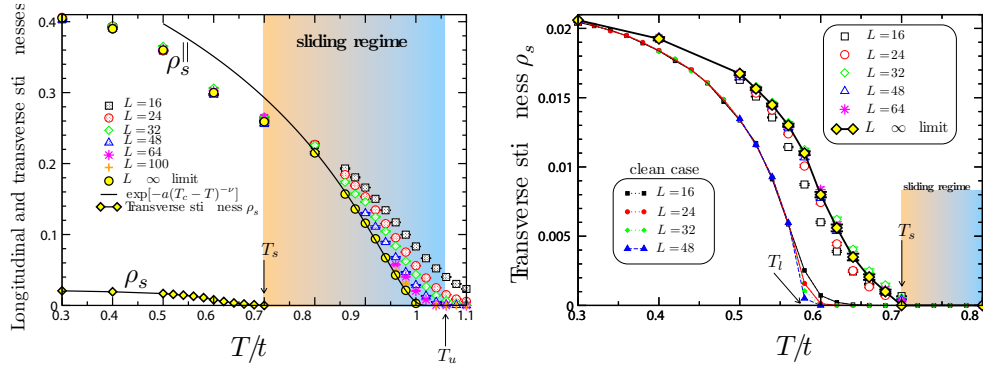


Figure 4.2: Taken from Nicolas Laflorencie’s Monte Carlo paper, this demonstrates the difference between a disordered system on the left and a clean system on the right. The in plane and perpendicular phase stiffnesses ρ_s scale differently at the transition and have different transition temperatures.

of materials and identified three distinct phases of matter below the two-dimensional critical temperature through scaling arguments [26]. Pekker et. al. found roughly the same behavior using RNG theory on a system of stacked layers of harmonically trapped superfluids with random chemical potentials on the boundaries of the quasi-2D regime [25]. Nicolas Laflorencie used monte carlo simulations to study a binary material system as described in the Mohan paper with hard core Bosons at half filling. All identify the emergence of two-dimensional superfluidity, via the BKT transition, at higher temperature than full three dimensional superfluidity, which emerges as a first order transition distinct from a BEC transition. The Monte Carlo study identified one intermediate phase, and the renormalization group and scaling argument studies identified two. All identify the intermediate region as a Griffiths phase, defined as a phase of matter whose behavior is dominated by the most extreme deviation of the disordered crystal from its average. This intermediate phase has been called the sliding phase since the observation of two-dimensional superconduction in bulk copper cuperate superconductors before the onset of three-dimensional superconduction at lower temperatures. In the case of disordered coupling of superfluid pancakes, the transition temperature and scaling of the superfluid fraction in the Griffiths phase would be determined by the weakest link between coherent

subsystems.

If we assume we can take our Wannier states to describe our pancakes as distinct and local objects, we consider the full Hamiltonian in the appropriately named tight binding approximation, where m is the mass of the particle, V_i is the depth of an individual pancake's trapping potential, \tilde{g}_i is the effective interaction energy of the pancake due to the local compression, ω is the harmonic trapping frequency due to our 1550 nm trap, $\Delta\omega_i$ is the deviation from that trap due to the local depth and curvature of the lattice, and $J_{i,j}$ is the hopping term between any pair of planes.

$$\hat{H} = \sum_i \left(\frac{\hat{p}_i^2}{2m} + V_i + \tilde{g}_i \psi_i \psi_i^\dagger + \frac{m}{2} \hbar^2 (\omega + \Delta\omega_i)^2 (x^2 + y^2) - J_{i,j} \psi_i^\dagger \psi_j \right) \quad (4.1)$$

This allows us to map a series of quantities using the LDA to the parameters characterizing the disordered systems described in the three theory papers. Our system exhibits disorder in three local parameters. The coupling from one pancake to the next is disordered. The local compression, and thus the local \tilde{g} , is disordered. And the local number varies due to a varying local site depth. Our system is thus most similar to the model in [25].

Pekker et al identify the sliding phase as a pair of Griffiths phases whose behaviors are dominated by the rarest region in the system. They identify a regime where isolated coherent layers separated by regions of normal gas pancakes are able to establish some mutual coherence that produces a vanishingly small but finite phase stiffness along the lattice axis. The point where this happens and the scaling of the stiffness is set by the weakest link in the chain of pancakes.

With our HiBAL system we can create a highly anisotropic system, composed of coupled pancakes of Bose gases. Each layer is harmonically trapped, and the range of temperatures and chemical potentials of each layer μ_i span regimes from entirely thermal 3-dimensional systems to coupled quasi-2D systems. We explore a parameter regime

where our quasi-2D trapping parameter, the gap between our different band-manifolds $E_{\vec{k}_{max}}(q = 0)$, ranges from 5.4 to 5.9 kHz, is always greater by a significant factor than the chemical potential of our gas, and always lower than the trap lattice depth. The T_c at which our system exhibits a nonzero two dimensional coherent fraction is around 200 nK, where $\frac{KT}{2\pi\hbar} = 4.16$ kHz, which leaves our thermal gas on the edge of being 2D. In our lattices we have emerging quasi-2D coherence in isolated pancakes coupled by a three dimensional thermal gas, which exhibits excitations perpendicular to the BKT planes on length scales smaller than the spacing provided by \vec{k}_{max} . These coherent planes we relate to the two dimensional Bose gas and its famous infinite-order BKT transition through the local density approximation, as our system's energy scale is significantly larger than the in-plane trapping frequency. $\frac{KT+\mu}{\hbar\omega} > 10$. The minimum ratio of the energy scales for perpendicular in-plane excitations to parallel excitations is 40.

4.1 Our Sliding Phase

Our toolset differs from those of the theoretical studies. Our primary tool is the time-of-flight measurement. Energy scales and the length scales of phase fluctuations in both the theoretical models and our own realization of the Hamiltonian are highly anisotropic, which lead our TOF distributions to be highly anisotropic. We define several terms separately for the in-plane and out-of-plane directions. The in-plane coherent fraction we define as the atoms at low enough momentum that density and phase fluctuations are subsumed into a Castin-Dum like expansion [44] in TOF. We define the ballistic fraction as the atoms that obey the relation $E = \frac{\hat{p}^2}{2m}$ in-plane, beyond the energy scale of Bogoliubov modes. The coherent pancakes are small enough to have a BEC fraction, which will give each an average phase. We use the correlations of the average phases of the various coherent pancakes as a function of temperature and lattice depth as a proxy for phase stiffness along the disordered direction. As a function of temperature we expect to first see the emergence of an in-plane coherent fraction which will emerge as a Thomas-Fermi

distribution on top of a thermal distribution in the in-plane TOF direction. At this point we expect the individual coherent fractions of each pancake to be incoherent with one another, so despite in-plane coherence the interference pattern of the planes will resemble a thermal distribution. This will indicate we have entered the uncorrelated sliding regime, where we have no superfluid fraction in the disordered direction but we do in the other two. The emergence of correlations in the disordered direction will appear as deviations from a thermal distribution. This is not direct evidence of a finite phase stiffness across the entire cloud, but is evidence of the same physics described by Pekker et. al. as order begins to emerge in puddles. According to Pekker et al, "The key signature of the Griffiths phase, in interference experiments, is very strong shot noise which results from the interference of several weakly coupled superfluid droplets." So if our TOF measurements of similar clouds are dramatically different from one another, our sliding phase is also a Griffiths phase. It will not be possible to differentiate the finite phase stiffness sliding phase from the zero phase stiffness sliding phase just from a momentum distribution. For a system of our size we expect a full 3D superfluid to emerge alongside a full three dimensional condensate fraction, along the lines of the momentum distributions calculated by Nicolas LaFlorenchie in his paper in Fig. 4.3.

We use an ROI, a region of interest within the field of view of our camera, that spans beyond $\pm \frac{4\pi\hbar}{(1.3\mu m)(87amu)}(50ms)$ along the lattice, which corresponds to two recoil momenta of our shortest wavelength lattice and the span of our lowest band manifold, and in plane we span twice the widest width measured of any Thomas-Fermi distribution in our dataset ($p_{\parallel,min}, p_{\parallel,max}$). Nicolas LaFlorenchie's work included momentum distributions in his stacked pancake system. They show near-separability of the distributions along p_{\parallel} and p_{\perp} . To enhance our SNR we create a pair of one-dimensional distributions $n(p_{\parallel}) = \sum_{p_{\perp}}^{ROI} n(p_{\parallel}, p_{\perp})$ and $n(p_{\perp}) = \sum_{p_{\parallel}}^{ROI} n(p_{\parallel}, p_{\perp})$. In $n(p_{\parallel})$ a TF distribution emerges below the BKT transition on top of the thermal distribution. In every picture we label $\pm p_{\parallel,TF}$ as the outer limits of the TF distribution, and fit a Gaussian distribution to $n(p_{\parallel})$ over

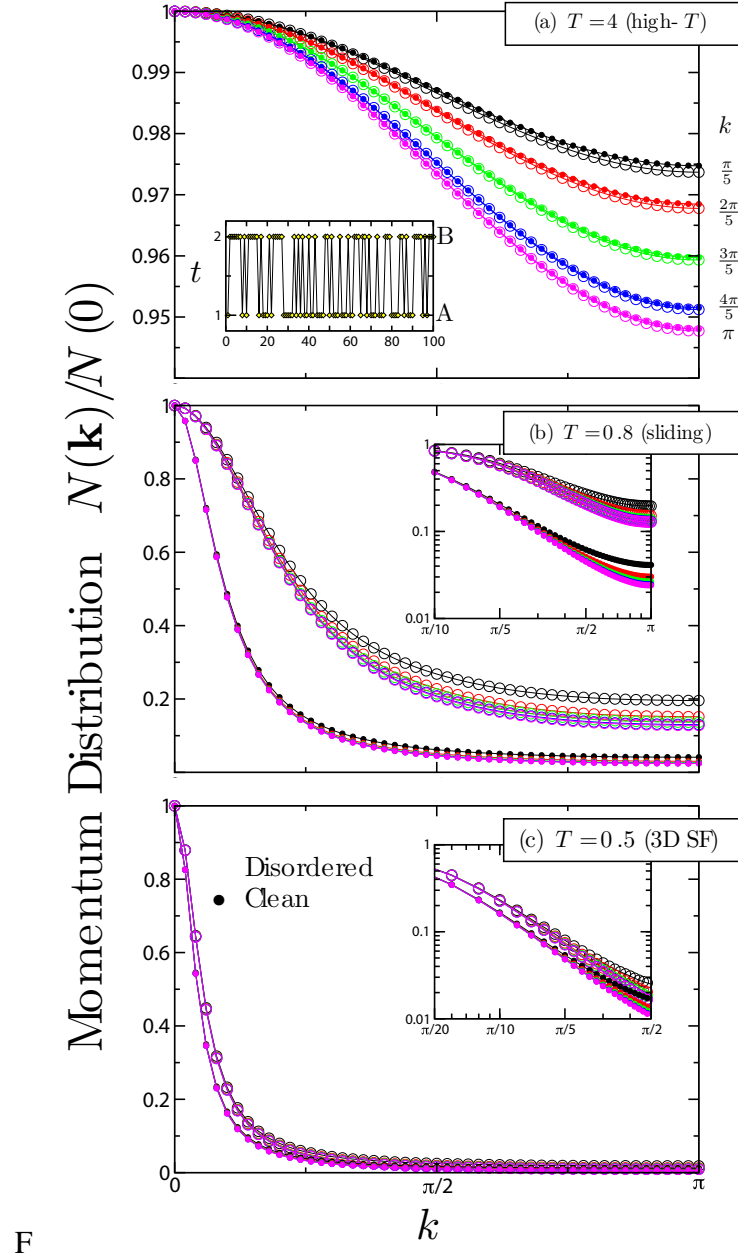


Figure 4.3: From top to bottom, taken from Nicolas LaFlorence’s paper [24], are the distributions of a thermal cloud, a sliding-phase superfluid, and a full 3D superfluid in a disordered system. In the sliding phase cuts along p_{\perp} displaced along p_{\parallel} have very similar distributions.

the span $(p_{\parallel, \min}, -p_{\parallel, TF}), (p_{\parallel, TF}, p_{\parallel, \max})$. We use that fit to estimate the thermal contribution in the span $(-p_{\parallel, TF}, p_{\parallel, TF})$, and then re-fit the TF distribution to the residual to determine the in-plane coherent fraction and produce an estimate of μ .

To accurately track the dynamics of $\bar{\phi}(x_{\perp})$ we remove the ballistic fraction from

our distribution along p_{\perp} . We subdivide our ROI along p_{\parallel} in to three sections, $a = (p_{\parallel,min}, -p_{\parallel,TF})$, $b = (-p_{\parallel,TF}, p_{\parallel,TF})$, $c = (p_{\parallel,TF}, p_{\parallel,max})$. The two outer sections only contain ballistic contributions from the cloud, and so we extract the form of the separable thermal distribution $n_{ac}(p_{\perp}) = \sum_{p_{\parallel}}^a n(p_{\parallel}, p_{\perp}) + \sum_{p_{\parallel}}^c n(p_{\parallel}, p_{\perp})$. We remove this from the distribution $n_b(p_{\perp}) = \sum_{p_{\parallel}}^b n(p_{\parallel}, p_{\perp})$ to derive the perpendicular distribution of the coherent fraction,

$$n_{b,c}(p_{\perp}) = n_b(p_{\perp}) - n_{ac}(p_{\perp}) \left(\frac{\sum_{p_{\parallel}}^b}{(\sum_{p_{\parallel}}^a + \sum_{p_{\parallel}}^c)} \right) n_T(p_{\parallel}) \quad (4.2)$$

In a system with no correlations along the c-axis (p_{\perp}) the distribution of the coherent fraction will look thermal. In a clean sufficiently deep lattice containing a cold cloud $n(p_{\parallel})$ would be a Thomas-Fermi distribution, and $n(p_{\perp})$ would be a Gaussian distribution reflecting the compression of the individual pancakes, and it is both what we expect and what we see in the sliding phase in our system at sufficiently high temperatures. As we

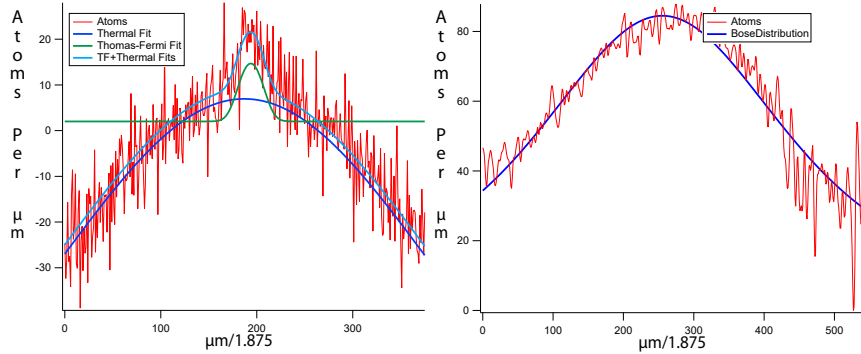


Figure 4.4: Left to right, $n(p_{\parallel})$ and $n(p_{\perp})$ in a cloud just below the BKT transition. A tiny Thomas-Fermi distribution shows up in-plane while there's no evidence of any coherence along p_{\perp} . The units, Atoms per μm , .

cool the cloud correlations begin to develop along p_{\perp} . While the density profile does not change much, the ensemble average of the power spectral density of phase fluctuations in our system, $\rho(\mu, T, V, p)$ narrows in p according to $e^{-\frac{E(p,\mu,V)}{k_B T}}$. Because our system size is not large enough for our excitation spectrum to be gapless the density of states $\nu(E)$ is not gapless, and so the narrowing distribution as a function of momentum is not smooth. At the lowest temperatures and lattice depths we see a few macroscopically occupied states

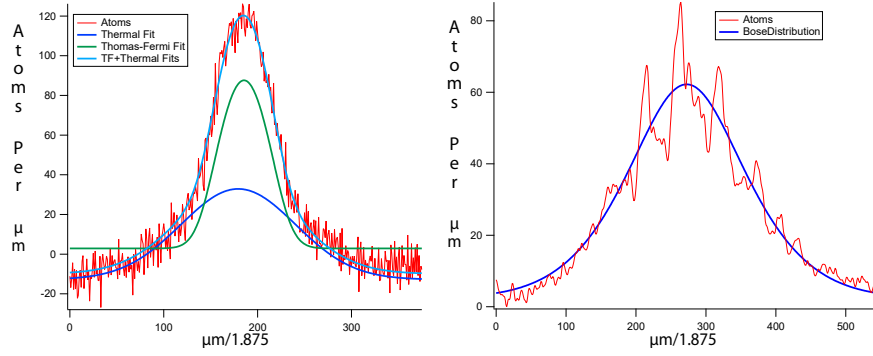


Figure 4.5: Left to right, $n(p_{\parallel})$ and $n(p_{\perp})$ in a cloud well below the BKT transition and establishing coherence along the lattice.

in TOF in a very narrow profile. If the distributions were roughly isotropic as in Fig. 4.3's ensemble averages they would unambiguously be 3D superfluids, but they are feature-full. We have no theoretical predictions to compare individual cloud profiles against, but the phase fluctuations that result from a small phase stiffness expected in a disordered 3D superfluid would express themselves as wide distributions when projected into TOF.

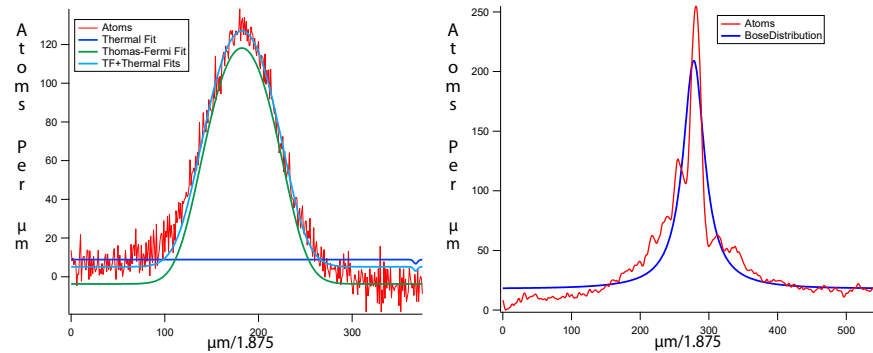


Figure 4.6: Left to right, $n(p_{\parallel})$ and $n(p_{\perp})$ of a likely 3D disordered superfluid. The distribution is narrow but still has significant phase fluctuations along the lattice, which are represented here.

4.2 Phase Fluctuations, Induced vs Many-Body

Our identically prepared clouds are much different from one another. Allowing for equilibration on a seconds long time scale does not diminish these effects. When one manufactures a BEC big changes in the shape of a cloud strongly suggest instability in the shape, position, or depth of a trap. We've well characterized the behavior of our optical

potentials, and I estimate such contributions to be nonexistent. Our optical dipole cross trap does change position as a function of its depth along the lattice axis by about 12 μm . The final evaporation step that sweeps us over this range is two seconds long. The ^{87}Rb deBroglie wavelength at a velocity of 6 $\mu\text{m/s}$ is 764 μm . The kinetic energy in freespace would be $3.9 \cdot 10^{-3}$ Hz. The excitations that could be imparted by phase noise in our lattice, properly calculated, are done over the full noise spectrum with knowledge of the full many-body excitation spectrum available, but with a full range of .04 radians and a statistical width closer to .02 over the full bandwidth we can estimate that, for our longest wavelength lattice, the movement is over a distance of about 30 nm. Putting all those noise into our 2 kHz peak give us a kinetic energy at max velocity of .446 Hz, which is on the same scale of deBroglie wavelength excitations at the size of our cloud. The length scales differences of the drive field of 5 μm , the size of the excitation 75 μm , and the scale difference of the drive energy and the excitation energies of 10^4 , we can estimate that any coupling will be very weak. This would be the highest energy drive and closest-to-resonance case. Lower energy excitations cannot exist on the length scale of our system. We conclude what we see is the result of the intended many-body Hamiltonian.

4.3 Dispersion in TOF

A noninteracting gas suddenly released from a trap $\hat{H}(t = [-\infty, 0]) = \hat{p}^2/2m + \hat{V}(x, p)$ in a TOF measurement will be suddenly projected into momentum-space $\hat{H}(t = [0, TOF]) = \hat{p}^2/2m$, which constitutes a Fourier transform of the in-situ wave function. In a long enough TOF the distribution $n(x) \rightarrow n(p)$. An interacting gas in the mean field limit in TOF will experience coherent nonlinear distortions under the GP equation $\hat{H}(t = [0, TOF]) = \hat{p}^2/2m + g \sum_{p_i+p_j=p_k+p_l} |\hat{\psi}_i\rangle |\hat{\psi}_j\rangle \langle \hat{\psi}_k| \langle \hat{\psi}_l|$ whose nonlinear term disperses the wavefunction. In the case of a BEC in a harmonic trap this leads to a self-similar Castin-Dum expansion of the Thomas-Fermi distribution. Our in-plane momentum distribution is dominated by these dynamics, but in our system the out-of-plane trapping energy

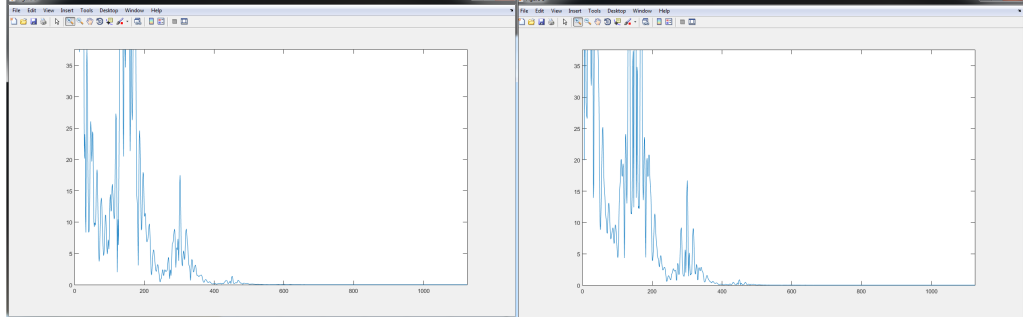


Figure 4.7: These are GPLab TOF simulations projected on momentum-space of our disordered cloud for the first 8ms of TOF in the presence of phase fluctuations. At left is post-TOF, to the right is pre-TOF. Dispersion makes peaks smaller and valleys shallower in our clouds, but the envelope remains roughly constant.

is larger than the chemical potential. The quick expansion of each individual pancake spreads the phase-fluctuation information contained in the cloud and freezes in the overall envelope. We confirm this with a set of GP simulations where phase-fluctuations have been added in Fig. 4.7. We take these simulations as evidence our individual pictures well represent a smoothed-out occupation $n(p_{\perp})$ and the phase fluctuation power spectrum of the disordered cloud.

4.4 Phase Fluctuation Power Spectrum

In an individual cloud we expect the probability of occupation for a given phonon mode to follow the grand canonical ensemble, we approximate $n(p_{\perp}) = \nu(E)e^{-\frac{E(p,\mu,V)}{k_B T}}$. We take a natural log of $n_{b,C}(p_{\perp})$. We identify $p = 0$ and create an object $n(|p_{\perp}|) = n(p_{\perp}) + \text{sum}(-p_{\perp})$ and fit a line. We take the slope of the line to characterize the phase fluctuation power spectrum, which we call our coherence parameter. The information derives from $p \gg 0$, so it is not a measurement of phase stiffness, which looks at $\frac{dE}{dp} |_{p \rightarrow 0}$.

4.5 Our Data Set

Our lattice depth lock points varied from 1 to 5 Volts on our pickoff photodiode, which characterizes how much power we send to the AOMs, but which we correlate

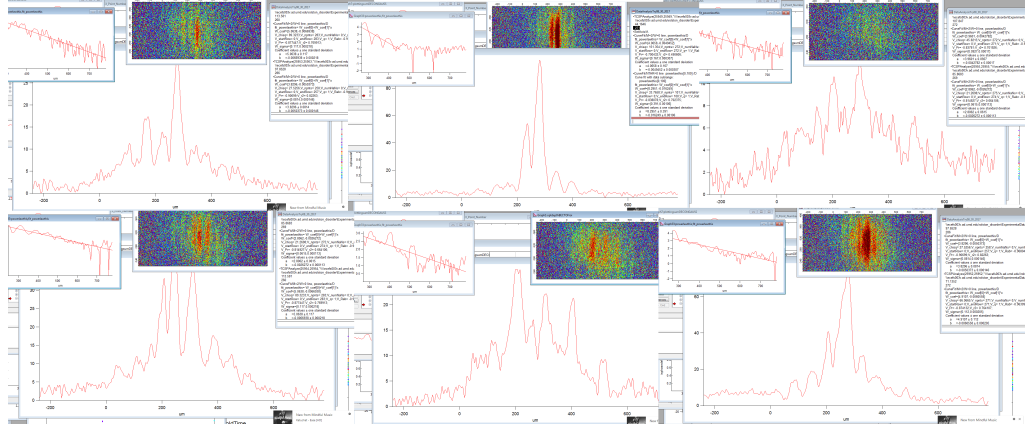


Figure 4.8: Clouds at varying lattice depths and temperatures, the object $\ln(n(|p_{\perp}|))$ and its fit, along with $n(p_{\perp})$

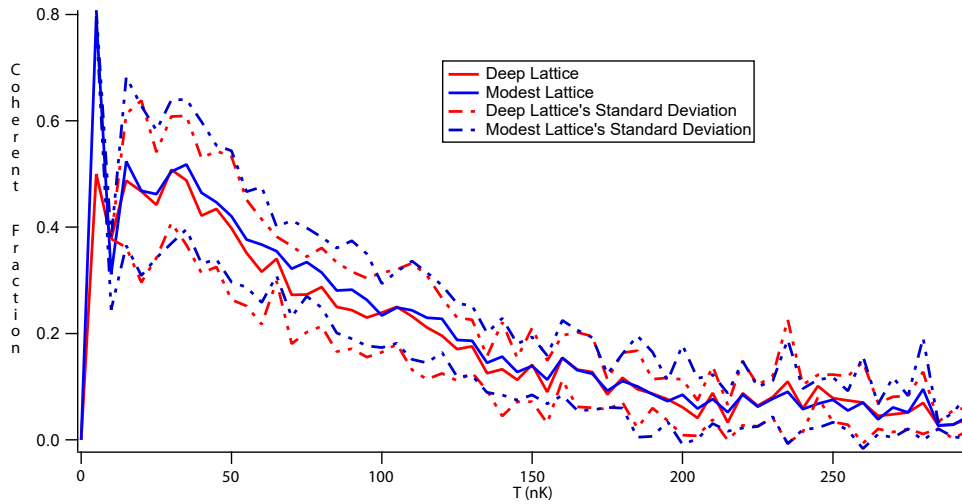


Figure 4.9: The result of our Thomas-Fermi profile fits to the in-plane momentum distribution for our 2 and 4 E_R lattices. They identify a minimum in-plane coherent fraction of approximately .05 even for purely thermal clouds. $T_{c,2D} = 200$ nK

directly with only one of our shallow angle lattices. We characterized our lattice depth by the depth of our $1.3 \mu\text{m}$ period lattice in standing wave pulses. The lattice depth of this band-manifold defining lattice was 1.11 kHz/V , which is about $.82 E_R/V$. We performed two different scans. In every shot we evaporate from a thermal distribution to our final temperature in the presence of our phase-locked lattice. We then utilize the depolarization caused by spontaneous emission in our optical lattice to take an in-situ picture of our cloud. The probe beam is not uniform, and so the imaging process disturbs the atoms left in the trap, forming a type of quench. Our first scan observed our cloud at low temperatures and

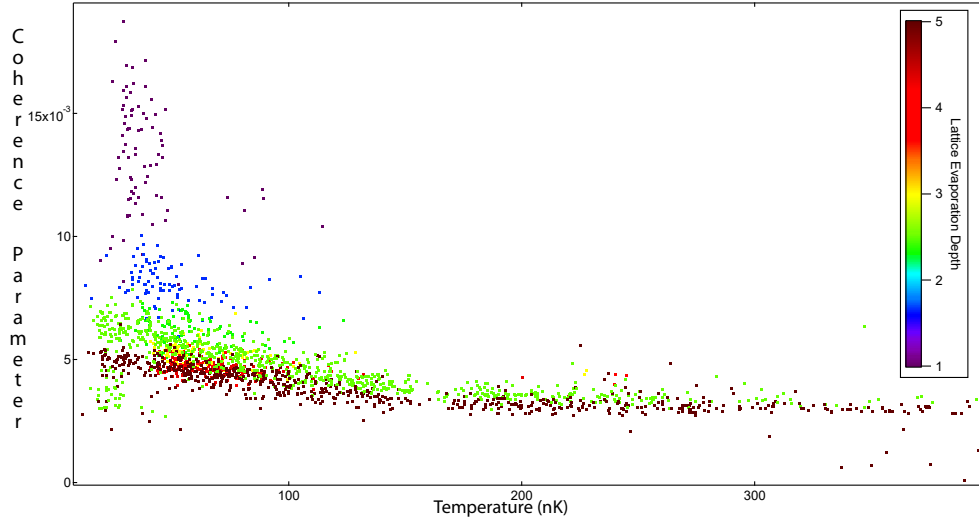


Figure 4.10: We evaluate the coherence of the cloud along p_{\perp} over a range of temperatures and lattice depths. Phase coherence decreases with both lattice depth and temperature, as expected.

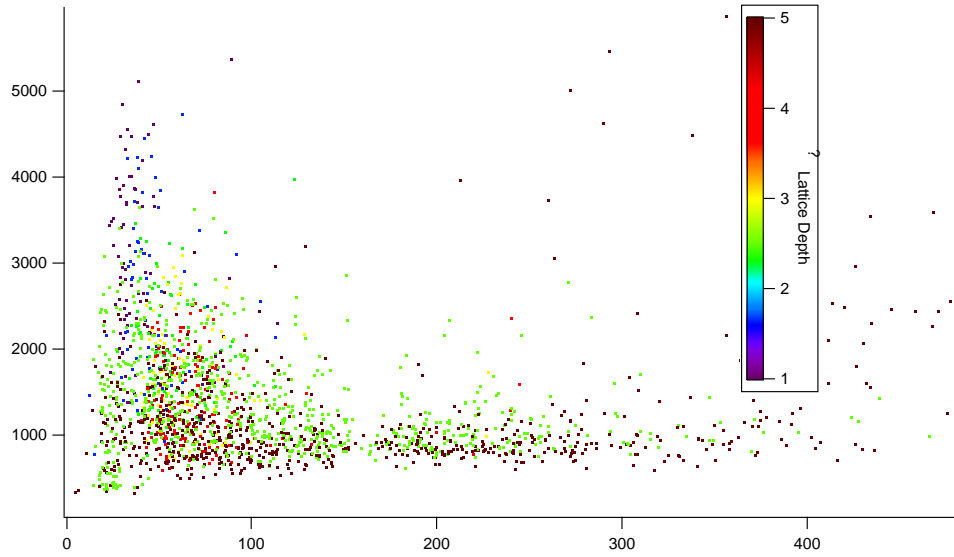


Figure 4.11: We evaluate the shot noise in the system by evaluating deviations from Bose fits to our time-of-flight distribution. We see growth begin in our deep lattice near 100 nK and in our more modest lattice near 175 nK

over a variety of hold times and lattice depths. The hold times start at 200 ms and range out to 7s. For our second scan we chose two lattice depths, 2 and 4 E_R , to obtain a detailed phase diagram as a function of temperature. In addition we performed each of the two sets of scans with two different optical potentials with two choices of $\phi_{\vec{k}}$

The in-plane coherent fraction emerges near 200 nK for both of our temperature-

scanned lattice depths. This is unsurprising. Our band gap varies by less than 7% between the two lattices and the average number in the deepest lattice is reduced slightly by enhanced photon scattering. The two curves are nearly identical. The coherence parameter begins to grow at 175 nK in the well-connected lattice and at 150 nK for the deep lattice. At low temperature the parameter saturates. The low temperature cuts show shallower lattices have a larger range and a higher saturation value as the cloud approaches BEC. The near lack of variation of the parameter as a function of temperature between the 2 and 4 E_R lattices is surprising, as inter-lattice hopping is suppressed exponentially in lattice depth. The changing saturation values of this coherence parameter as function of lattice depth roughly follows this expected behavior, and follows the expected behavior p_{\perp} of the system described in the body of theoretical work on the subject. It may only be useful at low temperatures.

In the next section we'll discuss the average, ensemble distributions constructed in 25 nK temperature bins for our two temperature-scan lattices, where we point out that they resemble the curves of Bose distributions. The results of the fits are nonsensical; they return higher temperatures for 25 nK clouds than they do for 200 nK clouds, and there's no reason to expect a 1D Bose distribution for the system. But because Bose distributions well duplicate the statistical average, and because the bins in that section may be over-broad, we fit to the clouds individually and sum up the deviations of the clouds from those fits to characterize the shot noise of our systems. We see our shot noise begin to grow at 175 nK in our 2 E_R lattice and at 100 nK in our 4 E_R lattice. This stands in contrast to my phonon occupation coherence measurement shown in Fig. 4.8 where the momentum distribution begins to shrink quickly in both systems near 175 nK. The magnitude of the shot noise is evidence of the emergence of a quasi-coherent Giffiths phase according to Pekker et. al., and with a lower onset temperature for the deeper lattice it matches the trends predicted in the theory.

4.6 Momentum-Space Bunching

Because our clouds are so different from one another we chose to study the statistics of those differences. One can identically prepare a set of clouds and let them evolve in TOF to generate $\psi^\dagger\psi(p)$. The average of these distributions can produce an ensemble average,

$$\frac{1}{m} \sum_m \psi^\dagger\psi(p)_m = \psi^\dagger\psi(p)_{avg} = n(p) \quad (4.3)$$

and consider each individual distribution's deviation from the average.

$$\psi^\dagger\psi(p)_m - \psi^\dagger\psi(p)_{ave} = \delta n(p)_m \quad (4.4)$$

The object $\sum_m \langle \delta n(p_i)_m \delta n(p_j)_m \rangle$ is the set of available 2 body correlation functions of deviations from mean distributions in momentum-space. They've been shown useful in discriminating between phases in 1D Bose gases by Feng et. al. [45]. Qualitative differences in the shapes of these correlation functions emerge for different phases of matter. Compared against quantum monte carlo simulations they can accurately identify those phases. We found the most interesting axes of symmetry in Fig. 4.12 data were the diagonal axes, the lower-left to upper-right axis being a correlation function, and the upper-left to lower-right being a convolution function. The number and locations of maxima and minima vary in their system in different phases matter. We have no simulations to compare our data against, but we are better able to resolve our momenta. We measured how these fluctuation correlation functions vary in our data as a function of temperature in 25 nK bins over the range of temperatures including purely thermal gasses down to a gas with a nonzero BEC fraction, from 250 nK down to what we label for convenience 0 nK, and more accurately identify as $T \ll \mu < 50nK$, where our temperatures are so low our fits fail. We chose two lattice depths for this measurement, 2.77 and 5.55 kHz.

There are several things to pay attention to in Fig. 4.13. The underlying lattice is

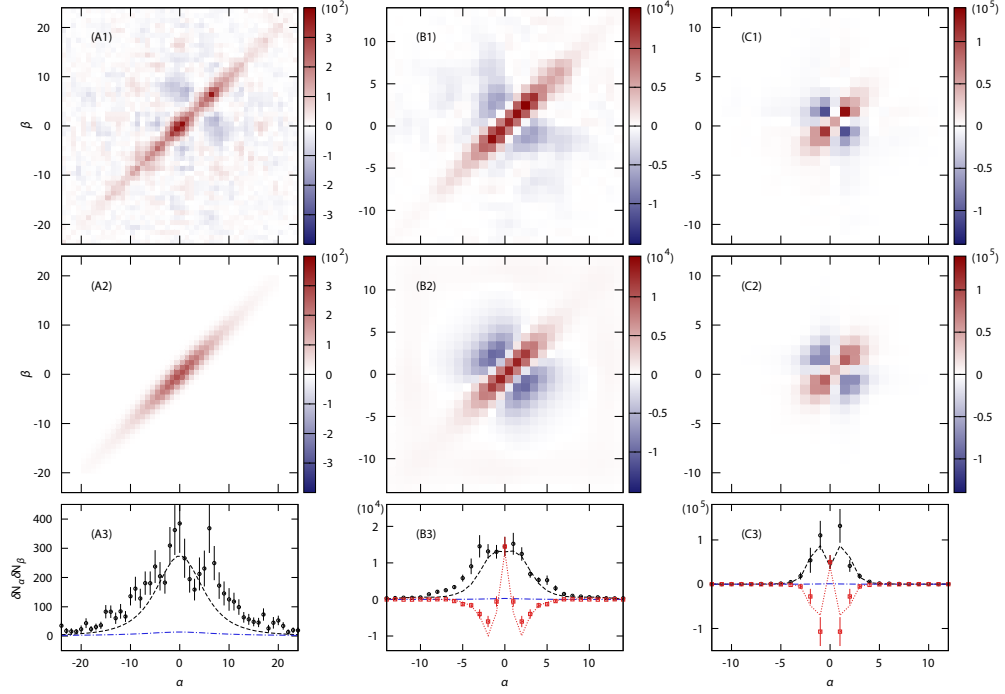


Figure 4.12: This description is lifted wholly from Feng et. al. [45]: Momentum correlations $\langle \delta n_\alpha \delta n_\beta \rangle$ for a gas in the IBG regime (Data A, left column), in the qBEC regime (Data C, right column), and in the qBEC-IBG crossover (Data B, middle column). The pixel size is $\Delta/\hbar = 0.15\mu\text{m}^{-1}$. The experimental data are shown in the top row. Data A, B and C are compared with the IBG theory, QMC calculations, and qBEC theory respectively, at the temperature of the data determined by independent thermometry methods [26]. The middle row gives the computed momentum correlations. The bottom row shows the diagonal cuts: the experimental data in circles for $\alpha = \beta$ (squares for $\alpha = \beta$ for Data B and C only) are compared with their respective theory model in dashed (dotted) lines. The error bars are statistical. The dash-dotted lines give the shot-noise limit.

visible in the ensemble average. One can see the $2\hbar\vec{k}$ peaks from the 1.3 and $1.5\mu\text{m}$ lattice at the edges of the image. The momentum-space range of the data was selected to encompass the lower band manifold set by the band gap of the $1.3\mu\text{m}$ lattice. They are apparent throughout our temperature range. The ensemble averages also resemble Bose distributions. In one dimension the density of states $d(p) = 2$, so the distribution is just $\frac{A}{e^{(\epsilon-\mu)/k_B T} - 1}$, where A is a normalization constant, and ϵ is the energy of the free particle eigenstate, in this case $p^2/2m$. The distribution diverges as $\mu \rightarrow 0$, and our distributions resemble a Bose gas approaching condensation at high temperature. Several parameters returned by the fit lack any correlation to reality. Lower temperature clouds are identified as higher temperature, and the fact that colder clouds do have several momentum states

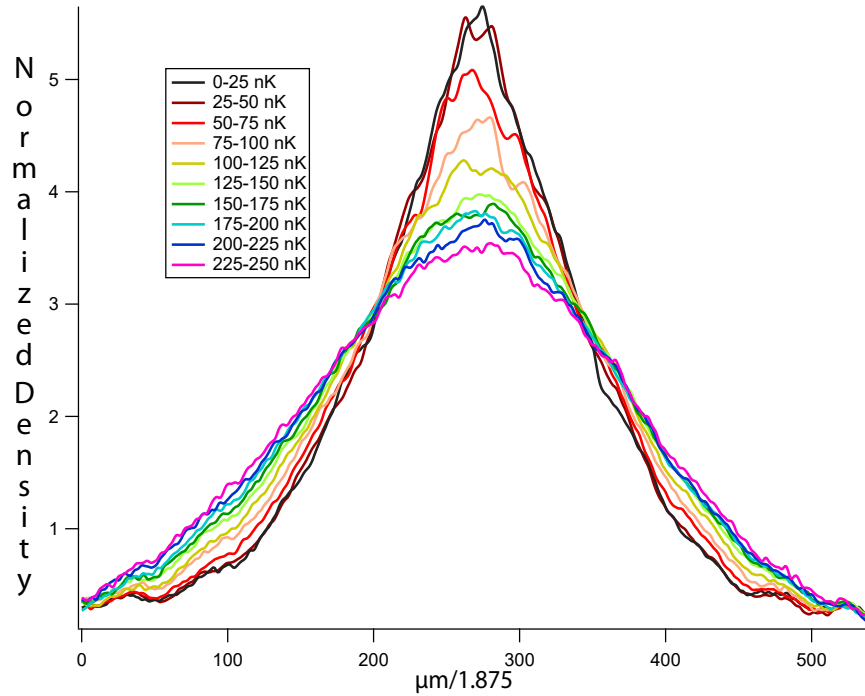


Figure 4.13: The ensemble average of every temperature bin in our well-connected disordered system. Between 200 nK, the onset of 2D superfluidity, and 125 nK the distribution looks mostly thermal, with a signature of our $1.3 \mu\text{m}$ lattice at $\pm 2\hbar k$. Below 125 nK the center of the distribution rises quickly, indicating a crossover towards phase coherence along the direction of the disorder.

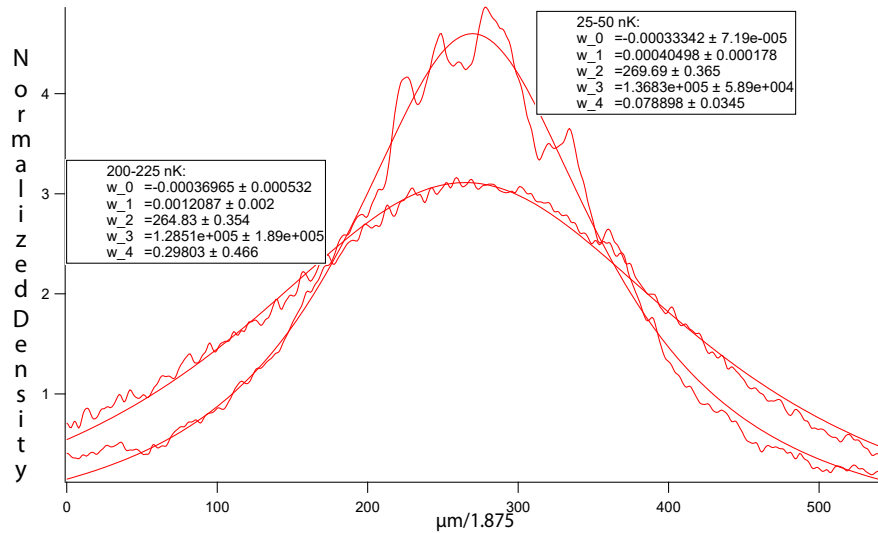


Figure 4.14: Bose fits identify the colder cloud as closer to condensation, with the chemical potential term $w_4 = \mu/T$ approaching zero, but it also identifies the 25-50 nK bin as being hotter than the 200-250 nK bin ($w_3 = T$ in arbitrary units)

with nonzero chemical potentials means the distribution shouldn't apply. But it does have worth some worth. The undistorted momentum distribution of our cloud represents

the power spectral density of fluctuations in-situ, and so its Fourier transform should be $\int \psi(x)\psi(x+a)dx$, the $g(1)$ of the order parameter. The proximity of μ/T to zero shows a deviation from the Gaussian distribution of a purely thermal gas. So while we may not be able to identify any particular renormalization group's characteristic $g(1)$ or exponents in our system, the parameter μ in the Bose fits of the average distribution does indicate how far the ensemble average deviates from a purely thermal distribution. This deviation begins when the central feature in the distribution starts growing quickly near 125 nK, and is evidence of strong p_{\perp} correlations. $\frac{d}{dT}\psi^*\psi(p=0)$ is obvious in profile.

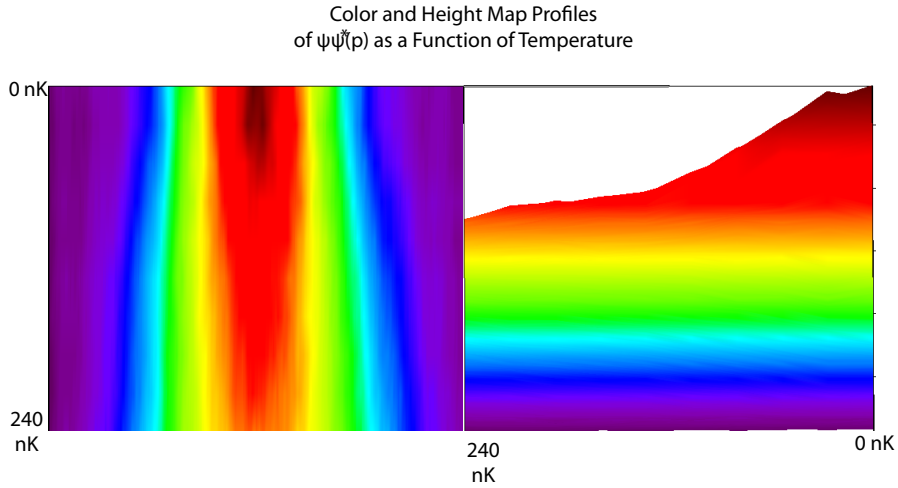


Figure 4.15: These are profiles of a 3D rendered and colorscaled average distributions of our clouds as a function of temperature. The sudden jump in the growth of $p=0$ stands out at 125 nK. The growth saturates at 50 nK

The average of the autocorrelation of deviations from the average distribution $AC(q,T) = \sum_m \int \delta n(p)_m \delta n(p+q)_m dp$ provides more evidence of a crossover from a thermal to a quantum degenerate regime in p_{\perp} after 2D superfluidity. At low temperatures fluctuations gain both correlation and anticorrelation length scales. The first anticorrelation dip occurs at a momentum offset with a ^{87}Rb deBroglie wavelength of $2.6 \mu\text{m}$, while the offset in the positive correlation peaks are one recoil momentum of our manifold defining wavevector. The crossover from thermal fluctuations to correlated fluctuations begins at 175 nK and is complete once we get to 100 nK, but is still obvious in the region

of 100-125 nK. I thus identify three crossovers. 2D superfluidity's onset occurs at 200

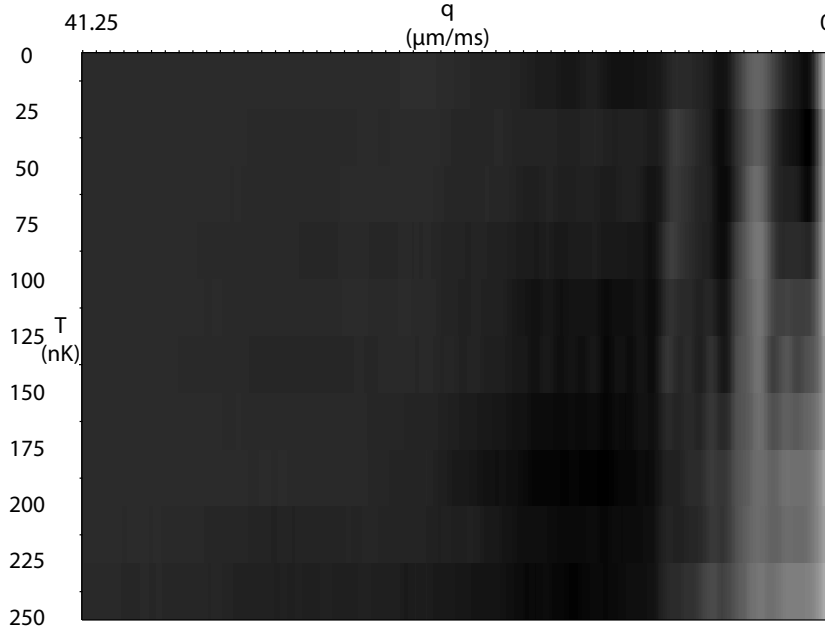


Figure 4.16: Displayed here is $AC(q, T) = \sum_m \int \delta n(p)_m \delta n(p + q)_m dp$ The staggered BKT transition begins near 200 nK. At higher temperatures there are some signatures of the lattice, a consequence of the band gap being on the order of the temperature. As temperature decreases we resolve three prominent peaks, the outermost of which creeps in closer to the $q=0$ peak as temperature decreases. The thermal inter-peak occupation is gone below 100 nK.

nK. Between 175 nK and 100 nK the gas becomes more correlated along p_{\perp} . And between 125 nK and 50 nK we have condensation. If we identify 200 nK, 175 nK, and 125 nK as critical temperatures, we have as many phases as predicted through RNG theory and at approximately the right temperatures.

The convolutions $Conv(q, T) = \sum_m \int \delta n(p)_m \delta n(-p + q)_m dp$ offer different microscopic information but identify similar crossover regions. In a convolution there's no reason to expect the $q = 0$ term to be one. The fluctuation distributions would need to be symmetric about $p = 0$. So the peak amplitude in these convolutions offers data about how symmetric the distributions are. In p_{\perp} 's thermal regime the symmetry of the fluctuations climbs with temperature near 150 nK. The trend at all other temperatures is a steady decrease in the amplitude of the convolution. At low temperatures the convolutions are packed with features separated at length scales that don't map easily onto any of the

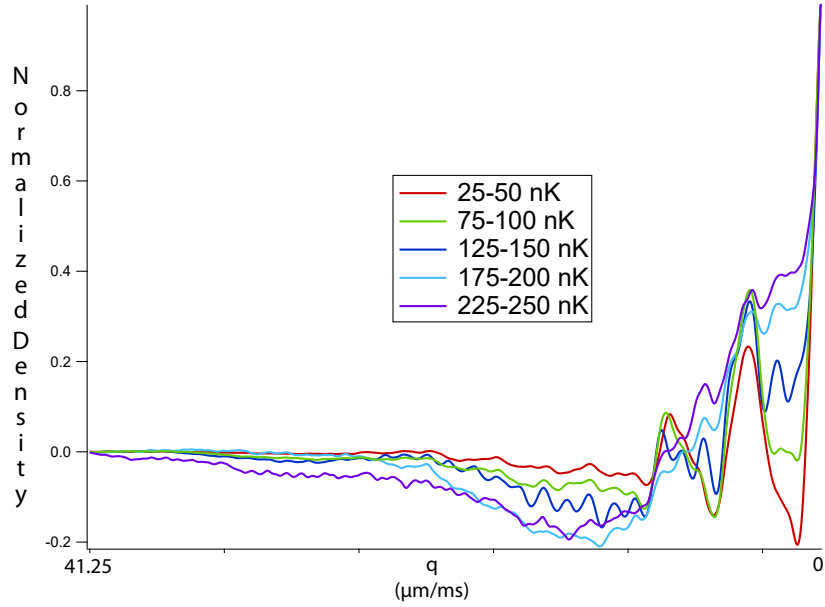


Figure 4.17: We show $AC(q, T) = \sum_m \int \delta n(p)_m \delta n(p + q)_m dp$ at selected temperatures to highlight differences. Clearer here is the bunching behavior at low temperatures. The outer peak gaining density correlates with a decrease in the density in the region before the middle peak below 100 nK, where the correlation function actually becomes negative. This is true below 50 nK for the second intermediate region.

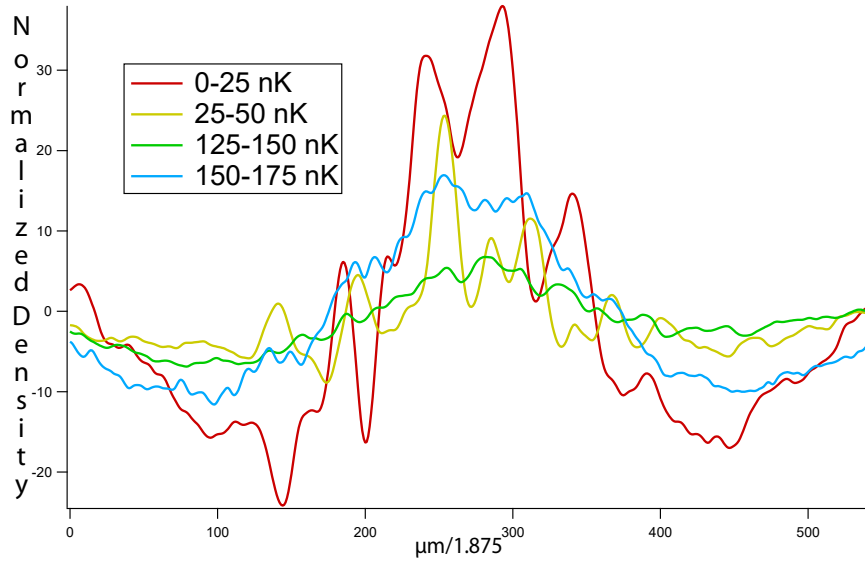


Figure 4.18: We show $Conv(q, T) = \sum_m \int \delta n(p)_m \delta n(-p + q)_m dp$ at selected temperatures to highlight differences. At low temperatures the convolutions are feature-full and show correlations at no obvious lengthscale. At higher temperatures in the sliding regime convolutions are purely thermal.

length or momentum scales of our system. At high temperatures they're Gaussian, which one expects in the presence of thermal correlations. When the data sets are separated into sub-bins the shapes of these distributions do not change much, which suggests the

correlations are real, but we need simulations to say more.

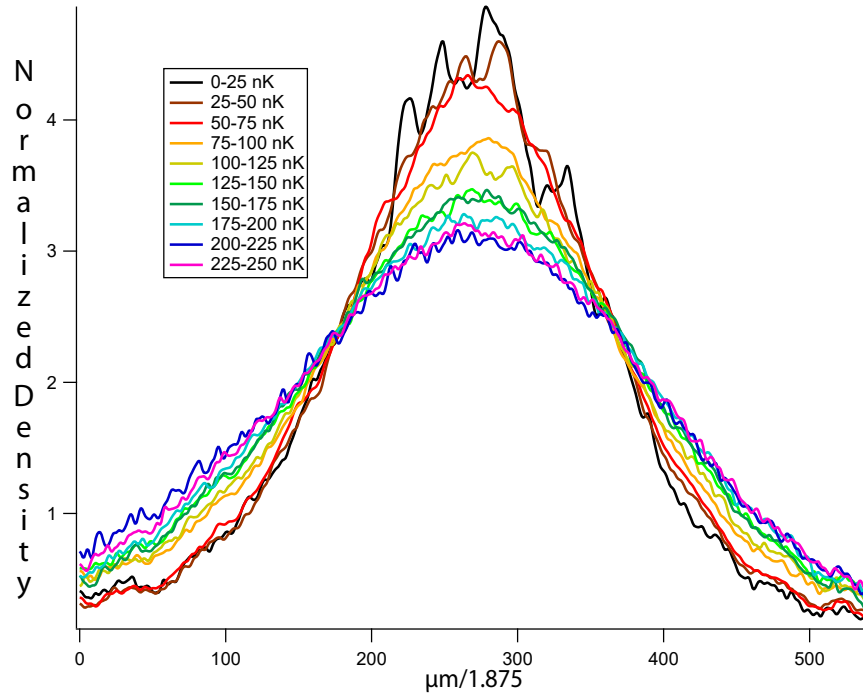


Figure 4.19: The ensemble average of every temperature bin in our deep disordered system.

At $4 E_R$ we see qualitative differences at lower temperatures. Tunneling is suppressed by a factor of $1/e$ compared to the $2 E_R$ lattice, so p_{\perp} transitions should occur at lower temperatures. The 125 nK point should map to 50 nK, and the 150-175 nK region should map to 75 nK. The momentum distributions are wider due to a flatter band structure. The distributions are also more feature-full at low temperatures and momentum. But we only identify three regimes, and the crossover to a correlated system is sharp at 75 nK, both in the growth of the $p=0$ population and in the fluctuation autocorrelation. The convolutions show a growth in fluctuation correlations below 75 nK by a factor of two, reinforcing the 75 nK transition point. The growth in the convolution peaks between the 50-75 nK bin and the 25-50 nK bin may suggest a phase crossover around 50 nK, but while the size of the correlations changes quite a bit between the two bins, its fundamental character does not.

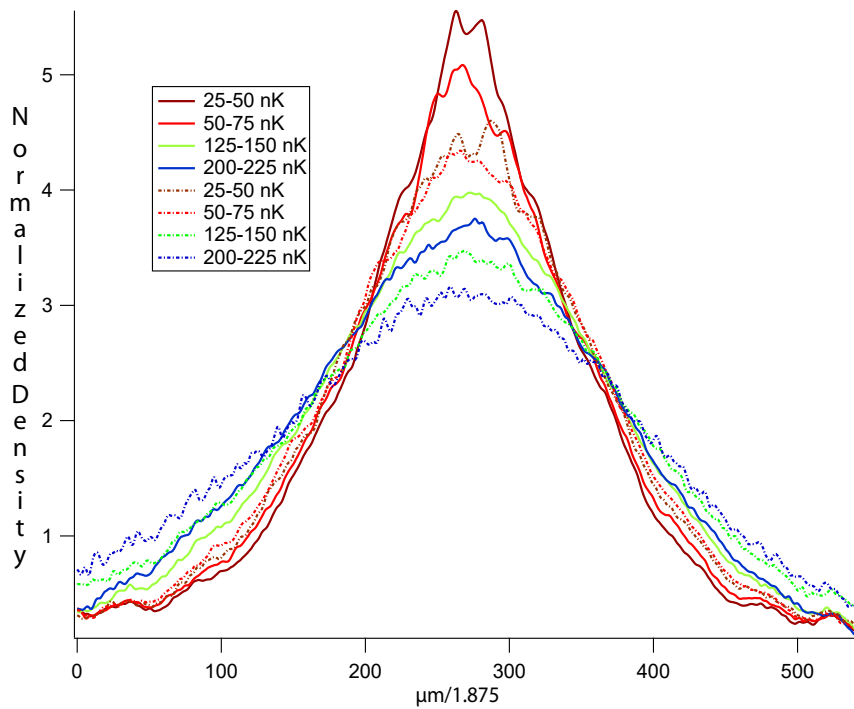


Figure 4.20: At the same temperature the deeper lattice (dashed lines) has a depleted $\psi^*\psi(p=0)$ and a wider distribution.

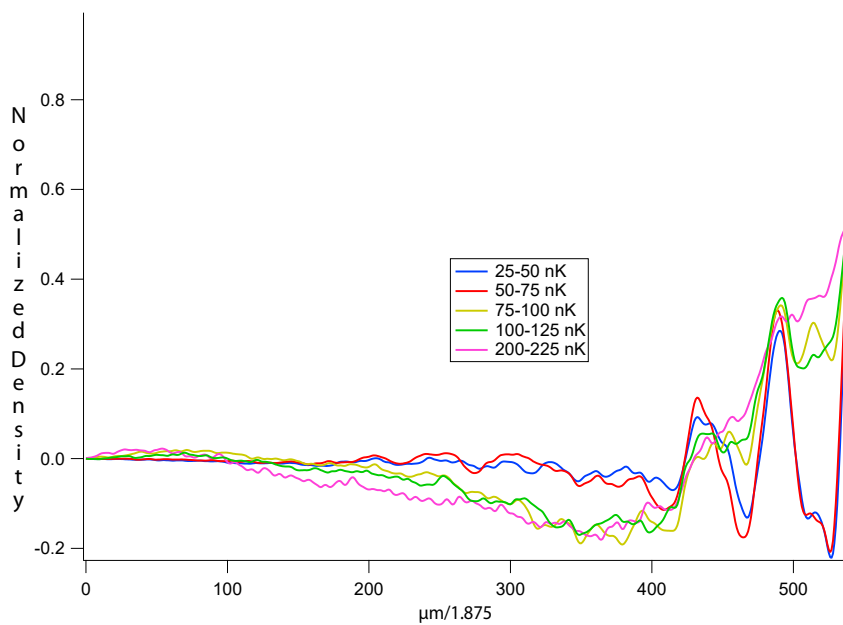


Figure 4.21: There are some sub-thermal correlations below $T_{c,2D}$, but no significant differences between 200 nK and 75 nK, at which point there's a sharp transition. In addition there's a clear length scale at low temperatures matching the autocorrelation data.

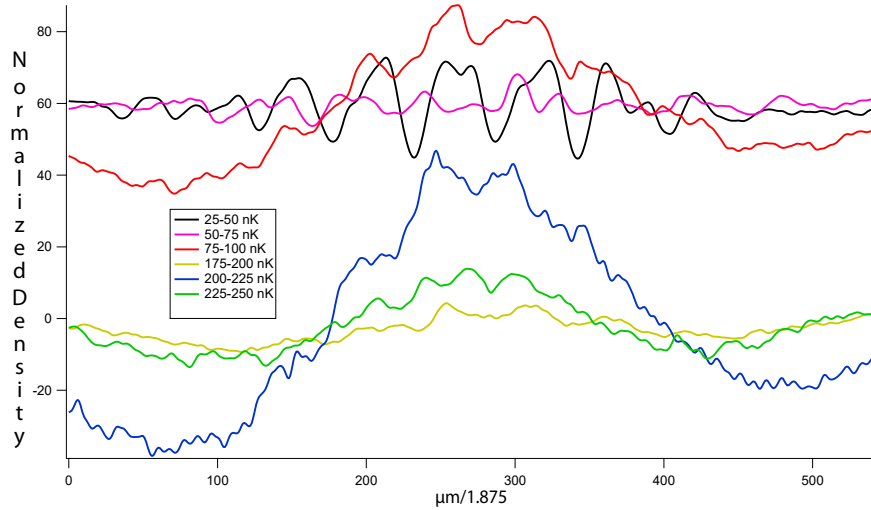


Figure 4.22: The growth in correlations between 75 and 25 nK gives us a probe of a temperature regime that otherwise looks static. The correlation and anticorrelation revivals persist out to high momenta. The three lower temperatures are offset to $6 \cdot 10^{-5}$

4.7 Our Phase Diagram

Using standard Thomas-Fermi fits we have identified a transition to 2D superfluidity as consanguinous with the emergence of in-plane BEC fractions through our Thomas-Fermi fits at 200 nK. We've identified a second likely critical point at two different temperatures in two different lattice depths where correlations begin to grow between pancakes. We identify these points through the emergence of interferometric effects in TOF images in individual atom clouds' deviations from a Bose fit. In the $2 E_R$ lattice this occurs at 150 nK, and in the $4 E_R$ lattice this occurs at 100 nK.

Our fluctuation correlation measurements, which are significantly clearer than our scatter-shot deviation-from-a-Bose-fit measurements, indicate a slow crossover in the $2 E_R$ lattice in the 150 to 75 nK range. A BEC-like peak in the $2 E_R$ ensemble average shows growth starting at 100 nK, which hints at a growing 3D superfluid coexisting with a quasi-coherent Griffiths phase, likely starting in the densest region of the cloud, between 100 and 75 nK.

In the $4 E_R$ lattice, both the growth of the BEC-like fraction and a sharp cross-over in

the fluctuation autocorrelation occur simultaneously, at 75 nK. All the qualitative changes that occur below the BKT transition thus occur somewhere between 100 nK and 75 nK. This suggests a very brief, if at all present, quasi-ordered Griffiths phase in the deeper lattice between 75 and 100 nK, and an ordered full 3D phase below 75 nK.

The convolution data is odd, and doesn't correspond to our other measures. The $2 E_R$ and $4 E_R$ lattice show a change in the fluctuation convolution starting at 50 nK, and growth of this ordering at lower temperatures. It may only indicate the growing global coherence in the 3D superfluid regime, but without a direct measure of a p_\perp superfluid critical velocity we are unable to truly identify which phase we see at our lowest temperatures.

4.8 Future Directions

The HiBAL's current capabilities are mostly limited by RF engineering. Driven systems in a disordered environment may open a path to exploring higher dimensional spaces. Our spin polarization control opens the door to spin mixtures in disordered systems, and our instantly and broadly tunable range of lattice \vec{k} and velocities allows broad momentum-state addressability. We do not know all the available applications of our control scheme. Our experiment is designed to be capable of creating two reservoirs on either side of our disordered potential, where an imbalance in the atom number in either reservoir can be treated as a voltage difference. We could also switch between several different potentials faster than a microsecond, which allows us to precisely populate every other pancake, or to perform an ensemble pairwise interferometric measurement. Band mobility and superfluid critical velocity measurements would be more direct measures of the bulk 3D properties of our disordered system, and would likely unambiguously identify the phase of our clouds at their lowest temperatures. Theory work to produce $\langle \delta n_\alpha \delta n_\beta \rangle$ along p_\perp may shed light on measurements we've already made, and we encourage interested parties to pursue those simulations.

Chapter 5: A Mobioid Proposal

The BKT crossover and the physics of vortices in quasi-2D systems can be altered with boundary conditions. Vortices can be trapped at the center of ring systems, and the result is macroscopic superflow. Quantum quenches in such systems produce net angular momentum through the Kibble-Zurek mechanism as a spontaneously broken $U(1)$ symmetry. These mechanisms are underpinned by vortices, and the BKT phase transition is a topological phase transition because a vortex is a topological object. Its angular momentum makes it an orientable object, and its antiparticle is a vortex of opposite rotation.

There are a limited set of closed systems with a smooth translation symmetry in two dimensions, and they are distinguished by their topology, how they connect to themselves. A globe is one such object. The hairy balls theorem states if a globe is going to have one phase defect, it is going to have two, and they will have opposite rotation/charge. The curvature of the surface can exert a torque on the defects' angular momentum, but that angular momentum is always well defined as a function of position, and so whenever a vortex antivortex pair meet, they annihilate. But there do exist more twisted spaces, such as the Klein Bottle or Mobius strip, which lack orientability. A vortex with curl q at its core will circle a strip once and return to its original spot with charge $-q$. It is possible to create a 2D Bose superfluid in at least one of these: the Mobius strip, and play with topological order in a topologically nontrivial space.

5.1 An Optical Potential for Mobius Strips of Cold Atoms

It is possible to build a Mobius strip out of a degenerate Bose gas without engaging in a complicated and Sisyphean alignment scheme. One only needs two laser beams: one blue detuned elliptical Gaussian, and one red detuned trapping beam shaped with a mask. Fig 5.1 depicts the geometry of the trap in three dimensions. Along the \hat{z} direction one can relay image an optical beam in the shape of the outline of a tadpole, symmetric about the \hat{y} axis. The imaging system's resolution determines the waist of the beam perpendicular to its curved surface, and optical resolutions of five micrometers are easy to achieve even on experimental apparatuses with thick windows and long working distances. Quasi-2D trapping potentials with out of plane harmonic confinement are possible in such a regime with some hundreds of milliwatts of light within several nanometers of the cycling transition in ^{87}Rb . A trap depth of 10 kHz would produce out of plane harmonic confinement of 2.7 kHz and trap a cloud with temperatures on the order of a kiloHertz. With a Rayleigh range of 100 micrometers that would create a tadpole shaped quasi-2D degenerate Bose gas with a width along the beam of about 20 μm . In this regime the BKT transition can be crossed by varying the density of the cloud by varying the number. A second simple elliptical Gaussian beam propagating down at a 60 degree angle through the $\hat{x}\hat{z}$ plane can push atoms out of the center of the tail and cut off its connection to the cylindrical head at the top on one side and the bottom of the other. This disconnects the tadpole and leaves behind a quasi-2D gas connected as a Mobius strip.

5.2 Non-Orientable Spaces and a Local \hat{L}

A Mobius strip is defined by the strange way in which it connects to itself. It has only one edge, and only one surface. Imagine a traveller who gets lost in a strange place and resolves to find her way out. She stands at the edge of a precipice. She turns left and sees a path that curves away into the unseeable distance. Turning further she sees a far edge

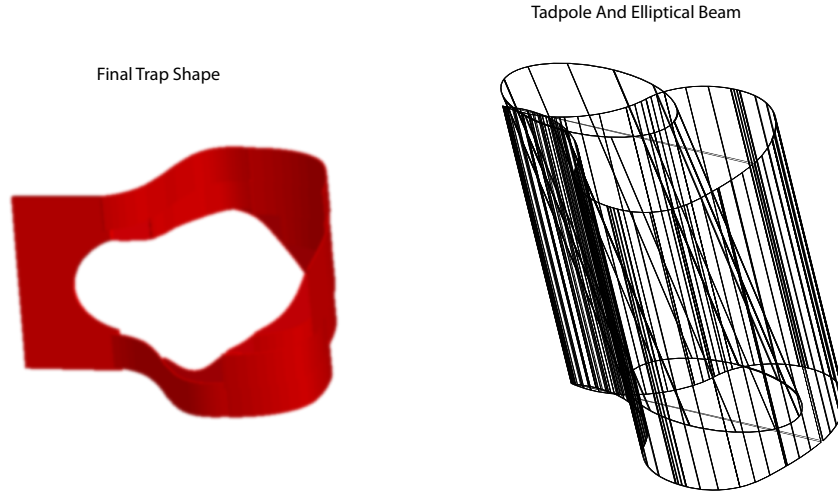


Figure 5.1: This is a demonstration of how an optical trap for a mobius strip could be constructed with two beams and a single bichromatic trap imaging axis.

at distance $2w$ from her position and turns once more to see an identical path going off into the distance. With two choices of direction looking rather similar and two promising certain death she then takes a stroll with the far edge on her right, and leaves some crumbs in this otherwise sterile place so she doesn't get turned around if she goes mad. After a distance L she looks to the far edge on her right and sees the start of a trail of bread-crumbs which goes off along the direction she's already travelling. Perturbed she keeps walking, and after another distance L she happens upon the start of a very familiar trail of crumbs. And then she wakes up, and tries to make sense of the whole thing.

To rigorously track this path one defines a coordinate system constructed from the generators $-i \frac{d}{dx}$ and $-i \frac{d}{dy}$. Choosing to place $y=0$ at the center of the strip and $x=0$ at any position, the symmetries are as follows,

$$\psi(x, y) = \psi(x + L, -y) = \psi(x + 2L, y) \quad (5.1)$$

This states a traveller that goes around the strip once perceives his original position on the opposite side of the strip, and ultimately must travel the length of the strip twice to come back to his original spot. Choosing a distance from the center y and walking once

around the strip lands one at $\psi(x + L, y)$, which is the same physical position as $\psi(x, -y)$. Thus walking around the strip once flips the coordinate system along the y direction, but not the x direction. Consequently the momentum operator $-i\frac{d}{dy}$ flips sign while the momentum operator $-i\frac{d}{dx}$ does not. One can attempt to construct an angular momentum operator $\hat{p}_x + i\hat{p}_y$. Imagine placing a single vortex at $y = 0$, right in the center of the strip. In this coordinate frame we evaluate the angular momentum of the strip and it has some positive value. But then we send the vortex around the strip once, and because this is identical to translating the coordinates around once \hat{p}_y has changed sign, and so the angular momentum of the quantum gas has not been conserved by a translation operator. We have not created something that violates real conservation laws in our Universe. This is rather an effect of the torque the optical potential adiabatically exerts on the system as it passes around the cylindrical part of the potential. While angular momentum of the full three dimensional object is a good quantum number, within the confines of this type of two dimensional closed space angular momentum has been rendered a bad quantum number.

5.3 Vorticies in a Non-Orientable Space

In an attempt to develop exact solutions for what now appear to be dubious quasi-particles we employed a Green's Function method. In two dimensions one can define a flow field $\vec{J}(x, y)$ with divergence $\vec{\nabla} \cdot \vec{J} = 0$ and curl $\vec{\nabla} \times \vec{J} = 2\pi\delta(\vec{x} - \vec{x}_0)$ as $\hat{z} \times \vec{E}$ with $\vec{\nabla} \cdot \vec{E} = 2\pi\delta(\vec{x} - \vec{x}_0)$ and $\vec{\nabla} \times \vec{E} = 0$. Our mobioid boundary conditions require the flow $J_x(x + L, y) = J_x(x, -y)$ and $J_y(x + L, y) = -J_y(x, -y)$ at all points. At the borders of the strip we require $J_y(x, w) = J_y(x, -w) = 0$ if our boundaries are to be stable in time. This defines the mobioid conditions for our dual scalar potential,

$$\frac{d}{dy}\Phi|_{x+L,y} = \frac{d}{dy}\Phi|_{x,-y} \quad (5.2)$$

$$\frac{d}{dx}\Phi|_{x+L,y} = -\frac{d}{dx}\Phi|_{x,-y} \quad (5.3)$$

While the border condition requires

$$\frac{d}{dx}\Phi|_{x,-w} = \frac{d}{dx}\Phi|_{x,w} = 0 \quad (5.4)$$

We define \vec{E} as the gradient of a scalar potential in a fourier representation,

$$\Phi = \sum_{n=1}^{\infty} \sum_{m=1}^{\infty} (A_{n,m}\cos(\frac{n\pi x}{L}) + B_{n,m}\sin(\frac{n\pi x}{L}))(C_{n,m}\sin(\frac{m\pi(y+w)}{2w}) + D_{n,m}\cos(\frac{m\pi(y+w)}{2w})) \quad (5.5)$$

To meet the condition $\vec{\nabla} \times \vec{J} = 2\pi\delta(\vec{x} - \vec{x}_0)$ and match the boundary conditions, we evaluate $\vec{\nabla}^2\Phi = 2\pi\delta(\vec{x} - \vec{x}_0)$ and the intermediate step,

$$\begin{aligned} \vec{\nabla}\Phi_{n,m}(x, y) = & (\hat{x}\frac{n\pi}{L}(-A_{n,m}\sin(\frac{n\pi x}{L}) + B_{n,m}\cos(\frac{n\pi x}{L}))) \\ & (C_{n,m}\sin(\frac{m\pi(y+w)}{2w}) + D_{n,m}\cos(\frac{m\pi(y+w)}{2w})) \\ & + \hat{y}\frac{m\pi}{2w}(A_{n,m}\cos(\frac{n\pi x}{L}) + B_{n,m}\sin(\frac{n\pi x}{L})) \\ & (C_{n,m}\cos(\frac{m\pi(y+w)}{2w}) - D_{n,m}\sin(\frac{m\pi(y+w)}{2w})) \end{aligned} \quad (5.6)$$

$$\begin{aligned} \vec{\nabla}^2\Phi_{n,m}(x, y) = & -((\frac{n\pi}{L})^2 + (\frac{m\pi}{2w})^2)(A_{n,m}\sin(\frac{n\pi x}{L}) + B_{n,m}\cos(\frac{n\pi x}{L})) \\ & (C_{n,m}\sin(\frac{m\pi(y+w)}{2w}) + D_{n,m}\cos(\frac{m\pi(y+w)}{2w})) \end{aligned} \quad (5.7)$$

First we consider 5.4,

$$\begin{aligned} & \frac{n\pi}{L}(-A_{n,m}\sin(\frac{n\pi x}{L}) + B_{n,m}\cos(\frac{n\pi x}{L}))(C_{n,m}\sin(m\pi) + D_{n,m}\cos(m\pi)) \\ & = \frac{n\pi}{L}(-A_{n,m}\sin(\frac{n\pi x}{L}) + B_{n,m}\cos(\frac{n\pi x}{L}))(C_{n,m}\sin(0) + D_{n,m}\cos(0)) \end{aligned} \quad (5.8)$$

= 0

and we see that $D_{m,n} = 0$, rendering $C_{m,n}$ redundant. Combining 5.2 and 5.6 we have

$$\begin{aligned} \frac{m\pi}{2w} (A_{m,n} \cos(\frac{n\pi(x+L)}{L}) + B_{m,n} \sin(\frac{n\pi(x+L)}{L})) \cos(\frac{m\pi(y+w)}{2w}) = \\ \frac{m\pi}{2w} (A_{m,n} \cos(\frac{n\pi x}{L}) + B_{m,n} \sin(\frac{n\pi x}{L})) \cos(\frac{m\pi(-y+w)}{2w}) \end{aligned} \quad (5.9)$$

If $f(y)$ is odd under $y \rightarrow -y$, then $f(x)$ will have to be odd under $x \rightarrow x + L$. The same goes for an even symmetry in each. Odd m provides odd symmetry around $y = 0$, and vice versa. Odd n provides odd symmetry under translation by L , and even even. The sum over the indices becomes $(2m, 2n)$ and $(2m + 1, 2n + 1)$. Next we combine 5.3 and 5.6,

$$\begin{aligned} \frac{n\pi}{L} (-A_{n,m} \sin(\frac{n\pi(x+L)}{L}) + B_{n,m} \cos(\frac{n\pi(x+L)}{L})) \sin(\frac{m\pi(y+w)}{2w}) \\ = -\frac{n\pi}{L} (-A_{n,m} \sin(\frac{n\pi x}{L}) + B_{n,m} \cos(\frac{n\pi x}{L})) \sin(\frac{m\pi(-y+w)}{2w}) \end{aligned} \quad (5.10)$$

We find that the same odd/even conditions satisfy the boundary condition above. To evaluate the Green's function we take an inner product of the divergence of the field and a delta function. For $\vec{\nabla}^2 \Phi = 2\pi \delta(\vec{x} - \vec{x}_0)$, $A = K \cos(\frac{n\pi x_0}{L})$, $B = K \sin(\frac{n\pi x_0}{L})$ and $K = \frac{4 \sin(\frac{m\pi(y_0+w)}{2w})}{\pi w L (\frac{n^2}{L^2} + \frac{m^2}{2w^2})}$. We also allow ourselves a superflow term $\vec{J}_d = k \hat{x}$ which we may employ to ensure the boundary condition $\psi(x, y) = \psi(x + L, -y)$ is satisfied.

The 5.2 represents a few specific path integrals over the flow field. Contributions to the phase accumulated along each arrow are written down as their scalar totals as letters a through d. Explicitly $a = \int_{-w}^w (\frac{d}{dx} \Phi(x, y'))|_{x=0, y'=y} dy$, b and c are two more contributions from the vortex, and d is from the superflow term. Any closed path integral $\oint (\hat{z} \times \vec{\nabla} \Phi) dx dy = n2\pi$. Consider two such path integrals $a + c + d$ and $2a + c - b$. We can choose d to satisfy the condition $a + c + d = 2\pi$. A path enclosing the vortex we've placed at the center of the strip must also acquire a 2π phase, so the closed path integral $2a + c - b = 2\pi$ When we use the first path to solve for a and substitute that into the other, we produce the relationship $d = \pi - c - b$. If we make the coordinate transformation $y+w \rightarrow y$ and then $2w \rightarrow w$, $c+b = \sum_{n=1}^{\infty} \sum_{m=1}^{\infty} 128 (\frac{4(2m-1) \sin^2(\pi m) \cos(\pi n) \sin(\frac{1}{20} \pi (2m-1) y_0)}{\pi (2n-1) (64m^2 - 64m + 4n^2 - 4n + 17)}) -$

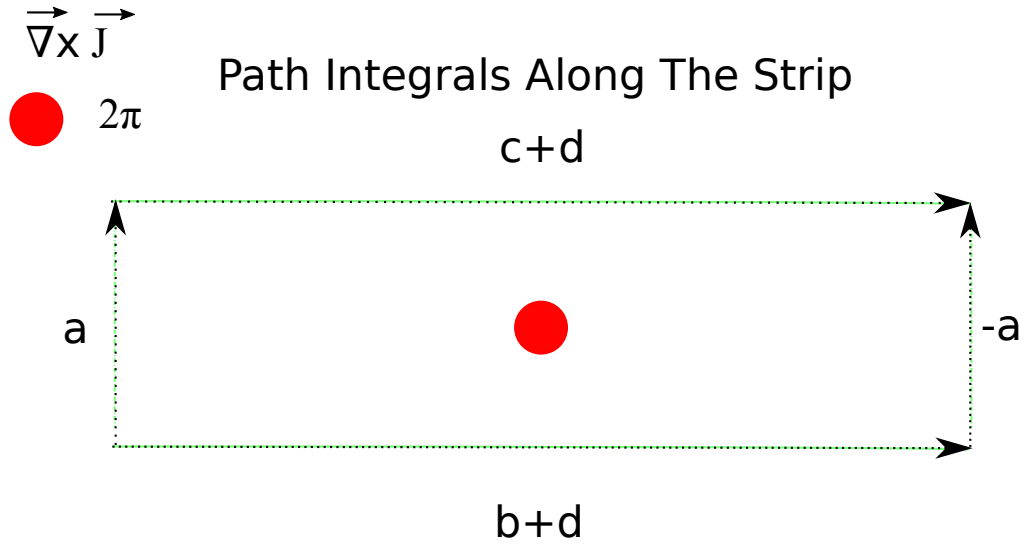


Figure 5.2: The scalar values a , b , c and d are path integrals taken along the directions indicated. The superflow component d is separated from the purely rotational contribution from the vortex

$\frac{m \cos^2(\pi m) \sin(\pi n) \sin(\frac{\pi m y_0}{10})}{16\pi m^2 n + \pi n^3}$). Because $\sin^2(\pi m) = \sin^2(\pi n) = 0$, every term in this sum is zero.

What we have then is $c = -b$ and $d = \pi$.

The eigenbasis with which we represent the phase and its Green's function analog is a discrete fourier eigenbasis. The fourier representation of a delta function does not converge, but any superfluid system with chemical potential μ will see energy scales above μ become incoherent ballistic states of a thermal gas, so we roll off our series summation past lengthscales longer than the healing length. We do this by replacing the delta function with a narrow-waisted 2D Gaussian distribution, which turns into a wide Gaussian distribution in momentum space. I've numerically evaluated this truncated series for all y_0 and found something I wasn't trying to produce, a line defect that can be seen in Fig. 5.3.

The whole problem boils down to one thing: The divergence of the green's function is not a delta function. There is also a ridge located at $y = y_0$, which leads to a small curl everywhere on the strip at the same location. It is not due to any ringing. Multiplying the solution by a narrower gaussian in fourier space turns the ridge into a more diffuse presence but does not remove it. The ridge becomes broad, and so a smaller curl per area exists over

An Eigenspace Approach

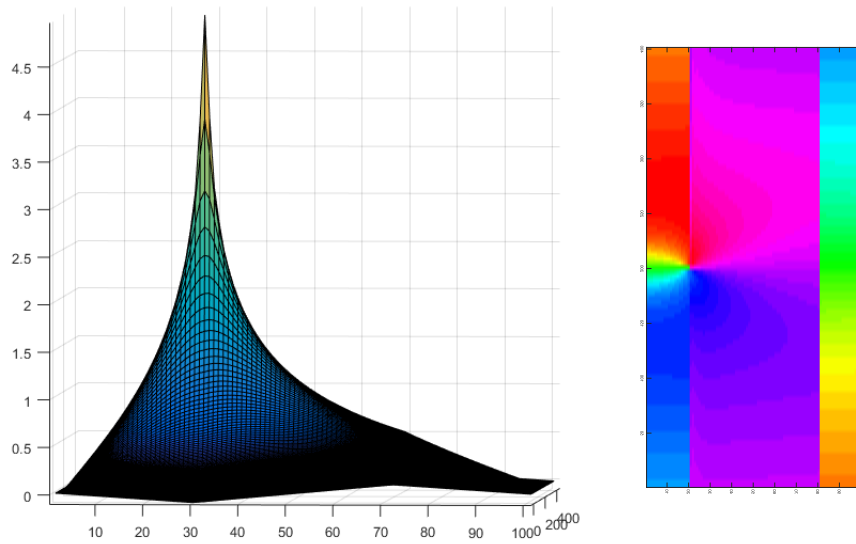


Figure 5.3: Above are both a Green's function and a phase profile as constructed with the eigenspace approach. Note the kink in the Green's function and the corresponding phase discontinuity in the strip. The units on the graph are raw matrix indices.

a larger area. But neither approach changes the central problem: the phase profile is path integral dependant. There is a line phase defect centered at $y = y_0$ that separates the strip into two distinct bands, one central and one outer. It only disappears when the vortex is at the absolute center of the mobius strip. The size of the phase difference between $(x, y_0 + \delta)$ and $(x, y_0 - \delta)$ depends on where along x one crosses that line defect. It is a line defect that cannot exist in a real interacting quantum fluid. The energy cost is too high. This suggests a vortex can only exist exactly at the Mobius strip's center. This would call into question the viability of the XY renormalization group's local symmetry as a function of the boundary conditions of the problem, and is thus unlikely.

I chose a second approach. A method of images solution would approach the boundary conditions perturbatively and guarantee the absence of any sharp localized artifacts due a poor choice of eigenbasis. A Mobius strip can be considered a real space projection of half of a virtual cylinder of circumference $2L$ and width $2w$. There exists a method of images solution whose individual flow contributions converge in $1/n$, with a

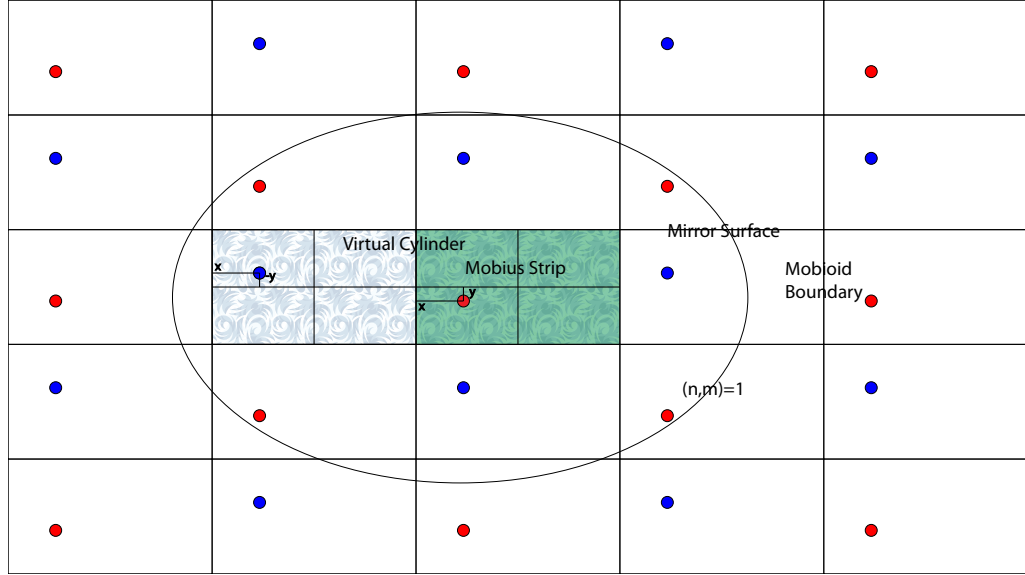


Figure 5.4: By treating the Mobius Strip as half a cylinder and its borders as mirrors I construct a method of images solution as a special case of the infinite parallel conductor solution in 2D electrostatics. Blue and red dots represent vortices of opposite helicity.

potential of the form $(-1)^{n+m} \ln \sqrt{(x - x_0 - nL)^2 + (y - (-1)^{n+m}y_0 + 2nw)^2}$ The truncated solution differs from the eigenbasis approach in one obvious way: there are no line phase defects. The superflow term is still roughly a constant as a function of y_0 . The same path integrals can be constructed, and the same condition set that $a + c + d = 2\pi$ produces $d = \pi$ The important thing to notice in the green's function drawing is that there aren't any kinks in the slope. The phase function similarly does not see any kinks. The integrand in the phase function picture, Figure 5, first integrates along x then along y . The function mostly meets the boundary conditions. This image and green's function was produced with a max m and n of 400, so any further effects will be at the center of a multipole of a very, very high order at a very long distance.

The numerical evaluation of the method of images solution of a lone vortex reveals roughly the same behavior one sees in with a single vortex on a ring. A vortex can enter from one side, traverse the strip, and exit the other, with the total superflow in the strip the ratio of $\frac{y_0+w}{2w}2\pi/L$. A vortex can similarly enter a ring from the outside, traverse the ring as it ramps up the superflow, and then enter the center of the ring, at which point

The Method of Images Superflow Remainder

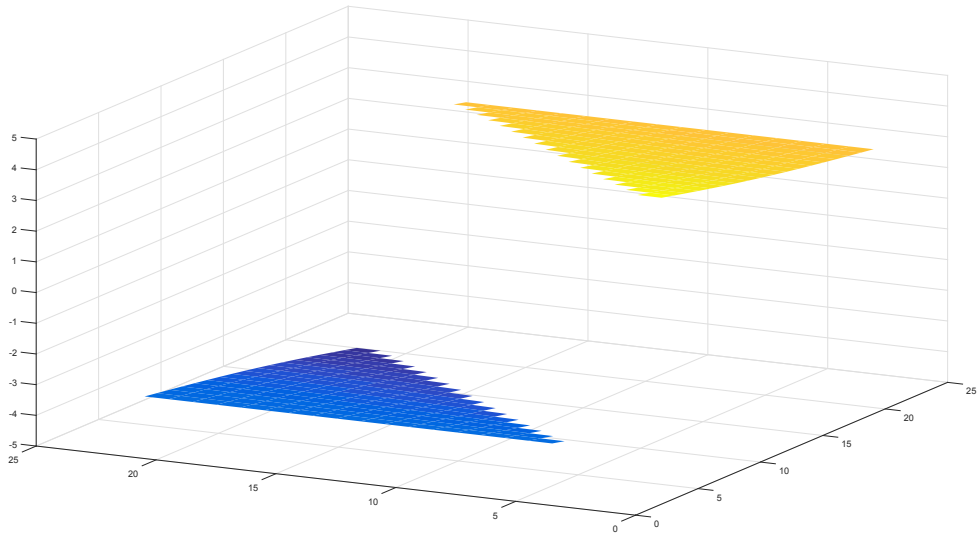


Figure 5.5: The axes on this graph are the position y along the strip and the position of the vortex y_0 . This is $\int_{x=0}^{x=L} \nabla \phi(x, y, y_0)$. The phase accumulated in the absence of the superflow term is roughly π regardless of the position of the vortex or the line along the strip the integrand is taken. The discontinuity in the graph is the vortex core. This is numerical evidence that the multipole solutions require the same superflow term $d = \pi$

any path integral around the ring leads to a phase of 2π . The behavior of interacting vortices is radically different. Two nearby vortices each of rotational charge q will be repelled from one another and attracted to each other's mirror image around the strip, enhancing the interaction potential. They can race around the strip and annihilate each other. This smoothly connects a Mobius strip with angular momentum $4\pi n$ to 0 without any quasiparticles leaving the system by its boundary. There are two orthogonal axes in the set of topologically distinct states in a superfluid mobius strip. One derives from the round-trip superflow term, which in real space consists of a tensor angular momentum. The other is whether there are an even or odd number of vortices on the strip. In a real system I expect vortices to enter and exit at the edges of the strip by a variety of the Magnus force, acting as transient states between quanta of superflow. An isolated space would see two varieties of state. One where there was a vortex and some fractional value of superflow. The other where there were no vortices and 2π quantized superflow. The

A Method of Images Solution

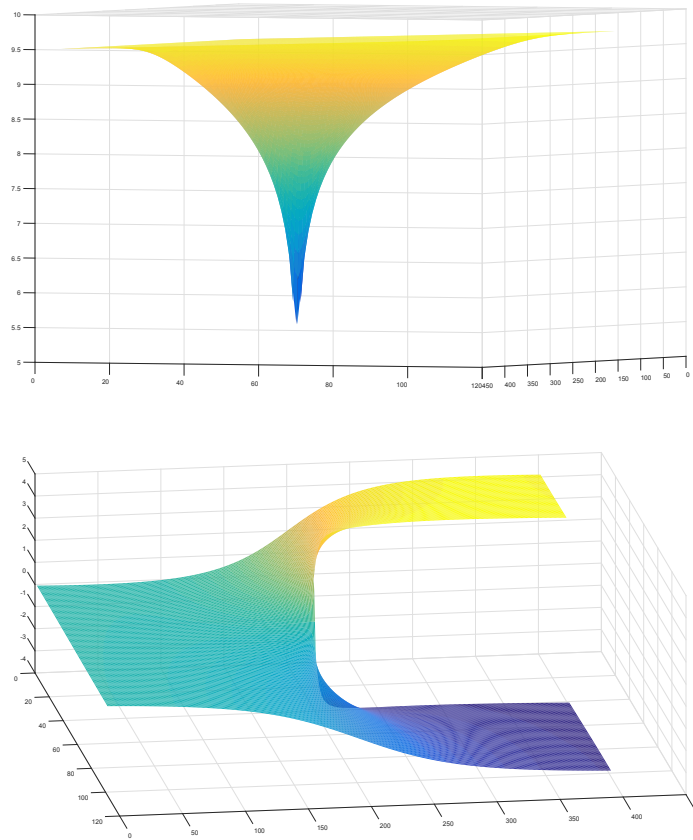


Figure 5.6: Note the lack of any kink. The phase profile integral was the simplest I could take, and so it passes quite close to the core. The integral was first taken along x , then y . Every position y_0 of the vortex core looks roughly the same. Note the π difference from one side to the other. This phase function has no superflow term added in. A gradient of $\frac{\pi x}{L}$ realizes a self-consistent and continuous wave function with a curl solely at the vortex core.

thermodynamic limit cannot exist for this system, as when L scales to ∞ we recover only the local symmetry class. The most interesting physics are likely to come out of vortex interactions. I cannot predict how the Kibble-Zurek mechanism would change on a Mobius strip compared to a ring, but I'm willing to bet it would, as there exists a path for any spontaneously generated angular momentum of order greater than 1 to cancel itself out. And if my method of images is fundamentally flawed, it may mean that the only eigenspace solution with a localized vortex, where it's right in the middle, would be very interesting.

Bibliography

- [1] Nigel Goldenfeld. Lectures on Phase Transitions and the Renormalization Group. *Frontiers in Physics*, 85, 1992.
- [2] M.H. Anderson, J.R. Ensher, M.R. Matthews, C.E. Wieman, and E.A. Cornell. Vortex Nucleation in Bose-Einstein Condensates in an Oblate, Purely Magnetic Potential. *Science.*, 269:198–201, 1995.
- [3] K.B. Davis, M.-O. Mewes, M.R. Andrews, N.J. van Druten, D.S. Durfee, D.M. Kurn, and W. Ketterle. Bose-Einstein condensation in a gas of sodium atoms. *Phys. Rev. Lett.*, 75:3969–3973, 1995.
- [4] B. DeMarco and D. S. Jin. Onset of Fermi Degeneracy in a Trapped Atomic Gas. *Science.*, 285:1703–1706, 1999.
- [5] Andrew G. Truscott, Kevin E. Strecker, William I. McAlexander, Guthrie Partridge, and Randall G. Hulet. Observation of Fermi Pressure in a Gas of Trapped Atoms. *Science.*, 291:2570–2572, 2001.
- [6] C. Ospelkaus, S Ospelkaus, L. Humbert, P. Ernst, K. Sengstock, and K. Bongs. Heteronuclear Molecules in a 3D Optical Lattice. *Phys. Rev. Lett.*, 97:120403, 2006.
- [7] Cheng Chin, Rudolf Grimm, Paul Julienne, and Eite Tiesinga. Heteronuclear Molecules in a 3D Optical Lattice. *Rev. Mod. Phys.*, 82:1225, 2010.
- [8] J L. Roberts, N R. Claussen, S L. Cornish, E A. Donley, Eric A. Cornell, and C E. Wieman. Controlled Collapse of a Bose-Einstein Condensate. *Phys. Rev. Lett.*, 86, 2001.
- [9] F. Bringas, M. T. Yamashita, , and T. Frederico. Triatomic continuum resonances for large negative scattering lengths. *Phys. Rev. A*, 69, 2004.
- [10] Markus Greiner, Olaf Mandel, Tilman Esslinger, Theodor W. Hänsch, and Immanuel Bloch. Quantum phase transition from a superfluid to a Mott insulator in a gas of ultracold atoms. *Nature*, 415:39–44, 2002.

- [11] Ian B. Spielman, William D. Phillips, and James V. Porto. The Mott Insulator Transition in a Two Dimensional Atomic Bose Gas. *Phys. Rev. Lett.*, 98:080404, 2007.
- [12] KÄhl M, Moritz H, StÄfferle T, and Esslinger T. GÄijnter K. Fermionic Atoms in a Three Dimensional Optical Lattice: Observing Fermi Surfaces, Dynamics, and Interactions. *Phys. Rev. Lett.*, 94:080403, 2005.
- [13] Toshiya Kinoshita, Trevor Wenger, and David S. Weiss. A quantum Newton’s cradle. *Nature*, 440:900–903, 2006.
- [14] Z Hadzibabic, P KrÄijger, M Cheneau, S P Rath1, and J Dalibard. The trapped two-dimensional Bose gas: from BoseÄEinstein condensation to BerezinskiÄKosterlitzÄThouless physics. *New Journal of Physics*, 10, 2008.
- [15] Ming-Shien Chang, Qishu Qin, Wenxian Zhang, Li You, and Michael S. Chapman. Coherent spinor dynamics in a spin-1 Bose condensate. *Nature Physics*, 1:111–116, 2005.
- [16] L. E. Sadler, J. M. Higbie, S. R. Leslie, M. Vengalattore, and D. M. Stamper-Kurn. Spontaneous symmetry breaking in a quenched ferromagnetic spinor BoseÄEinstein condensate. *Nature*, 443:312Ä315, 2006.
- [17] Gregor Jotzu, Michael Messer, RÄlmi Desbuquois, Martin Lebrat, Thomas Uehlinger, Daniel Greif, and Tilman Esslinger. Experimental realization of the topological Haldane model with ultracold fermions. *Nature*, 515:237–240, 2014.
- [18] Y.-J. Lin, A. R. Perry, R. L. Compton, I. B. Spielman, and J. V. Porto. Rapid production of ⁸⁷Rb Bose-Einstein condensates in a combined magnetic and optical potential. *Phys. Rev. A*, 111:063631, 2009.
- [19] AndrÄ Eckardt, Martin Holthaus, Hans Lignier, Alessandro Zenesini, Donatella Ciampini, Oliver Morsch, , and Ennio Arimondo. Experimental realization of the topological Haldane model with ultracold fermions. *Phys. Rev. A*, 79:013611, 2009.
- [20] M.C. Beeler, M.E.W. Reed, T. Hong, and S.L. Rolston. Disorder-Driven Loss of Phase Coherence in a Quasi-2D Cold Atom System. *New Journal of Physics*, 14:073024, 2012.
- [21] B Allard, T Plisson, M Holzmann, G Salomon, A Aspect, P Bouyer, and T Bourdel. Effect of disorder close to the superfluid transition in a two-dimensional Bose gas. *Phys. Rev. A*, 85:033602, 2012.
- [22] S. S. Kondov, W. R. McGehee, J. J. Zirbel, and B. DeMarco. Effect of disorder close to the superfluid transition in a two-dimensional Bose gas. *Science*, 344, 2011.
- [23] Matthew P. A. Fisher. Quantum Phase Transitions in Disordered Two-Dimensional Superconductors. *Phys. Rev. Lett.*, 65:073024, 1990.

- [24] Nicolas Laflorencie. Sliding phase in randomly stacked 2d superfluids/superconductors. *EPL*, 99, 2012.
- [25] David Pekker, Gil Refael, and Eugene Demler. Finding the Elusive Sliding Phase in the Superfluid-Normal Phase Transition Smeared by c-Axis Disorder. *Phys. Rev Lett.*, 105:085302, 2010.
- [26] Priyanka Mohan, Paul M. Goldbart, Rajesh Narayanan, John Toner, and Thomas Vojta. Anomalous Elastic Intermediate Phase in Randomly Layered Superfluids, Superconductors, and Planar Magnets. *Phys. Rev Lett.*, 105:085301, 2010.
- [27] Nikolai V. Prokof'ev and Boris V. Svistunov. Two Definitions of Superfluid Density. *arxiv*, 1999.
- [28] Chen-Lung Hung, Xibo Zhang, Nathan Gemelk, and Cheng Chin. Observation of scale invariance and universality in two-dimensional Bose gases. *Nature*, 470:236, 2011.
- [29] Tin-Lun Ho and Qi Zhou. Obtaining the phase diagram and thermodynamic quantities of bulk systems from the densities of trapped gases. *Nature Physics*, 6:131–134, 2010.
- [30] Tarik Yefsah, Rami Desbuquois, Lauriane Chomaz, Kenneth J. Gajner, and Jean Dalibard. Exploring the thermodynamics of a two-dimensional Bose gas. *Phys. Rev Lett.*, 107:130401, 2011.
- [31] Gregory H Wannier. The Structure of Electronic Excitation Levels in Insulating Crystals. *Physical Review*, 52:191–197, 1937.
- [32] Emily E Edwards. CONSTRUCTION OF APPARATUS AND FIRST EXPERIMENTS INVESTIGATING DYNAMICS OF BOSE-EINSTEIN CONDENSATES IN DISORDERED OPTICAL LATTICES. *University of Maryland Library*, 2009.
- [33] Matthew Beeler. Disordered Ultracold Two-Dimensional Bose Gases. *University of Maryland Library*, 2010.
- [34] Jennifer Robinson. Explorations of Variable Interactions in a Cold Rubidium Rydberg Gas. *University of Maryland Library*, 2012.
- [35] Y.-J. Lin, A. R. Perry, R. L. Compton, I. B. Spielman, and J. V. Porto. Rapid production of ^{87}Rb Bose-Einstein condensates in a combined magnetic and optical potential. *Phys. Rev. A*, 79:063631, 2009.
- [36] Michael Schreiber, Sean S. Hodgman, Pranjal Bordia, Henrik P. Lüscher, Mark H. Fischer, Ronen Vosk, Ehud Altman, Ulrich Schneider, and Immanuel Bloch. Observation of many-body localization of interacting fermions in a quasi-random optical lattice. *Science*, 349:842–845, 2015.

- [37] Dina Genkina, LM Aycock, BK Stuhl, Hsin-I Lu, RA Williams, and IB Spielman. Feshbach enhanced s-wave scattering of fermions: direct observation with optimized absorption imaging. *New Journal of Physics*, 18, 2015.
- [38] Chen-Lung Hung, Xibo Zhang, Li-Chung Ha, Shih-Kuang Tung, Nathan Gemelke, and Cheng Chin. Extracting density–density correlations from in situ images of atomic quantum gases. *New Journal of Physics*, 13, 2011.
- [39] Francesco Sciortino and Piero Tartaglia. Extension of the Fluctuation-Dissipation Theorem to the Physical Aging of a Model Glass-Forming Liquid. *Phys. Rev. Lett.*, 86, 2001.
- [40] Las-Pho. Encyclopedia of Optical Engineering. *CRC Press*, page 1892, 2003.
- [41] G. Birkl, M. Gatzke, I. H. Deutsch, S. L. Rolston, and W. D. Phillips. Bragg Scattering from Atoms in Optical Lattices. *Phys. Rev. Lett.*, 75:842–845, 2015.
- [42] G. Birkl, M. Gatzke, I. H. Deutsch, S. L. Rolston, and W. D. Phillips. Simple piezoelectric-actuated mirror with 180 kHz servo bandwidth. *Optics Express*, 18:9739–9746, 2010.
- [43] H Muntinga, H Ahlers, M Krutzik, A Wenzlawski, S Arnold, D Becker, K Bongs, H Dittus, H Duncker, N Gaaloul, C Gherasim, E Giese, C Grzeschik, T W Hansch, O Hellmig, W Herr, S Herrmann, E Kajari, S Kleinert, C Lammerzahl, W Lewoczko-Adamczyk, J Malcolm, N Meyer, R Nolte, A Peters, M Popp, J Reichel, A Roura, J Ruldolph, M Schiemangk, M Schneider, S T Seidel, K Sengstock, V Tamma, T Valenzuela, A Vogel, R Walser, T Wendrich, P Windpassinger, W Zeller, T van Zoest, W Ertmer, W P Schleich, and E M Rasel. Interferometry with Bose-Einstein Condensates in Microgravity. *Phys. Rev. Lett.*, 111:093602, 2013.
- [44] Y. Castin and R. Dum. Bose-Einstein Condensates in Time Dependent Traps. *Phys. Rev. Lett.*, 77, 1996.
- [45] Bess Fang, Aisling Johnson, Tommaso Roscilde, and Isabelle Bouchoule. Momentum-Space Correlations of a One-Dimensional Bose Gas. *Phys. Rev. Lett.*, 116, 2016.
- [46] NIST Digital Library of Mathematical Functions. <http://dlmf.nist.gov/>, Release 1.0.11 of 2016-06-08. Online companion to [47].
- [47] F. W. J. Olver, D. W. Lozier, R. F. Boisvert, and C. W. Clark, editors. *NIST Handbook of Mathematical Functions*. Cambridge University Press, New York, NY, 2010. Print companion to [46].